

AN INSTRUMENTED PROSTHESIS FOR MEASURING
THE CARTILAGE SURFACE PRESSURE DISTRIBUTION IN THE HUMAN HIP

by

CHARLES E. CARLSON

B.S.M.E., University of Illinois
B.S.E.E., University of Illinois
(1966)

S.M.M.E., Massachusetts Institute of Technology
(1967)

SUBMITTED IN PARTIAL FULFILLMENT

OF THE REQUIREMENTS FOR THE

DEGREE OF

DOCTOR OF SCIENCE

at the

MASSACHUSETTS INSTITUTE OF TECHNOLOGY

June, 1972

Signature of Author
Department of Mechanical Engineering, May 5, 1972

Certified by
Thesis Supervisor

Accepted by
Chairman, Departmental Committee on Graduate Students



AN INSTRUMENTED PROSTHESIS FOR MEASURING
THE CARTILAGE SURFACE PRESSURE DISTRIBUTION IN THE HUMAN HIP

by

CHARLES E. CARLSON

Submitted to the Department of Mechanical Engineering
on May 5, 1972, in partial fulfillment of the requirements
for the degree of Doctor of Science.

ABSTRACT

Knowledge of the pressures acting on the cartilage surfaces in the human hip is of interest for several reasons. Information on the magnitude and distribution of pressure on articular cartilage in the hip would provide a better understanding of the physiology of cartilage. Such information could provide further insight into the causes of cartilage destruction, such as is observed in osteoarthritis. Knowledge of the pressure distribution on cartilage surfaces would be particularly useful in studies of joint lubrication.

A method of measuring in vivo the spatial and temporal pressure variations on the cartilage surfaces in the human hip has been developed. The pressure measurements will be made by replacing the head and neck of the femur with an instrumented prosthesis. The hollow ball of this prosthesis contains a network of pressure transducers which measure the pressure distribution on the surface of the ball. The signals from these transducers are transmitted to external receiving and recording equipment by a multi-channel time-multiplexing PAM/FM telemetry device which also is located inside the ball of the prosthesis. The telemetry device is powered externally through a power induction system.

A prototype of the instrumented prosthesis has been constructed which demonstrates the satisfactory performance of the pressure measuring system.

Thesis Supervisor: Robert W. Mann
Title: Germeshausen Professor

ACKNOWLEDGMENTS

The number of people who deserve recognition for the time, energy, and talent that they have contributed to this project is truly significant. First and foremost are the members of my doctoral committee--Professors Robert W. Mann, William M. Murray, Stephen K. Burns, and Dr. William H. Harris--whose patient guidance and timely suggestions during the course of this project were most welcome.

The following people also deserve special recognition. Sincere thanks are due:

Edward Duggan, Peter Corbett and Bernard Lane, of the Charles Stark Draper Laboratory, for packaging and fabricating the telemetry unit;

Stanley LaShoto, of the Charles Stark Draper Laboratory, for assistance in a multitude of machining problems;

John Crep, of Howmedica, Inc., for supplying the hip prostheses;

John Mingos, of Applied Energy Company, for electron beam welding the prostheses;

Jerry Dubreuil, of Athbro Precision Engineering Corporation, for machining the pressure transducer diaphragms; and

Joseph Mallon, of Kulite Semiconductor Products, Inc., for supplying the cantilever beams for the pressure transducers.

This list would not be complete without mention of my wife, Joan, whose assistance in preparing this thesis saved me many hours of tedious labor.

The phase-locked loop pulse generator described in Appendix G was designed and built by Donald Wade, a student in the Electrical Engineering Department at M.I.T.

The author thanks the National Science Foundation and the National

Institute for General Medical Sciences for tuition and stipend support.

This project has been funded by grants from the Medical Foundation, Inc., the Smith-Petersen Foundation, the Easter Seal Research Foundation and the Germeshausen Professorship of Professor Robert W. Mann.

TABLE OF CONTENTS

	<u>Page</u>
ABSTRACT	2
ACKNOWLEDGMENTS	3
LIST OF FIGURES	9
NOMENCLATURE	12
CHAPTER 1 - INTRODUCTION	16
The Human Hip	16
Loads Carried by the Hip Joint	19
Role of Magnitude and Distribution of Load in Osteoarthritis	22
Joint Lubrication	22
Modelling of Cartilage	24
Improvements in Hip Prostheses	24
CHAPTER 2 - THE PRESSURE MEASURING SYSTEM	26
Basic Approach	26
Why Human Experimentation	26
Validity of Method	28
Pressure Measuring System Requirements	30
Physiological Requirements	30
Technical Requirements	30
Experimental Requirements	31
Basic Design Approach	32
Pressure Measuring Instrumentation	32
The Pressure Transducer	33
Pressure Sensing Element	33
Pressure Transducer Diaphragm Dimensions	33

TABLE OF CONTENTS (cont.)

	<u>Page</u>
Transducer Mechanical-to-Electrical	
Conversion Element	36
The Telemetry System	41
Telemetry Device Construction	45
Power Induction Circuitry	45
Data Receiving, Recording, Display and Computation	47
Prosthesis Modifications	49
Proposed Experimental Procedure	53
Candidate Selection	53
Surgical Procedure	53
Test Program	54
CHAPTER 3 - SUMMARY	56
APPENDIX A - ESTIMATE OF PEAK PRESSURE IN THE HIP JOINT	57
APPENDIX B - DIAPHRAGM STRESS ANALYSIS	62
Section One: Method and Results	62
Section Two: Equations	82
Numerical Values	95
Flat Diaphragm Equations	96
Worst-Case Stress Conditions	97
Stresses in Diaphragms of Different Radius of Curvature	97
Table 1. Stresses in Spherical Diaphragm	99
Table 2. Stresses in Flat Diaphragm	103
Table 3. Comparison of Worst-Case Radial Stress Ranges	104

TABLE OF CONTENTS (cont.)

	<u>Page</u>
APPENDIX C - DIAPHRAGM FATIGUE TEST	105
Fatigue Test Specifications	105
Experimental Apparatus	106
Test Results	108
Test Conclusions	110
APPENDIX D - PRESSURE TRANSDUCER DESIGN AND ASSEMBLY	111
Mechanical-to-Electrical Conversion Element	111
Strain Gage Bridge	116
Pressure Transducer Assembly Procedure	119
APPENDIX E - TELEMETRY SYSTEM OPERATION, FABRICATION AND CALIBRATION	123
Circuit Operation	123
Pulse Generator Stage	123
Multiplexer and Pressure Transducer Stages	126
Diode Isolation Stage	128
Amplifier Stage	130
Oscillator Stage	133
Power Supply Stage	139
Heating of Prosthesis Due to Power Dissipation in Telemetry System	145
Legal Requirements for Operation of Telemetry System	145
Telemetry Device Packaging	146
Pressure Transducer/Telemetry System Calibration	150
Telemetry Device Schematic	152
APPENDIX F - POWER INDUCTION SYSTEM	154

TABLE OF CONTENTS (cont.)

	<u>Page</u>
APPENDIX G - DATA ACQUISITION, STORAGE AND COMPUTATION	162
Telemetry System Receiver	162
Telemetry Data Recorder	162
Data Processing	163
Data Computation	166
APPENDIX H - PROSTHESIS MODIFICATIONS, ASSEMBLY AND	
STERILIZATION	167
Mechanical Details of Instrumented Hip Prosthesis	167
Alignment Ring	167
Stem Redesign	170
Power Induction Coil Design and Assembly	171
Prosthesis Assembly	177
Prosthesis Sterilization Procedure	179
REFERENCES	182
BIOGRAPHICAL NOTE	184

LIST OF FIGURES

	<u>Page</u>
1 The Human Skeletal System Associated with the Hip Joint .	17
2 A Side View of a Portion of the Pelvis Illustrating the Acetabulum	18
3 Diagram of Joint Structure	20
4 Hip Joint Load during Walking	21
5 Standard Moore Prosthesis	27
6 Construction of Standard Prosthesis	27
7 Cross Section of Transducer Diaphragm	34
8 Cross Section of Transducer	38
9 Pressure Transducer Mounted in Prothesis Hemisphere . . .	39
10 Pressure Transducer Locations in Hemisphere	40
11 Time Multiplexed PAM Signal	42
12 Block Diagram of Telemetry Device	44
13 Telemetry Device Prior to Mounting in Prosthesis.	46
14 Standard and Instrumented Prostheses	50
15 Side View of Modified Prosthesis (Power Induction Coil Not Shown).	51
A1 A Side View of a Portion of the Pelvis Illustrating the Acetabulum	58
A2 Assumed Pressure Distribution for Calculation of Maximum Pressure	60
B1 Model of Spherical Diaphragm Boundary Conditions	63
B2 Planes in State-Space for which Solutions Exist	66
B3 Superposition of Loading Conditions	67
B4 Plane in State-Space for which Solutions Are Needed . . .	69

LIST OF FIGURES (cont.)

	<u>Page</u>
B5	Line in State-Space Determined by Radial Edge Load F . . . 71
B6	Line in State-Space Determined by Limiting Stresses at k = 0 and k \rightarrow ∞ for Transverse Pressure p 72
B7	Region in State-Space in Which Solutions Now Exist . . . 73
B8	Radial Stresses at Diaphragm Surfaces Due to 1000 psi Applied to Diaphragm for Edge Conditions k = 0 and k \rightarrow ∞ When F = 0 75
B9	Comparison of Radial Surface Stresses for Spherical Diaphragm with Clamped Edge (k \rightarrow ∞) and Flat Diaphragm of Same Dimensions. Applied Pressure Is 1000 psi. 76
B10	Stresses in Radial Direction on Diaphragm Surfaces for P = 0, F = F _{max} 77
B11	Radial Stresses at Diaphragm Surfaces Showing Effect of Edge Load F When k = 0. Transverse Pressure Is 1000 psi. 79
B12	Goodman Diagram Showing Peak Stress Ranges for Worst- Case Conditions 81
B13	Locations of Normal Forces and Bending Moments on Section of Diaphragm 86
B14	Boundary Conditions for Cases I, II and III 87
B15	Locations of Principal Shear Stresses in Diaphragm . . . 94
C1	Fatigue Test Apparatus 107
C2	Fatigue Test Pressure Waveform 109
D1	Cross Section of Transducer 113

LIST OF FIGURES (cont.)

	<u>Page</u>
D2 Displacement Sensing Element before Mounting	115
D3 Displacement Sensing Element Mounted in Hemisphere	115
D4 Pressure Transducer Cantilever Beam	117
E1 Block Diagram of Telemetry Device	124
E2 Pulse Generator Stage	125
E3 Transducer Bridge Switching Circuitry	127
E4 Diode Isolation of Transducer Bridges	129
E5 Amplifier Stage	131
E6 Synchronization and Calibration Circuitry	134
E7 Oscillator Stage and Antenna Coupling	135
E8 Power Supply Stage	140
E9 Current Flow in Milliampères through Telemetry Device Stages	144
E10 Individual Printed Circuit Boards in Telemetry Device	148
E11 Assembled Telemetry Device	148
E12 Mounting Arrangement of Telemetry Device in Hemisphere	149
E13 Sixteen-Channel Transmitter	153
F1 Power Induction Circuitry	155
G1 Signal Processing Stages	165
H1 Standard and Instrumented Prostheses	168
H2 Hemisphere and Stem of Standard Prosthesis	168
H3 Hemisphere, Stem and Alignment Ring in Modified Prosthesis	169
H4 Power Induction Coil Encapsulation	173
H5 Side View of Modified Prosthesis (Power Induction Coil Not Shown)	176
H6 Weld Bead Grinding Setup	180

NOMENCLATURE

a	radius of diaphragm
A	$1/Eh$
$ber(\lambda), bei(\lambda)$ $ber'(\lambda), bei'(\lambda)$	real and imaginary parts (and their derivatives) of $J_0(i^{3/2}x)$
Be_1	$\frac{bei'(\lambda)ber(\lambda) - ber'(\lambda)bei(\lambda)}{ber'(\lambda)}$
Be_2	$\frac{[ber'(\lambda)]^2 + [bei'(\lambda)]^2}{ber'(\lambda)}$
c	one-half of cantilever beam thickness
D	$\frac{Eh^3}{12(1-\nu^2)}$
E	modulus of elasticity
F	radial edge load on diaphragm; also stress function in stress analysis differential equations
F_{max}	maximum radial edge load
g	acceleration at sea level due to gravity
G	gain of operational amplifier
GF	strain gage gage factor
h	diaphragm thickness
I_1	primary resonant circuit current
I_2	secondary resonant circuit current
I_{in}	input current, power induction system
I_L	load current, power induction system
$J_0(\quad)$	Bessel function of first kind of order zero
$J_0(i^{3/2}x)$	$ber(x) + i bei(x)$
k	stiffness of cantilever beam in pressure transducer; also stiffness of springs in model of diaphragm boundary conditions

NOMENCLATURE (cont.)

k_{actual}	stiffness of diaphragm edge supports
l	length of cantilever beam
m	mass of sliding pin and cantilever beam in pressure transducer
M_r, M_θ	bending moments per unit length in radial and tangential directions
N	number of turns in primary power induction coil
N_r, N_θ	loads per unit length in radial and tangential directions
\bar{N}_r	load per unit length at circumference of diaphragm
p	pressure
p_{max}	maximum pressure
P_{in}	input power, power induction system
P_L	power dissipated in load, power induction system
P_n	pressure applied to diaphragm surface in transverse (normal) direction
P_{R_2}	power dissipated in secondary coil, power induction system
P_o	transverse pressure on diaphragm
r	radial distance from center of diaphragm
r, θ	polar coordinates in plane tangent to apex of diaphragm
R	radius of prosthesis ball; also resistance of strain gages
R_D	dynamic resistance of isolation diodes
s	stress
s_e	endurance limit
s_{mean}	average (mean) stress

NOMENCLATURE (cont.)

s_u	ultimate stress
s_y	yield stress
u	displacement of diaphragm in radial direction
V_i	strain gage bridge excitation voltage
V_o	strain gage bridge output voltage; also output voltage of operational amplifier
w	transverse component of diaphragm middle surface displacement
W_b	body weight
x	distance from free end of cantilever beam
y_e	deflection of end of cantilever beam
Z_{in}	input impedance, power induction system
ΔR	change in resistance of strain gages
ϵ	strain
ϵ_{avg}	average strain
θ, ϕ	spherical coordinates
λ	$\frac{a}{\sqrt{Rh}} [12(1-\nu^2)]^{1/4}$
ν	Poisson's ratio
ρ	r/a , dimensionless distance from diaphragm center
σ_e	endurance limit
σ_n	transverse stress (pressure) on diaphragm surface
σ_r, σ_θ	stresses in radial and tangential directions
$\sigma_{rB}, \sigma_{\theta B}$	bending stresses (B) on diaphragm surfaces in radial (r) and tangential (θ) directions
$\sigma_{rD}, \sigma_{\theta D}$	direct stresses (D) in radial (r) and tangential (θ) directions

NOMENCLATURE (cont.)

$\sigma_{r \text{ concave}}$	stress in radial direction on concave surface of diaphragm
$\sigma_{\theta \text{ concave}}$	stress in tangential direction on concave surface of diaphragm
$\sigma_{r \text{ convex}}$	stress in radial direction on convex surface of diaphragm
$\sigma_{\theta \text{ convex}}$	stress in tangential direction on convex surface of diaphragm
τ_1	shear stress in plane tangential to diaphragm surface
τ_2	shear stress in plane perpendicular to diaphragm surface
ω	power induction frequency
ω_n	natural frequency of pressure transducer

CHAPTER 1

INTRODUCTION

The human hip joint has been the subject of a number of investigations aimed at providing a better understanding of the biomechanics of the hip. One specific area of study has been the determination of the loads carried by the hip joint during activities such as standing, walking and running. The information gained from these studies is useful in describing certain gross characteristics of the joint, but the localized effects of these loads are not readily apparent if the distribution of these loads throughout the joint is unknown.

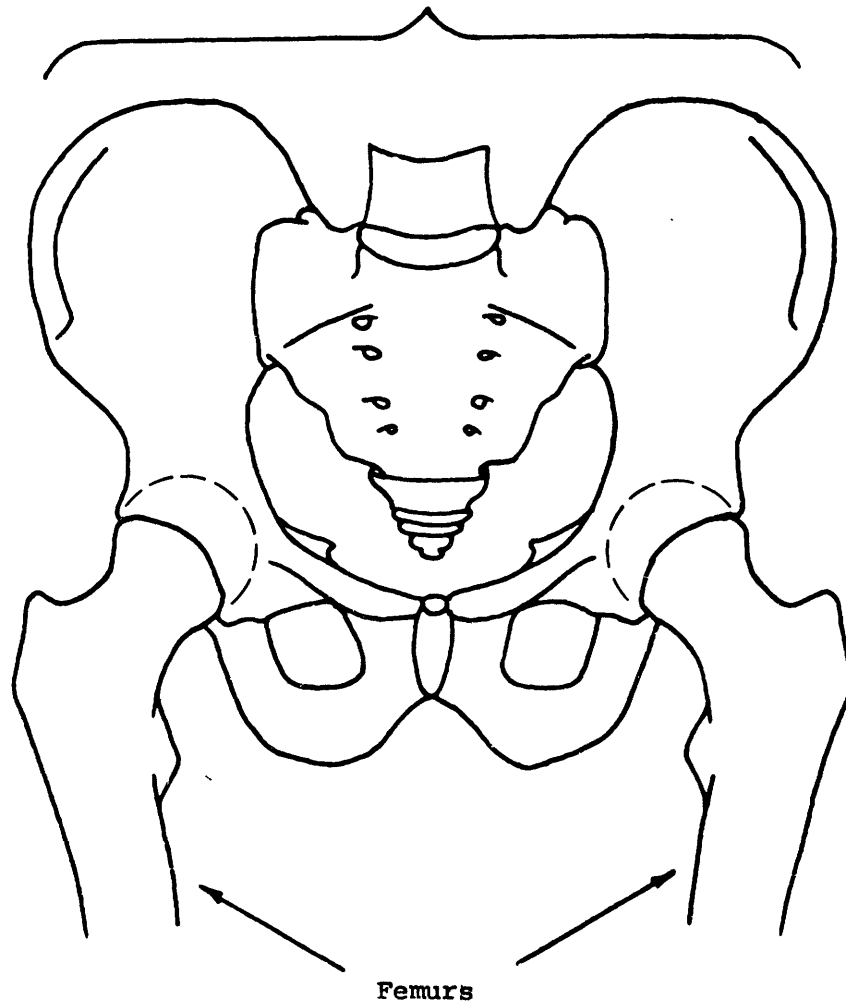
The distribution of the joint loads over the cartilage surfaces in the hip is of particular interest. Knowledge of the variation of the load per unit area, i.e., the pressure distribution, on the cartilage surface would be of considerable value in understanding the localized behavior of cartilage under normal and diseased conditions. This thesis describes a method of measuring the spatial and temporal pressure variations in vivo on the cartilage surfaces in the human hip.

The Human Hip

The hip joint is a ball-and-socket joint, as shown in Figure 1. The ball half of the joint is located on the upper end of the femur and is firmly held in the socket, or acetabulum, in the pelvis by ligaments and muscles which surround the joint and form the joint capsule.

The horseshoe-shaped load-carrying surface in the acetabulum is shown in Figure 2. The diameter of the hip joint in adults is

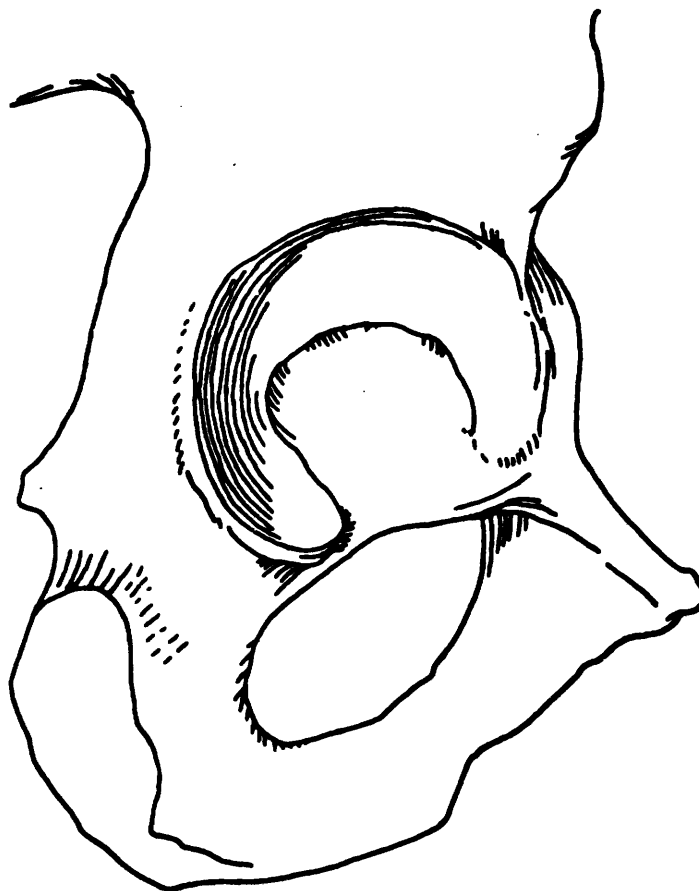
Pelvis



The Human Skeletal System Associated with the Hip Joint.

Figure 1

[Redrawn from W. Henry Hollinshead, Anatomy for Surgeons: Volume 3
(New York: Harper & Brothers, 1958), p. 712]



A Side View of a Portion of the Pelvis
Illustrating the Acetabulum.

Figure 2

[Redrawn from J. C. Boileau Grant, An Atlas of Anatomy (Baltimore:
The Williams & Wilkins Co., 1962), Figure 276]

typically slightly less than two inches. The femoral head and the acetabulum fit closely together, and their surfaces are very nearly spherical (Ref. 1).

The load-carrying surfaces on the ball of the femur and on the acetabulum in the pelvis are covered by a tough, viscoelastic layer of cartilage one to two millimeters thick. The synovial membrane which lines the interior of the joint capsule produces synovial fluid which serves to nourish as well as lubricate the cartilage tissue. A simplified schematic of the hip joint is shown in Figure 3.

Loads Carried by the Hip Joint

The hip joint is capable of supporting relatively large loads. By making various simplifying assumptions about the geometry and musculature of the joint, early investigators were able to determine the hip joint load for a person standing motionless on one leg. Inman (Ref. 2) calculated the minimum load for single-leg support to be between 2.4 and 2.6 times body weight.

The hip joint loads can be significantly higher under dynamic loading conditions. Paul (Ref. 3,4), by means of a theoretical analysis coupled with force-plate, cinematographic and electromyographic measurements, has calculated the time-varying load carried by the hip during walking. Paul's results, based on studies conducted on a number of young adults, show that the peak hip joint load during walking can be as high as 5 to 7 times body weight. A typical graph of joint load during one walking cycle is shown in Figure 4.

The loads carried by the hip joint were measured directly by

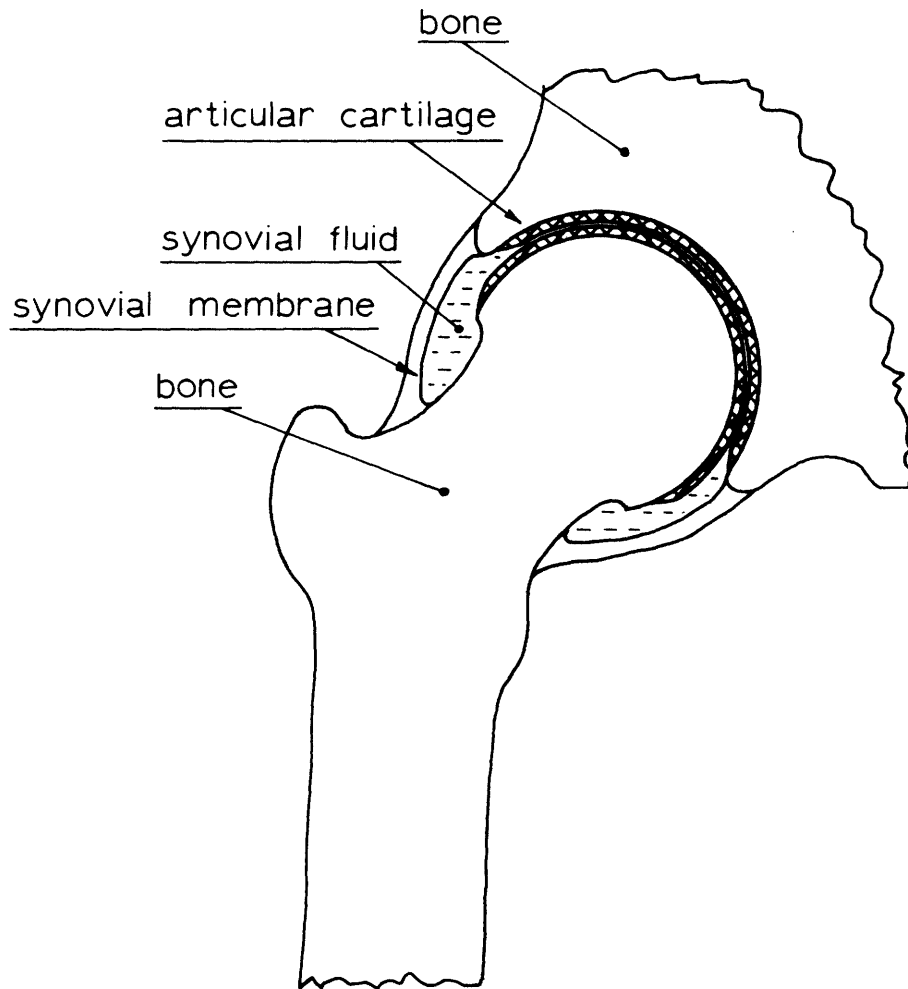
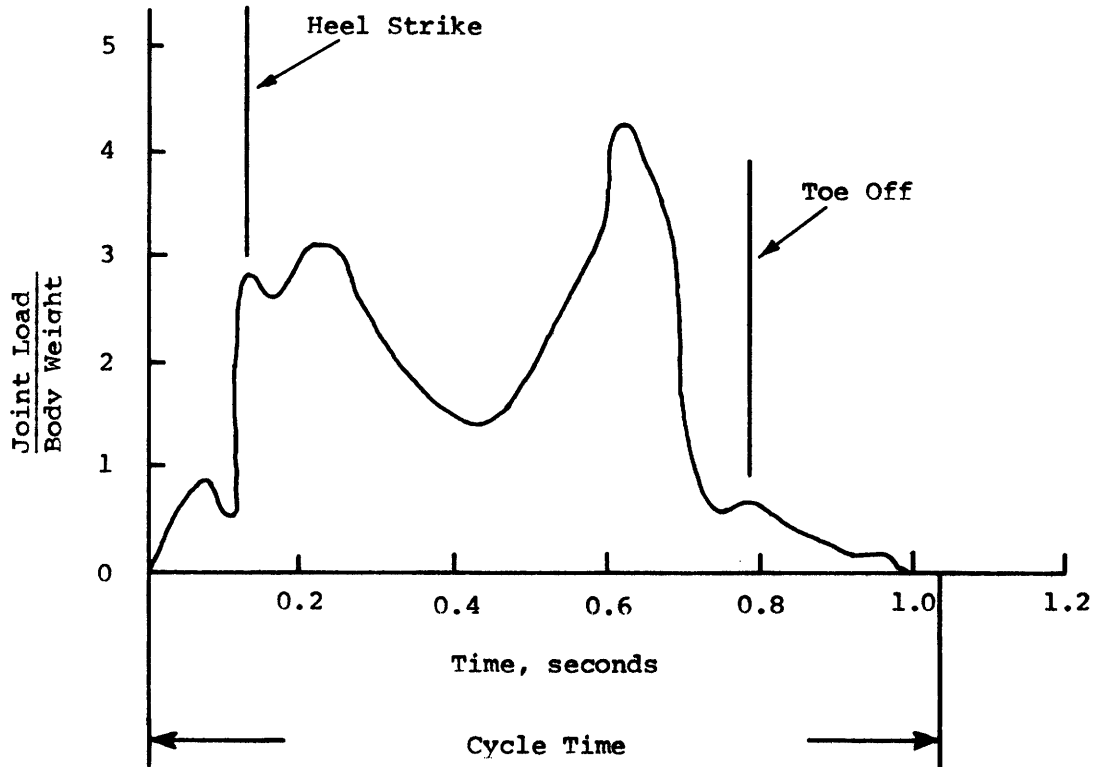


DIAGRAM OF JOINT STRUCTURE.

Figure 3



Hip Joint Load During Walking.
(Paul, Ref. 3)

Figure 4

Rydell (Ref. 5) in two older adults 51 and 56 years of age. These in vivo measurements were accomplished by replacing the head and neck of the femur by a hip prosthesis which had been instrumented to measure the loads carried by the prosthesis. Rydell found the peak load during walking in these two cases to be 2 to 3 times body weight. In one case the peak load developed during running was 4.3 times body weight.

Role of Magnitude and Distribution of Load in Osteoarthritis

Paul's data show that the peak instantaneous load carried by the hip joint can easily be as large as 1000 lb for a 150 lb person. The magnitude of these loads suggests the possibility of a correlation between the loads carried by the joint and joint cartilage deterioration, such as is observed in osteoarthritis. Relatively large localized loads on cartilage tissue are known to be a contributing factor in osteoarthritis once the process of cartilage destruction has begun, but the role that high loads per unit area play in initiating osteoarthritis is unknown. A knowledge of the magnitude and distribution of loads over the cartilage surfaces in normal hips would be of significant value in studying the causes not only of osteoarthritis but also of other diseases that result in deterioration and destruction of joint structure.

Joint Lubrication

The coefficient of friction of articular cartilage is remarkably low. Charnley (Ref. 6) has measured the coefficient of friction in normal joints and has found it to be on the order of 0.005 to 0.023. Several modes of joint lubrication have been proposed to account for these low values and to explain why articular cartilage exhibits

very low wear rates. Hydrodynamic lubrication was suggested by MacConaill (Ref. 7). Charnley (Ref. 6), noting that hydrodynamic lubrication is not likely under slow, reciprocating motion, has proposed boundary lubrication in which there is contact between the opposing cartilage surfaces. Elasto-hydrodynamic lubrication, which takes into account the elasticity of the bearing surfaces, has been proposed as a mode of lubrication by Tanner (Ref. 8). More complex schemes of joint lubrication have been theorized which take into account the composition and rheological behavior of synovial fluid and the porous, anisotropic structure of cartilage. McCutchen (Ref. 9) has suggested that synovial fluid is squeezed out of the cartilage into the joint space as the joint is loaded, thereby maintaining synovial fluid between the opposing cartilage surfaces. McCutchen calls this form of lubrication "weeping lubrication." Longfield, Dowson, Walker and Wright (Ref. 10) have proposed a lubrication mechanism termed "boosted lubrication" which takes into account the surface irregularities of cartilage. They suggest that pools of concentrated synovial fluid are trapped in shallow depressions in the cartilage surface and that these pools maintain a lubricating film on the cartilage surfaces during adverse loading conditions.

The understanding of joint lubrication would be significantly enhanced if the pressure distribution over the cartilage surfaces were known. The mode of lubrication for certain loading conditions could possibly be inferred by examining the corresponding pressure profiles. For example, the pressure profile generated under boundary lubrication conditions could be expected to differ markedly

from the pressure profile generated under elasto-hydrodynamic conditions. The pressure gradients on the cartilage surface could also indicate the direction of flow, or the tendency of flow, of synovial fluid along the cartilage surfaces.

A knowledge of the location and extent of the cartilage surfaces that are actually load-bearing also is useful in lubrication studies. Greenwald (Ref. 11) and Longfield et al (Ref. 10) have found that in autopsied hips the initial area of contact between the femoral head and the acetabulum for low joint loads occurs around the periphery of the acetabulum. Greenwald found that contact between the femoral head and the dome of the acetabulum did not occur for loads of less than one-half body weight. The actual area of contact in the in vivo situation could easily be determined by examining the pressure distribution between the cartilage surfaces.

Modelling of Cartilage

The functional behavior and load-carrying ability of cartilage can be studied by the use of models at both the microscopic and macroscopic levels. Such models could indicate the behavior of cartilage under normal and abnormal conditions. A model that adequately describes the behavior of cartilage and synovial fluid at the microscopic level could be expanded to represent a larger region of cartilage. The development of a suitable model would be promoted by information on pressure magnitude and distribution. The validity of such a model could be established by comparing the pressure distribution predicted by the model with the actual in vivo pressure distribution for similar loading conditions.

Improvements in Hip Prostheses

The pressure measurements may suggest changes in current designs

of hip prostheses. For instance, the Moore prosthesis that replaces only the ball portion of the joint presently is available in one-sixteenth inch size increments. The measured pressure distribution may indicate that the fit between the ball of the prosthesis and the socket should be better than what is currently assumed to be satisfactory, thus indicating a need for a selection of prostheses with smaller increments between sizes. The pressure distribution might also suggest the desirability of a prosthesis with an elastic surface whose characteristics match those of cartilage.

CHAPTER 2

THE PRESSURE MEASURING SYSTEM

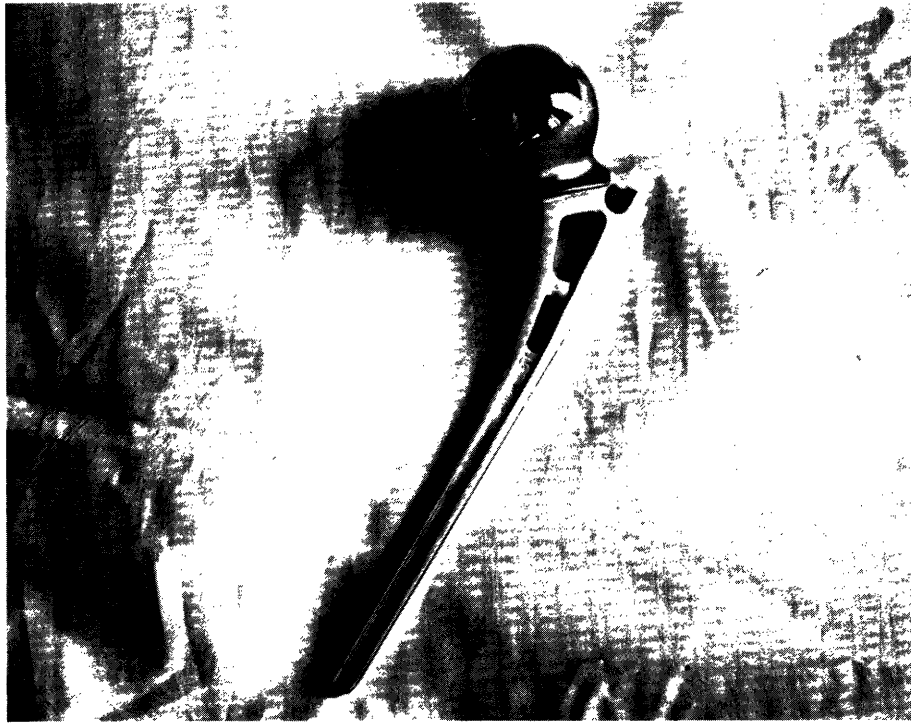
Basic Approach

The proposed method of determining the cartilage surface pressure distribution is to measure the pressure distribution in vivo by replacing the femoral head in a human by a suitably instrumented Moore prosthesis. The Moore prosthesis, shown in Figure 5, is a standard surgical device that is commonly used when the head and/or neck of the femur has been irreparably damaged but the acetabulum and its cartilage surface are intact. The prosthesis is fabricated in two parts, a hemisphere and a stem, as shown in Figure 6. These two parts are welded together, producing a device with a hollow ball.

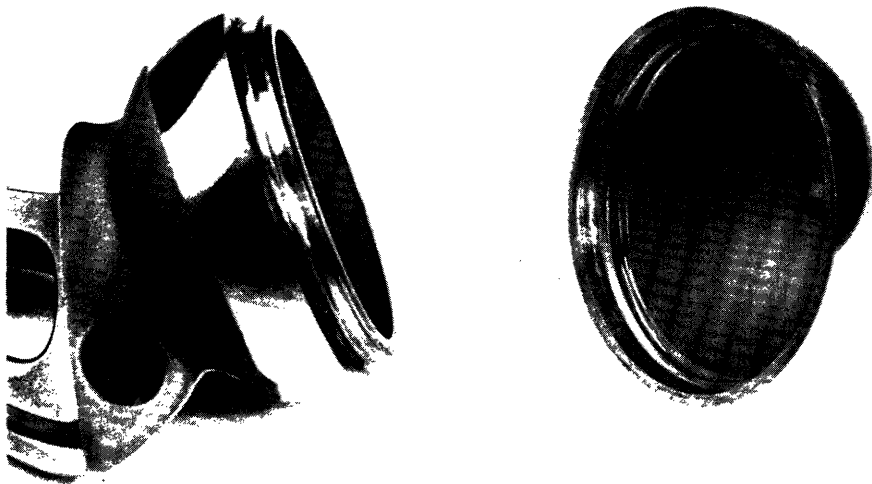
The hollow ball on the prosthesis serves as a convenient vehicle for introducing appropriate pressure transducers into direct contact with the cartilage surface in the acetabulum. These transducers will measure the pressure at a number of points on the surface of the ball, and the pressure distribution can then be reconstructed from these measured values.

Why Human Experimentation

The intent of this investigation is to study the pressures acting on the cartilage surfaces in a human hip. The decision to perform this investigation using humans is based on several considerations. First, tests performed in animals would yield significant data, but these data would not directly relate to the human situation because of the differences in joint structure and gait. Second, the



Standard Moore Prosthesis
Figure 5



Construction of Standard Prosthesis
Figure 6

interpretation of the measured pressure distribution in the human hip will be enhanced by the existing large body of information on the human hip. Third, virtually all of the proposed tests require a cooperating test subject to yield useful data.

For these reasons, plus the fact that the functioning of the instrumented prosthesis as a prosthetic device is identical to that of the unmodified prosthesis, it is felt that human experimentation is well justified.

Validity of Method

An instrumented hip prosthesis appears to be the only approach capable of producing the desired information on the spatial and temporal pressure variations imposed on normal cartilage in the human hip. The question now arises--are the pressures in a hip joint in which half of the joint has been replaced by a metal ball typical of the pressures in a normal hip joint? An answer cannot be given with complete certainty, but the pressures in the two cases should be similar if the following considerations are satisfied.

The pressures on the hip joint surfaces are determined by the magnitude and direction of the loads on the joint, the load-carrying area of the joint, and the viscoelastic nature and lubricating characteristics of cartilage and synovial fluid. The magnitude and direction of the loads are a function of the geometry of the joint, the surrounding muscles and the forces developed by these muscles. The standard hip prosthesis has been designed to replicate the normal hip joint geometry, and it can be implanted without disturbing the major muscles around the joint. Therefore, the loads

acting on the prosthesis should be the same as in a normal hip.

The load-carrying area of the joint is determined primarily by the cartilage surface in the socket. To insure that the loads are distributed over the normal contact area of the socket, the sphere of the prosthesis must closely match the size of the socket. Fortunately, the hip joint surfaces are very nearly spherical, so that a close fit can be achieved by selectively fitting the ball of the prosthesis in the socket at the time of implantation.

The third consideration, that of the elastic nature and lubrication characteristics of cartilage, is not so easily dealt with. It is not at all certain that cartilage in contact with metal will behave in a manner similar to cartilage against cartilage. However, it seems reasonable to assume that the functioning of the cartilage in the acetabulum in a normal joint is relatively insensitive to the internal behavior of the cartilage on the femoral part of the joint. If the deformation of the cartilage surfaces is small, i.e., if the surfaces remain nearly spherical, it seems plausible that the cartilage-covered ball could be replaced by a metal ball of the same size without greatly upsetting the functioning of the cartilage in the acetabulum. This conclusion is supported by the clinical success of standard femoral head prostheses.

The loss of roughly half of the cartilage in the joint when the prosthesis is implanted will almost certainly have some effect on the distribution and quantity of synovial fluid between the joint surfaces. This change in synovial fluid distribution may cause some variation in the pressure distribution. Just how significant this variation will be is unknown. Since the cartilage in the

acetabulum can be reasonably expected to function normally in the presence of a metal ball, it is hoped that the synovial fluid distribution will not be greatly affected, so that the pressures as measured by the instrumented prosthesis will approach those in a normal joint.

Pressure Measuring System Requirements

Physiological Requirements. Of fundamental concern is the safety and well-being of the test subject. The instrumentation, prosthesis modifications and experimental procedure must all be designed with this basic requirement in mind.

From a medical viewpoint the performance of the instrumented prosthesis should be identical to that of a standard prosthesis. It must be capable of carrying the same loads, have the same expected life, and allow the same range of motions as the unmodified device. The design of the instrumented prosthesis must be such that it can be implanted using standard, accepted surgical techniques. The test subject must not be exposed to any significant danger or discomfort when pressure measurements are made.

Technical Requirements. To accurately reproduce a given spatial pressure distribution the pressures must be measured at a sufficiently large number of points in order to detect all of the "hills and valleys." The density of sampling points required to reproduce a pressure distribution that has abrupt spatial changes is greater than the density of points required to reproduce a distribution that has a smoothly varying surface. Since the spatial character of the pressure distribution on the cartilage in the hip is unknown, the pressures should be measured at as many points on the surface of the prosthesis as is possible.

To accurately reproduce a pressure distribution that varies with time, the frequency response of the measuring system must cover the range of frequency components in the pressure signals.

The pressure fluctuations for various physical activities are not known, but the time-varying load carried by the hip joint as a person walks is known fairly accurately. Assuming that the load fluctuations resemble the pressure fluctuations, a reasonable estimate of the necessary frequency response can be arrived at by determining the frequency content of the load fluctuations. The most easily used data is Paul's, shown previously in Figure 4. The Fourier series expansion of this periodic signal gives the discrete frequency spectrum of this load cycle. The results of a computer analysis of this signal indicate that for this particular load curve the magnitudes of the frequency components beyond the fiftieth harmonic are less than one percent of the magnitude of the largest component. Hence, for walking at a rate of one cycle per second, the frequency components above 50 Hz are negligible. For other activities, however, significant frequency components above 50 Hz may exist. Since the pressure distribution for static conditions also is of interest, frequency response should extend from zero to at least 50 Hz.

Experimental Requirements. Pressure measurements will be desired for a variety of activities, such as walking, running, climbing stairs, etc. This implies that any external equipment required in the measuring system should not encumber the test subject.

It is desirable to be able to measure the pressure distribution

from the time that the prosthesis is implanted in the operating room to at least two years after implantation. Tests will be performed immediately following implantation and periodically throughout the recovery process. Approximately six months is required for the patient to recover essentially normal use of the hip, at which time a second series of tests will be performed. Following these tests the pressure distribution will be measured at extended intervals to detect any time-dependent changes.

The maximum uncertainty in the pressures as measured by the pressure measuring system should be on the order of 5 percent. This accuracy requirement is a compromise between the need for accurate measurements and the complexity of the equipment required to make increasingly more accurate measurements.

Pressure distributions with both spatial and temporal variations up to 50 Hz convey a great deal of information. The data acquisition, processing and display system must be capable of presenting this information in a convenient, comprehensible fashion.

Basic Design Approach. The standard Moore prosthesis has evolved over a period of years into a highly reliable, structurally sound prosthetic device. The design philosophy in instrumenting this prosthesis has been to modify the prosthesis only when necessary and to weigh carefully the consequences of such modifications.

Pressure Measuring Instrumentation

The implanted portion of the instrumentation system that evolved from these requirements basically consists of two subsystems--a network of pressure transducers which measure the pressure distribution on the surface of the prosthesis ball and a multi-channel radio telemetry

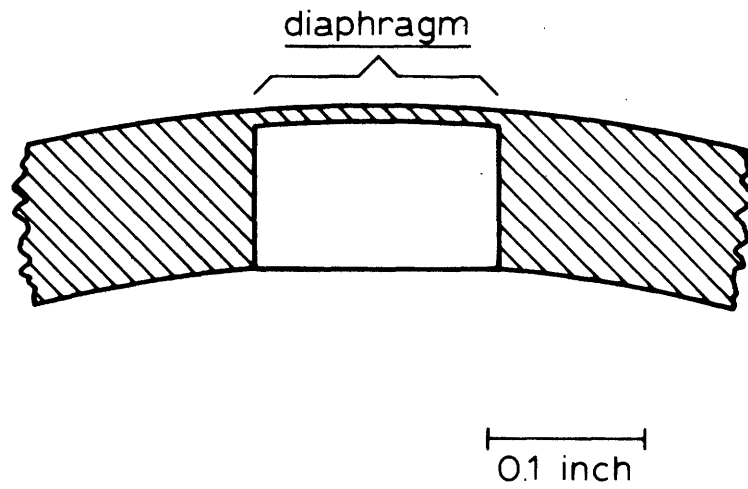
device which transmits the pressure information to external receiving and recording equipment. The telemetry device as well as the pressure transducers are located inside the ball of the prosthesis. The system is powered externally by means of a transformer power induction link. No internal energy storage devices are used.

The Pressure Transducer

Each pressure transducer contains two basic elements--a diaphragm which produces a mechanical motion proportional to the applied pressure, and a motion sensing element that causes an electrically measurable parameter to change in response to the diaphragm motion.

Pressure Sensing Element. A shallow, spherical diaphragm was chosen as the most suitable means of converting pressure into mechanical motion. The diaphragm, shown in cross section in Figure 7, is machined by an electric discharge machining process directly into the inside wall of the ball of the prosthesis. The diaphragm is of uniform thickness so that accurate calculations of the stresses and strains in the diaphragm can be obtained from shell theory. This type of diaphragm preserves the sphericity of the outer surface of the ball, and there is no external indication of the transducer location.

Pressure Transducer Diaphragm Dimensions. Several factors must be considered in choosing the diameter and thickness of the diaphragm. It is desirable to minimize the diameter of the diaphragm so that a number of them may be constructed in the ball without seriously weakening it. In addition, the smaller the diameter, the more closely the transducer approximates measuring the pressure at a "point." On the other hand, a small diameter necessitates a thin



CROSS SECTION OF TRANSDUCER DIAPHRAGM .

Figure 7

diaphragm if reasonable transducer sensitivity is to be achieved. The minimum thickness of the diaphragm is determined by the uncertainty in the machining processes used to produce the diaphragm; the diaphragm should be much thicker than machining uncertainties so that variations in thickness do not significantly influence the stresses in the diaphragm.

The peak pressure that the diaphragm is expected to encounter during the lifetime of the prosthesis is 1000 psi. This figure is based on a hip joint load of 1500 lb and an assumed sinusoidal pressure distribution over the load-carrying area of the prosthesis. The details of this calculation are presented in Appendix A.

The major loads carried by the hip joint are predominantly cyclic in nature. In view of this, the transducer diaphragm has been designed to withstand repeated cycling between 0 and 1000 psi indefinitely. The endurance limit of Vitallium for reversed bending at 10^8 cycles is approximately 40,000 psi (Ref. 12), and this stress level was used as the maximum allowable stress. Since the yield point for Vitallium is approximately 80,000 psi, a diaphragm designed for an endurance limit of 40,000 psi can withstand occasional pressures of up to 1450 psi* without difficulty.

The diameter of the diaphragm is 0.156 in., and its thickness is 0.0105 in. These dimensions are based on a detailed stress analysis that takes into account the fact that the stresses in the diaphragm are caused not only by pressure on the external surface of the diaphragm but also by slight deformations of the ball as it is subjected to various loading conditions. This stress analysis is presented in

*The material in the diaphragm is not subjected to complete stress reversals, so that the peak stress can be higher than 40,000 psi and still satisfy the endurance limit criterion. The yield stress of 80,000 psi remains as a fixed stress limit. See Appendix B.

Appendix B.

The theoretical stress analysis of the pressure transducer diaphragm was supplemented with an experimental fatigue test in which ten diaphragms were subjected to repetitive cycling between 0 and 1000 psi for 43 million cycles. The ten diaphragms showed no signs of failure at the end of this test. The fatigue test procedure is presented in Appendix C.

Transducer Mechanical-to-Electrical Conversion Element. Two principal methods of sensing the diaphragm motion were considered. In one method strain gages measure the strain on the concave surface of the diaphragm, while in the other method a displacement sensing element measures the inward motion of the center of the diaphragm. Both methods would work well if the edges of the diaphragm were rigidly clamped. Under normal loading conditions the ball of the prosthesis undergoes small elastic deformations, and as a result the edges of the diaphragm cannot be considered as being rigidly clamped. Thus, the outputs of both measuring methods are influenced to some extent by loads applied to the ball other than on the diaphragm.

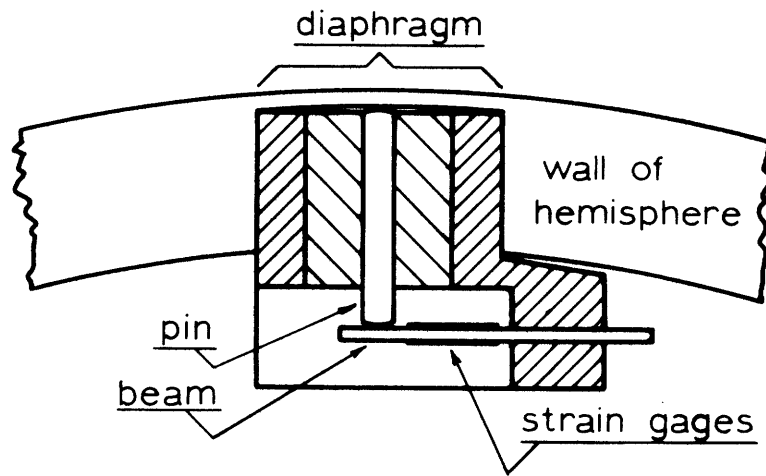
The center-deflection measuring method is considerably less sensitive to remote loads than the surface-strain measuring method. This result is due to the fact that the diaphragm is nearly flat. In the limiting case of a flat diaphragm the surface strain is still a direct function of the radial edge load, but there is no deflection of the center of the diaphragm unless instability is reached. For the transducer diaphragm the error in the output for worst-case conditions is less than 12 percent for the center-deflection measuring method, while for the surface-strain method

the error is on the order of 37 percent.

The displacement sensing element, shown in cross section in Figure 8, consists of a silicon cantilever beam coupled to the center of the diaphragm by a sliding pin. The cantilever beam has four semiconductor strain gages diffused into its surfaces, two gages on the top and two on the bottom of the beam, connected in a four-active-arm Wheatstone bridge. This arrangement maximizes the bridge output and provides good temperature compensation. Fluctuations in bridge output due to temperature changes should be small, since the device will be operating in a stable temperature environment.

A picture of a single pressure transducer mounted in the ball of the prosthesis is shown in Figure 9. The transducer has a sensitivity of $6.6 \mu\text{V}/\text{V}/\text{psi}$ which is constant over the 0 to 1000 psi range. The natural frequency of the transducer is approximately 12 kHz, well above the required operating frequency range of 0 to 50 Hz. If care is exercised in mounting the cantilever beam, there is no detectable hysteresis in the transducer. The deflection of the center of the diaphragm at 1000 psi is 150 μin . Further details on the pressure transducer design and assembly are presented in Appendix D.

A total of fourteen pressure transducers are uniformly distributed over the surface of the hemisphere in the pattern shown in Figure 10. The number of transducers was limited to fourteen because of the increasing complexity of the telemetry system necessary to accommodate more transducers. These fourteen transducers are confined to a 124° sector of the hemisphere because of the prosthesis construction



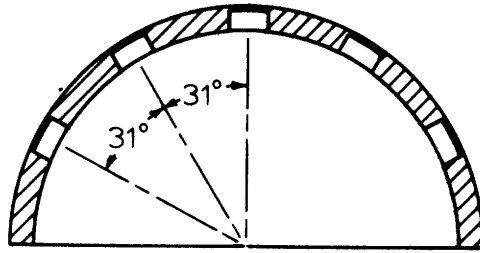
CROSS SECTION OF TRANSDUCER.

Figure 8

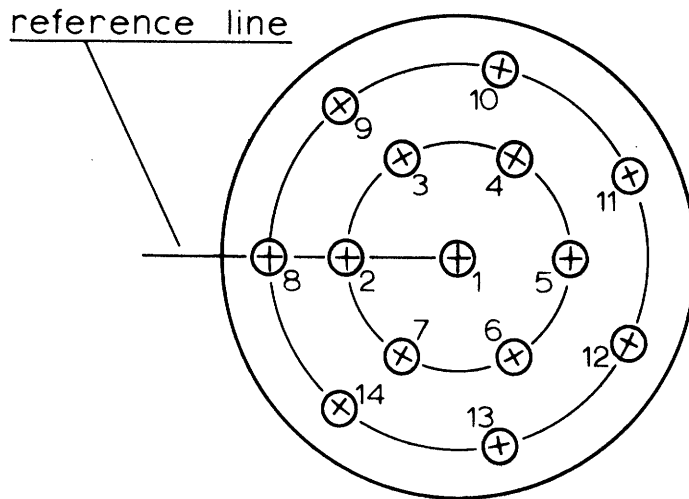


Pressure Transducer Mounted in Prosthesis Hemisphere

Figure 9



side view



bottom view

PRESSURE TRANSDUCER LOCATIONS
IN HEMISPHERE .

Figure 10

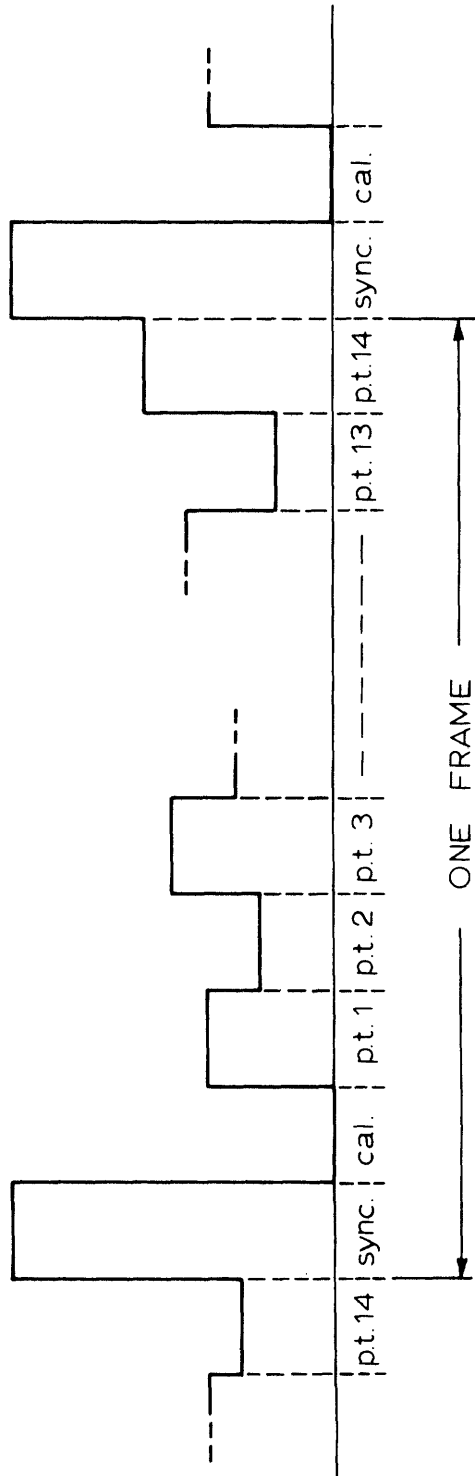
limitations. This pressure sensitive area covers what is expected to be the major load-carrying area on the prosthesis.

The Telemetry System

The signals from the outputs of the pressure transducers are transmitted to external receiving and recording equipment by a PAM/FM (pulse amplitude modulation/frequency modulation) sixteen channel time-multiplexing telemetry system. In this system the output signals of the transducers are sampled in a predetermined sequence by a commutator or multiplexer. The resulting time multiplexed PAM signal is of the form shown in Figure 11, in which the various amplitudes of the signal are proportional to the pressure transducer outputs.

One complete sweep through the sixteen channels constitutes a "frame." The first two channels of each frame are used for synchronization and calibration purposes. The synchronization channel transmits a pulse that can be distinguished from the other signals by its large fixed amplitude. This synchronization pulse is transmitted at the beginning of each frame and thus indicates which pressure transducer is associated with each pulse. The amplitude of this synchronization pulse is about 20 percent larger than the largest expected signal on any of the other channels.

The channel immediately following the synchronization channel is used for calibration purposes and transmits a pulse of zero amplitude. The difference in amplitude between the synchronization pulse and the calibration pulse corresponds to a predetermined pressure. The pressures on the fourteen transducer channels are determined by



TIME MULTIPLEXED PAM SIGNAL .

Figure 11

calculating the ratios of the amplitudes of the transducer signals to the fixed reference amplitude.

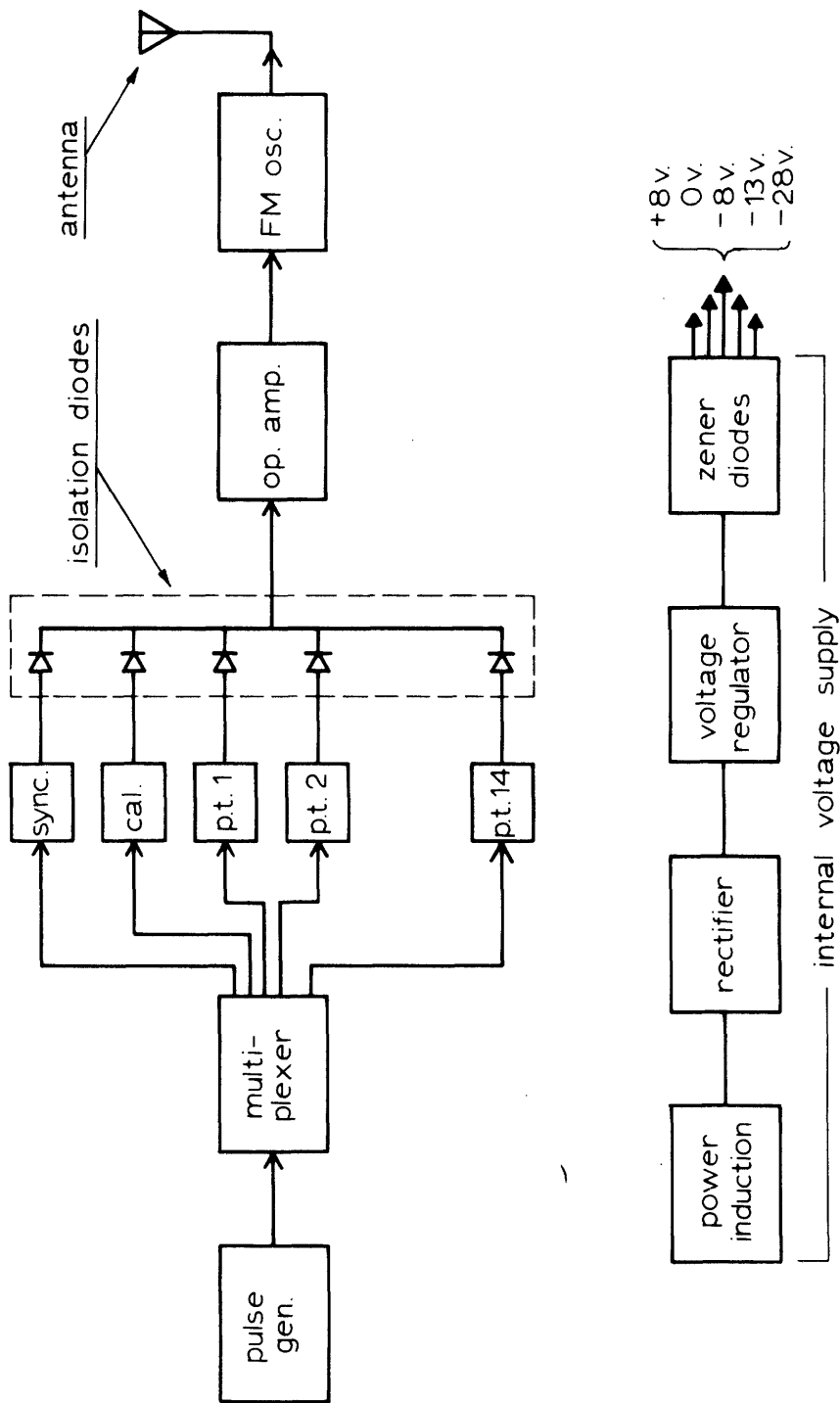
Each channel (and thus each frame) is sampled 250 times per second. This sampling rate theoretically results in an upper frequency response per channel of 125 Hz* and can readily accommodate signal frequencies ranging from 0 to 50 Hz.

A block diagram of the implanted portion of the telemetry system is shown in Figure 12. To minimize power consumption in the transducers, the inputs, rather than the outputs, of these signal sources are switched or commutated. Hence, only one pressure transducer (or the synchronization or calibration channel) is energized at a particular instant. This commutation is performed by the multiplexer (MPXR). The rate at which the multiplexer sequentially excites the sixteen channels is set by the pulse generator. The multiplexer advances one channel for each pulse received from the pulse generator.

The outputs of the sixteen channels are connected to a diode isolation stage that isolates the output of the one channel that is energized from the other fifteen channels. The output of this stage, which is now the time multiplexed PAM signal, is amplified by an operational amplifier. This amplified PAM signal frequency modulates the oscillator/transmitter stage, and the FM signal is radiated by a coil mounted on the tip of the prosthesis stem. The various operating voltages required by the signal processing stages are supplied by the power supply section. Total power required by the implanted device is about 500 mW.

A more detailed description of each of these stages is given in

*This follows from the sampling theorem. See, for instance, Ref. 13.



BLOCK DIAGRAM OF TELEMETRY DEVICE.

Figure 12

Appendix E.

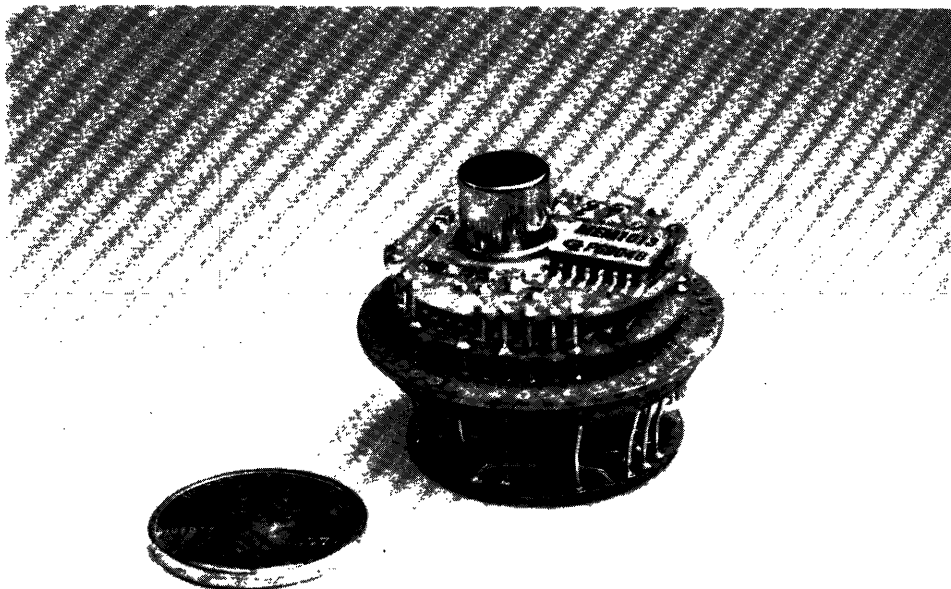
Telemetry Device Construction

The sixteen channel telemetry device is constructed on five circular printed-circuit boards. These boards are supported at their edges by stiff wires which also serve as electrical interconnections between the boards. The telemetry unit prior to mounting in the prosthesis is shown in Figure 13.

Power Induction Circuitry

The implanted telemetry device is externally powered through a simple transformer arrangement. The primary winding of this transformer is a coil which circles the test subject's thigh at the level of the prosthesis stem. The secondary winding is mounted axially on the tip of the stem of the prosthesis and is thus located in the marrow cavity of the femur. (This secondary winding also serves as the radiating antenna for the 100 MHz oscillator.) The telemetry system is energized by slipping the primary winding over the subject's thigh and turning on the power oscillator connected to this winding.

This method of powering the telemetry device has a number of advantages. Since no batteries are used in the device, the problems associated with batteries, such as on-off switches, space requirements, encapsulation of potentially hazardous materials, and low energy storage density (i.e., limited lifetime), are eliminated. The availability of essentially unlimited power and the ease with which relatively high operating voltages can be obtained greatly simplifies the design of the telemetry system. The disadvantages are that the patient has a slightly cumbersome coil around his thigh and must



Telemetry Device Prior to Mounting in Prosthesis

Figure 13

carry a portable power supply in either a back pack or a belt or be connected to a stationary power source by a pair of trailing wires. The inclusion of a coil on the stem of the prosthesis also poses certain design problems, chiefly with respect to the selection of bio-compatible materials.

The power induction system operates at a frequency of 100 kHz. The over-all coupling efficiency is on the order of 10 percent, so that in delivering 500 mW of power to the telemetry system, 5 W must be supplied by the external power source. The power that is lost is dissipated primarily in the external coil. The power dissipation in the tissues in the thigh is very small at this frequency and power level (Ref. 14).

A more detailed analysis of the power induction system is presented in Appendix F.

Data Receiving, Recording, Display and Computation

The 100 MHz signal transmitted by the telemetry unit is received on a standard FM tuner. The PAM signal is recovered at the output of the ratio detector stage of the tuner and is passed through a buffer amplifier and a low pass filter. The buffer amplifier isolates the ratio detector from the recording and data processing equipment, and the low pass filter removes high frequency noise from the signal.

The PAM signal is then recorded on magnetic tape. An instrumentation quality tape recorder operating in the FM mode is capable of recording the PAM signal on a single track. This form of data storage is very convenient, since large amounts of data can be stored compactly, and the data is in a serial format that is ideal for further data processing.

Several forms of data display are possible. The simplest method of data display is to present the PAM signal on an oscilloscope, using the synchronization pulse in the signal to trigger the horizontal sweep of the oscilloscope. The data "frames" are then displayed sequentially, and a quantitative indication of the pressure fluctuation on each channel can readily be obtained.

The spatial variation of pressure is not readily apparent from this simple display. A somewhat more complex display that gives a qualitative presentation of both the spatial and temporal pressure information consists of mapping the pressure sensitive area of the prosthesis hemisphere into a flat circle and displaying the fourteen pressure sensing sites on an oscilloscope, using circles of varying diameter or intensity to indicate the magnitude of the pressure at each point.

A relatively sophisticated method of displaying the pressure information can be produced by determining the pressures at a large number of locations on the hemisphere by interpolating between the fourteen measured points and using this information to draw contour maps. All the data processing necessary for this display is performed by a digital computer, and the contour maps are presented on an oscilloscope.

A digital computer is a necessity to adequately process the telemetered data, since approximately 4000 samples are transmitted each second. Computations, such as integrating the pressure distribution over the surface of the ball to find the magnitude and direction of the resultant force, are possible only if performed by a computer.

To maximize the information gained from the instrumented prosthesis and to minimize the length and frequency of the pressure measuring tests, it is highly desirable to be able to generate the above mentioned data displays in real time at the location where the tests are being performed--in the operating room, at the hospital during the recovery phase, and at other locations. This display capability is possible with the use of a relatively portable digital mini-computer.

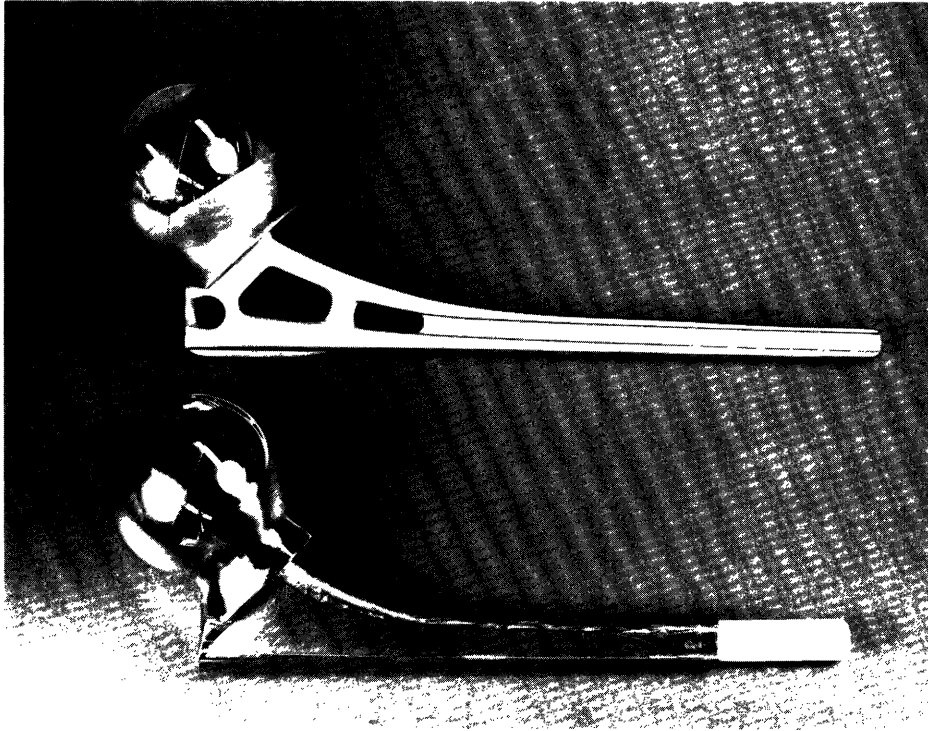
The pressure distribution is measured with respect to the head of the prosthesis. The same pressure distribution occurs on the cartilage in the acetabulum, but its position on the acetabulum can only be determined by knowing the position of the femur relative to the pelvis. Some of the tests will be performed on instrumented walk-ways that have facilities, such as television or high-speed film equipment, for accurately determining the position of the femur, and hence the prosthesis, with respect to the pelvis and acetabulum.

Further information on data receiving and processing is presented in Appendix G.

Prosthesis Modifications

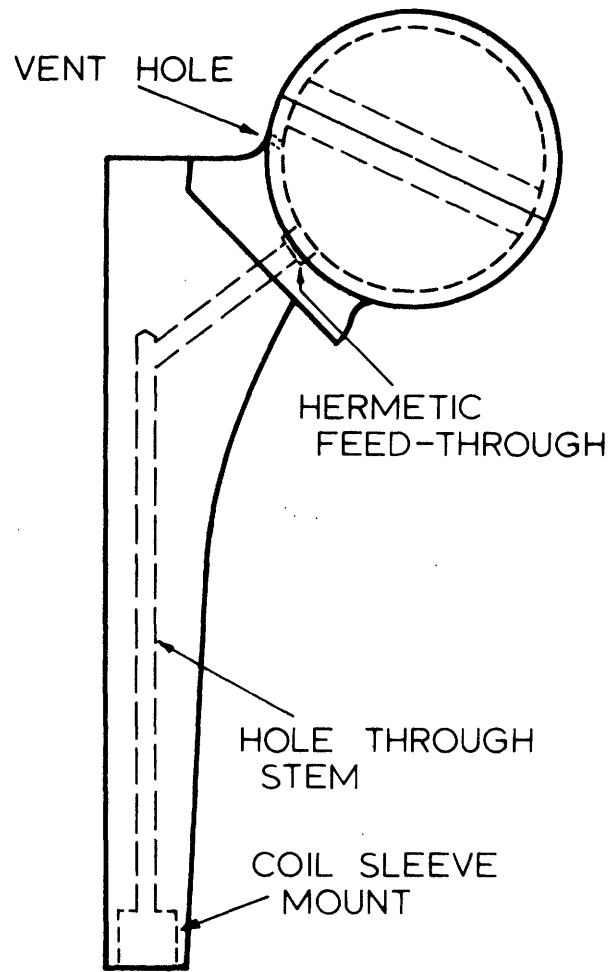
The standard Moore prosthesis and the fully-instrumented prosthesis are shown in Figure 14. The external modifications are confined to the stem, which has been made thicker to accommodate the power induction coil and its encapsulation on the stem tip. The stem is tapered from the ball to the tip and the transverse holes have been eliminated to facilitate removal of the prosthesis if this ever becomes necessary.

A cross-sectional view of the stem is shown in Figure 15. Two intersecting holes are drilled through the axis of the stem as a



Standard and Instrumented Prostheses

Figure 14



SIDE VIEW OF MODIFIED PROSTHESIS
(POWER INDUCTION COIL NOT SHOWN).

Figure 15

passage for the two wires that connect the power induction coil to the telemetry circuitry inside the ball. This hole is filled with medical grade silicone rubber, and the upper end of the hole is sealed by a hermetic feed-through insulator.

The power induction coil is wound on a ferrite core using Teflon[®]-insulated silver wire. The coil assembly is mounted in a Teflon sleeve which is locked to the stem by a series of stainless-steel retaining rings which expand and clamp the Teflon sleeve to a recess machined in the stem tip.

The materials used in this stem modification have been carefully chosen to be as bio-compatible as possible. As a further precaution the stem is assembled in a clean room and the completed stem assembly is then heat sterilized.

After the pressure transducers and telemetry device have been mounted in the ball of the prosthesis, the seam between the hemisphere and stem is welded by electron beam welding. The weld bead is then ground to match the contour of the ball.

The interior of the ball is gas sterilized after the hemisphere has been welded to the stem. This internal sterilization is accomplished through a small vent hole in the wall of the sphere, shown in Figure 15. After the gas sterilization the interior is purged and filled with nitrogen that has been carefully filtered. The vent hole is then welded shut.

Prior to implantation the external surfaces of the prosthesis are gas sterilized, allowing sufficient time before implantation to insure that the Teflon sleeve is fully degassed.

The details of the prosthesis modification, assembly and sterilization are presented in Appendix H.

Proposed Experimental Procedure

Candidate Selection. It is anticipated that several of these instrumented prostheses will be implanted in individuals who are candidates for hip reconstruction utilizing the Moore type of prosthesis and who can be expected to regain essentially normal use of their hips.

The initial implantation will be performed in a woman in her late 50's or early 60's who weighs 150 lb or less. Data obtained in this first implantation will suggest guidelines for the selection of subsequent candidates in terms of age, weight and athletic ability.

Implantations will be performed only after the informed consent of the candidates has been obtained.

Surgical Procedure. The instrumented prosthesis will be implanted using standard surgical techniques. The prosthesis is fastened in the femur by reaming out a cavity in the femur somewhat larger than the stem of the prosthesis. An appropriate amount of polymethyl methacrylate is placed in the cavity, and the prosthesis stem is then inserted into the femur by hand. A small hole drilled through the side of the femur at the bottom of the cavity allows air and excess polymethyl methacrylate to escape.

This procedure subjects the prosthesis to a minimum of shock loads and allows the patient to become ambulatory within a few days after implantation.

At the time of implantation three prostheses having ball diameters of $1 \frac{3}{4}$, $1 \frac{13}{16}$ and $1 \frac{7}{8}$ in. will be available to obtain an

optimum fit between the prosthesis and the hip socket. If none of the three prostheses is suitable an appropriately sized standard prosthesis will be used.

Test Program. While the patient's hip is open each of the three prothesis will be temporarily placed in the hip socket, and the pressure distribution generated by hand loading each of the three sizes will be measured. Immediately following fixation of the appropriate prosthesis in the femur the patient's leg will be moved through a range of motions to verify that the prosthesis is functioning normally and also to obtain baseline measurements of pressure distribution.

The pressure distribution will be measured periodically for several months following implantation to monitor the changes in distribution that may occur during this period and also to evaluate the effects of the graduated series of exercises that the patient undergoes as he recovers the use of his hip.

Approximately six months after the operation when the patient has regained essentially normal use of his hip, a series of tests aimed at obtaining detailed pressure information will be conducted. These tests will be performed during a variety of activities, such as standing, walking, running, climbing stairs, etc.

The pressure distribution will be measured at intervals over a period of two or more years to evaluate long-term changes in the pressure distribution. Additional implantations will be performed after the performance of the initial implantation has been evaluated. The results of the first implantation may indicate a need for changes in the instrumentation, such as the location and sensitivity

of the pressure transducers.

CHAPTER 3

SUMMARY

A prototype of the pressure measuring prosthesis has been constructed to verify the performance of the pressure measuring system. The prototype is essentially identical to the three prostheses that will be prepared for the initial implantation.

Preliminary testing of the prototype indicates that the device performs satisfactorily. The telemetry system operates reliably, and the transmitted 100 MHz signal is stable and has an adequate signal-to-noise ratio at a range of twenty to thirty feet with the coil on the prosthesis stem immersed in a saline solution. The external power oscillator and induction coil adjustments are readily accomplished. The individual pressure transducer channels have not been calibrated, but the transducers appear to operate normally.

In summary, the pressure measuring prosthesis appears to be a workable device. The ultimate test of the device will be in the in vivo situation.

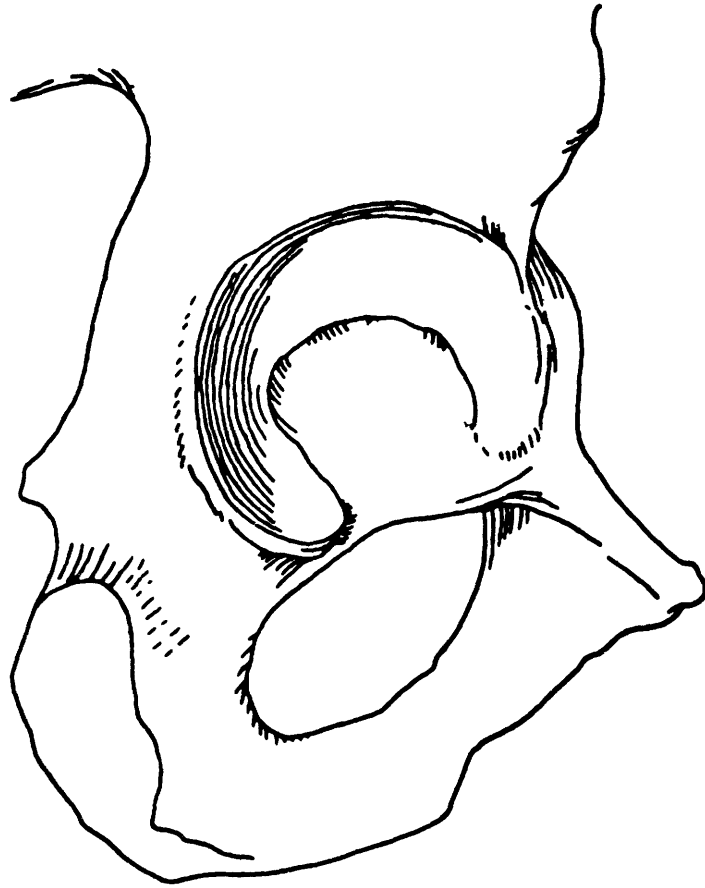
APPENDIX A

ESTIMATE OF PEAK PRESSURE IN THE HIP JOINT

One important factor in determining the dimensions of the transducer diaphragm is the peak pressure that the diaphragm may experience when the instrumented prosthesis has been implanted. No measurements of pressure on cartilage tissue are available, so it is necessary to arrive at an estimate of the peak pressure by making some assumptions concerning the peak loads carried by the hip joint and the pressure distribution on the load-carrying surfaces of the joint.

Paul (Ref. 4) has found that the peak loads during walking can be as large as 5 to 7 times body weight for young adults. The peak loads measured by Rydell (Ref. 5) in an older adult while running were approximately 4.3 times body weight. For design purposes a figure of 10 was chosen as the ratio of peak hip joint load to body weight. This load ratio may be exceeded in a normal athletic person, but for an older person with a hip prosthesis who probably will not engage in strenuous exercises this figure seems reasonable. A peak load ratio of 10 seems particularly conservative when compared to Rydell's figures which were measured directly in a prosthetic hip in an older individual, a situation identical to that of the pressure measuring prosthesis. For a 150 lb person the peak load is then 1500 lb.

The area on the cartilage surfaces where this load is carried is not well defined. The cartilage surface in the acetabulum is roughly U-shaped, as shown in Figure A1. Presumably the major portion of the loads on the joint is carried by the upper area of the cartilage, while the lower areas of the cartilage serve mainly to make the hip joint



A Side View of a Portion of the Pelvis
Illustrating the Acetabulum

Figure A1

[Redrawn from J. C. Boileau Grant, An Atlas of Anatomy (Baltimore:
The Williams & Wilkins Co., 1962), Figure 276]

more stable and are not loaded as heavily as the upper central area.

The pressure distribution on the cartilage in the acetabulum is unknown. It seems reasonable and conservative to assume, however, that for large loads the pressure is distributed smoothly over the cartilage surface with the pressure being a maximum at the center and decreasing to relatively small values at the edges of the load-carrying area. This pressure distribution yields a larger peak pressure than the uniform pressure distribution that Greenwald (Ref. 11) suggests.

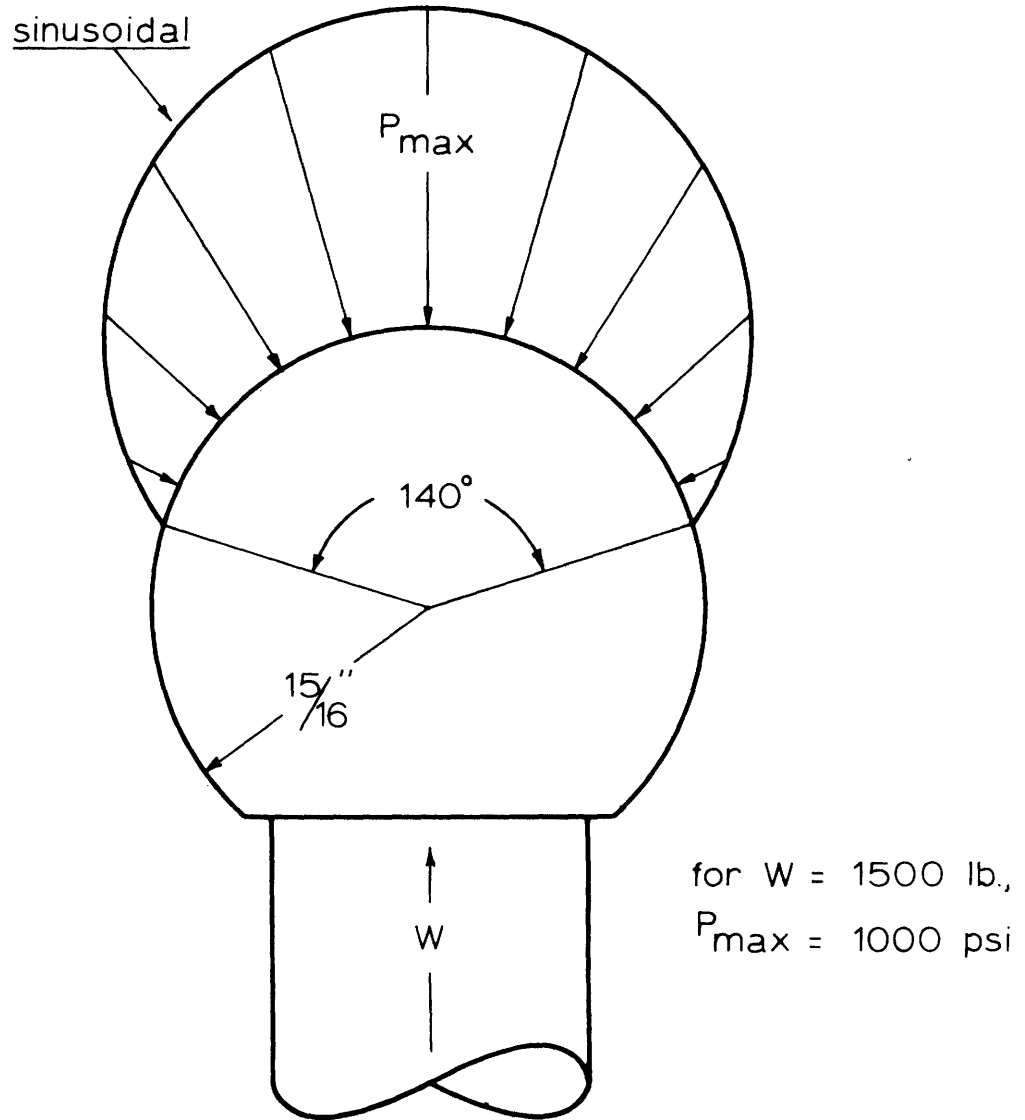
For computation purposes the pressure distribution is assumed to be sinusoidal over a 140° solid angle on the 1 7/8 in. diameter sphere, as shown in Figure A2. The 140° angle roughly approximates what is estimated to be the main load-carrying area of the acetabulum, and a sinusoidal pressure distribution gives a smoothly-varying function with a maximum at the center and zero at the edges. The relation between peak pressure and hip joint load is found by integrating the pressure distribution over the surface of the ball and equating this to the applied load. The resulting equation is

$$W_b = \int_0^{\phi_1} \int_0^{2\pi} P_{\max} \cos\left(\frac{\pi \phi}{2 \phi_1}\right) \cos\phi R^2 \sin\phi \, d\theta \, d\phi$$

where $\phi_1 = 70^\circ$. This yields

$$P_{\max} = \frac{20W_b}{\pi R^2} \quad \text{where } W_b = \text{body weight,}$$
$$R = \text{radius of ball.}$$

For a 150 lb person the peak pressure under the conditions assumed in Figure A2 is approximately 1000 psi.



ASSUMED PRESSURE DISTRIBUTION FOR
CALCULATION OF MAXIMUM PRESSURE.

Figure A2

This figure of 1000 psi is only an estimate of the peak pressure. The pressures on the diaphragm are expected to range typically from zero to several hundred psi with occasional excursions to perhaps 700 or 800 psi. It is conceivable, however, that under unusual circumstances the peak pressure could exceed 1000 psi, and the diaphragm must be designed to withstand these over pressures without failing.

APPENDIX B

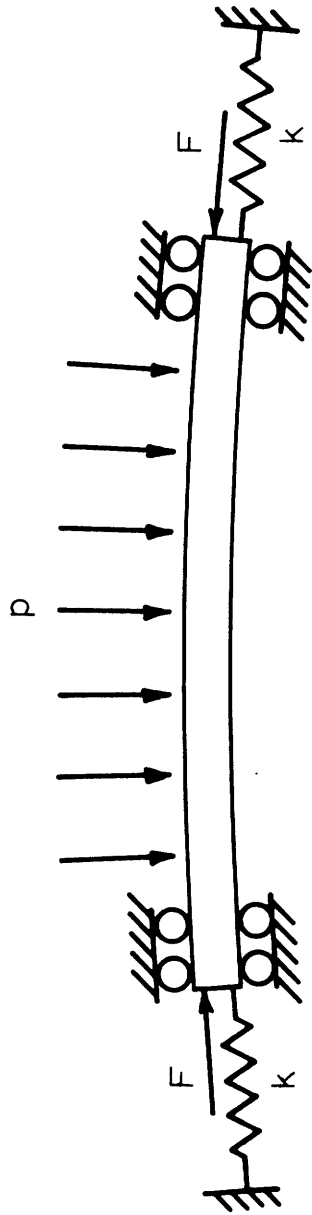
DIAPHRAGM STRESS ANALYSIS

This appendix contains two sections: the first section describes the method of calculating the stresses in the diaphragm and presents the results of these calculations, while the second section contains the equations which yield numerical values for the diaphragm stresses.

Section One: Method and Results

The stress analysis of the diaphragm is complicated by the fact that the circumference of the diaphragm cannot be considered to be rigidly clamped. The sphere of the prosthesis as a whole deforms elastically to a small extent when it is subject to normal physiological loads, and this over-all deformation is sufficiently large to significantly affect the boundary conditions of the diaphragm.

To take into account the variability of the boundary conditions, the edge constraints of the diaphragm are modeled as shown in Figure B1. (The diaphragm is accurately drawn to show its curvature relative to its diameter and thickness.) The edges of the diaphragm are relatively free to move in the radial direction (subject to the restraining springs), and it is assumed that the slope of the diaphragm at its circumference does not change, as shown symbolically by the rollers. It cannot be demonstrated that the actual change in slope at the circumference of the diaphragm is negligible, but this assumption is necessary to make the mathematical analysis manageable. The validity of this assumption is supported by the close agreement of the actual transducer output with the theoretical output based on the model in Figure B1.



MODEL OF SPHERICAL DIAPHRAGM BOUNDARY CONDITIONS .

Figure B1

The springs of stiffness k represent the stiffness of the sphere, while the radial edge load F is a function of the loads applied everywhere except on the diaphragm. The stress applied to the edge of the diaphragm for a given value of F is, therefore, modified by the spring constant k . When $k = 0$ the diaphragm is free to move in the radial direction, and is influenced by the edge force F . When $k \rightarrow \infty$ the diaphragm circumference is rigidly clamped, and the edge force F has no effect in this situation. The applied pressure p is assumed to be uniformly distributed, a reasonable assumption in view of the small diameter of the diaphragm.

The stresses and strains in the diaphragm for specific loading conditions can now be calculated from formulas based on the theory of thin, elastic shells as applied to shallow, spherical shells (Ref. 15,16). This theory assumes among other things that the shell thickness is less than one-tenth of the radius of curvature of the shell and that the deflections of the shell are small. This second assumption permits the theory to be a linear, elastic one, and thus the principle of superposition holds. The calculation of stresses and strains follows an analysis of shallow, spherical shells by Wan (Ref. 17) which includes solutions for various boundary conditions.

Explicit solutions for the stresses in the diaphragm exist for several sets of boundary conditions, three of which are applicable to the diaphragm model: one, when the edge is free to expand ($k = 0$, $F = 0$) and a pressure p is applied to the surface; two, when the edge is rigidly clamped ($k \rightarrow \infty$) and a pressure p is applied; and three, when the surface pressure is zero and a radial stress is applied to the edge of the diaphragm.

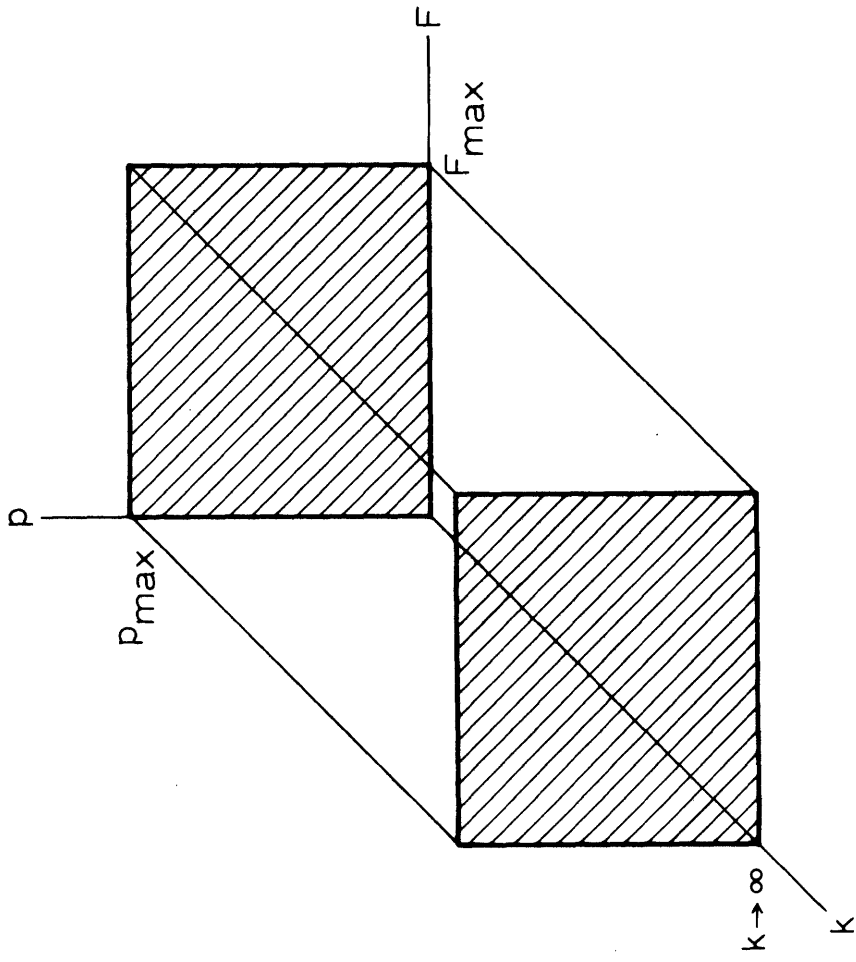
These solutions are not directly applicable to calculating the stresses in the diaphragm. The first two cases assume that k is either zero or virtually infinite, while k for the diaphragm is a finite, non-zero number. In the third case, the radial edge stress is a function of F and k , both of which are unknown.

The situation is illustrated by the "state-space" diagram in Figure B2. The stress state of the diaphragm is completely determined by p , k and F , assuming specific values have been chosen for the diaphragm diameter, thickness and radius of curvature. Thus, each point in the space defined by the coordinates p , k and F represents a particular stress state.

The regions of this state-space in which solutions exist are indicated by the shaded areas. Solutions are readily obtained for all values of p when F and k are zero. Similarly, since the edge stress applied to the diaphragm can be readily computed for a given value of F when $k = 0$, the stresses can be calculated for arbitrary values of F when p and k are zero. (Note, however, that the numerical values of F for the diaphragm are unknown.) Since superposition holds, it is now possible to find the stresses for any combination of p and F when $k = 0$ by algebraically adding the stresses caused by p and F applied separately. This superposition is shown graphically in Figure B3.

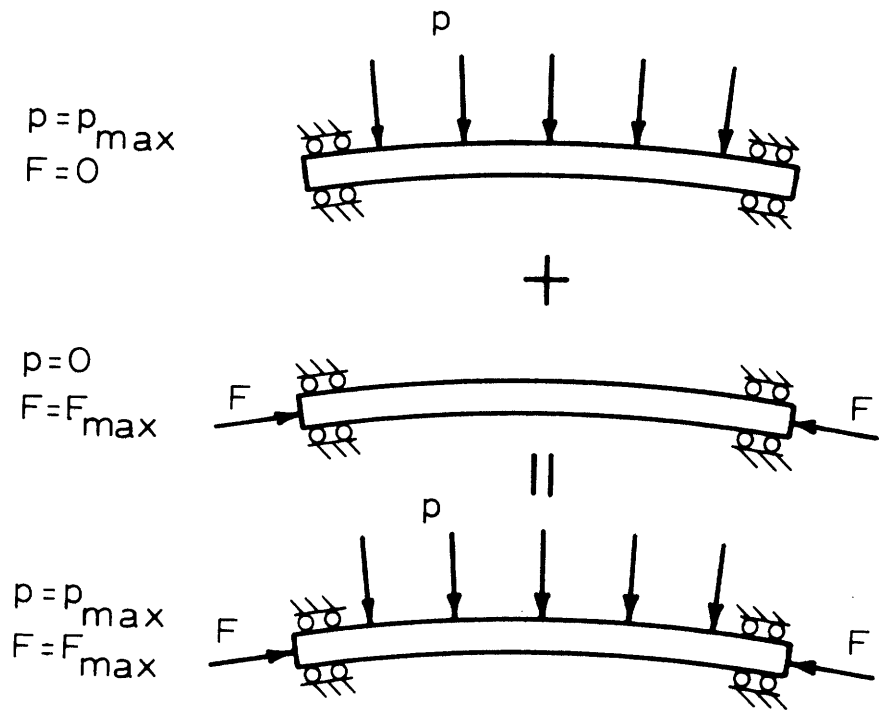
Solutions for the stresses are also readily obtained for all values of p when $k \rightarrow \infty$. In this case F has no influence on the stress state, and hence the stresses in the diaphragm can be calculated for all values of p and F when $k \rightarrow \infty$.

Neither of the two planes in the state-space diagram for which



PLANES IN STATE-SPACE FOR WHICH SOLUTIONS EXIST.

Figure B2



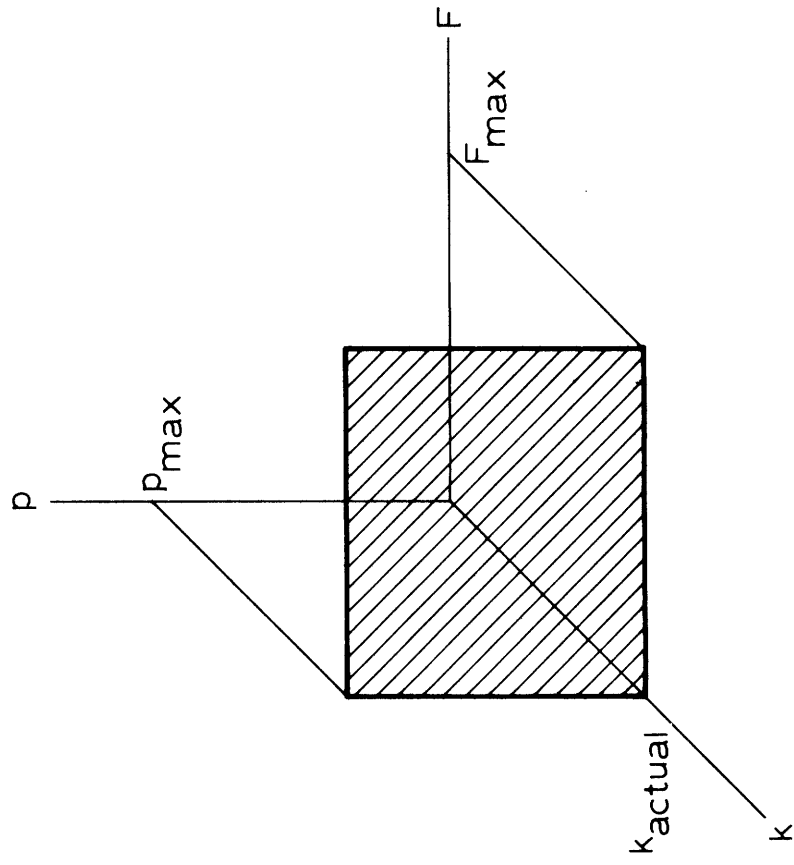
SUPERPOSITION OF LOADING CONDITIONS .

Figure B3

solutions are possible corresponds to the situation for the diaphragm, which has a finite, non-zero value of k . The plane in the state-space where solutions are desired is indicated in Figure B4. Fortunately, several factors permit the stresses in the diaphragm to be determined quite accurately.

First, the equations for the diaphragm displacement and stresses are written in terms of the transverse pressure and the radial edge stress, not k and F . Thus, when $p = 0$, only the radial edge stress due to F must be known to determine the stress state of the diaphragm. The magnitude of the radial edge stress for the situation when $p = 0$ is found experimentally by the following trial-and-error procedure. A hemisphere containing a trial diaphragm is subjected to 1000 psi everywhere on the surface of the hemisphere except on the diaphragm ($p = 0, F = F_{\max}$). The dimensions of this trial diaphragm are based on stress calculations for a transverse pressure p of 1000 psi and an estimated radial edge load. The actual radial edge load is then computed by measuring the center deflection of the diaphragm and is compared to the estimated value. This procedure can be repeated by testing a second trial diaphragm whose dimensions are based on a revised estimate of the radial edge load and again comparing the estimated value to the measured value. In reality, this trial-and-error procedure needs to be done only once to arrive at a sufficiently accurate value of the radial edge load, since the stresses in the diaphragm due to the edge load F are small compared to those due to the transverse pressure p . The radial edge stress determined in this fashion is assumed to be the maximum value due to any load applied to the hemisphere excluding the diaphragm.

The region in the state-space diagram where numerical solutions



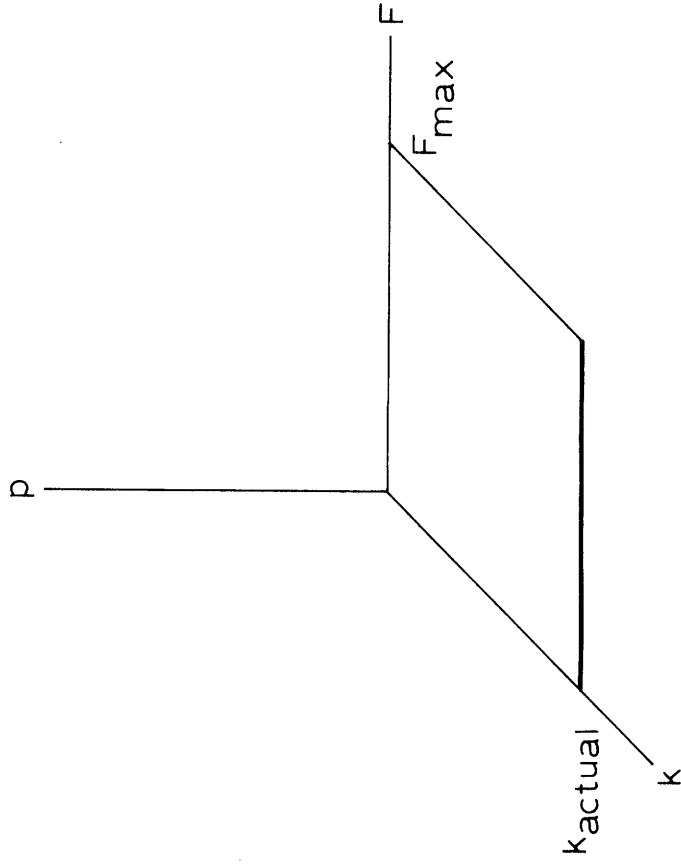
PLANE IN STATE-SPACE FOR WHICH SOLUTIONS ARE NEEDED.

Figure B4

now exist is shown in Figure B5. What remains to be determined are the stress states for non-zero p when $F = 0$ for the value of k corresponding to the actual situation. Two additional considerations eliminate this problem. First, the stresses in the diaphragm due to p are only a weak function of k . This is a consequence of the fact that the diaphragm is nearly flat. In the limiting case of a flat diaphragm the stresses are independent of k for small deflections. Second, because the shell theory is linear, the stresses at any point in the diaphragm increase or decrease monotonically as k goes from zero to infinity. Thus the stresses computed for the two cases $k = 0$ and $k \rightarrow \infty$ for a particular value of p with $F = 0$ place rather close bounds on the actual stresses for that value of p . These considerations provide solutions in the region in the stress state-space shown in Figure B6.

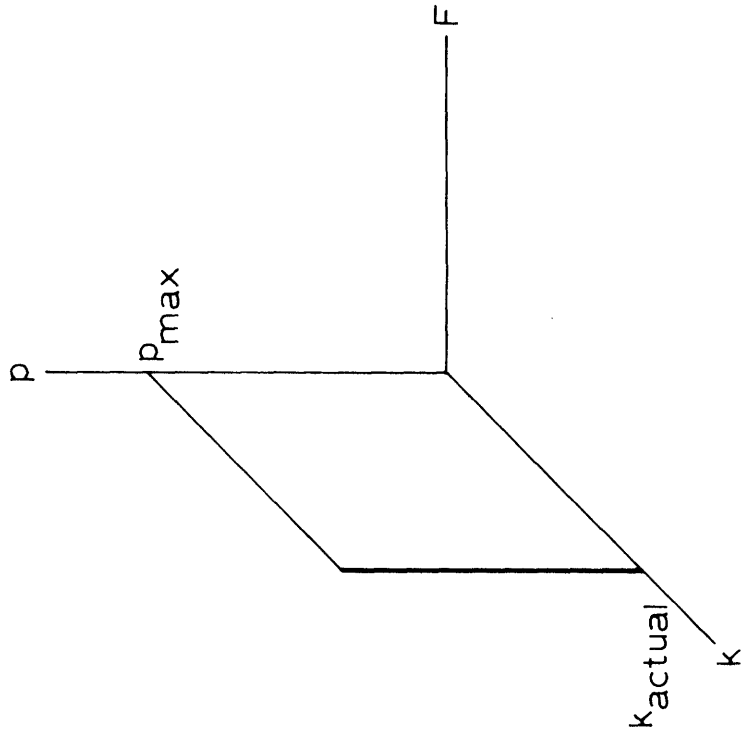
Combining these two solution regions results in the situation shown in Figure B7. The stress states for the actual value of k (k_{actual}) for values of p with $F = 0$ are assumed to be identical with those for $k = 0, F = 0$. The stresses for k_{actual} could have been assumed to be the average of the stresses for $k = 0$ and $k \rightarrow \infty$, but the former procedure is slightly more conservative from a design standpoint. Since the range of radial edge stresses due to the edge load F are now known, the stresses in the diaphragm for any combination of transverse pressure and radial edge stress can now be determined by superposition.

Again, because of linearity, the maximum or minimum values of stress occur at the corners of the state-space rectangle. The trivial case of no loads applied anywhere on the hemisphere is represented by



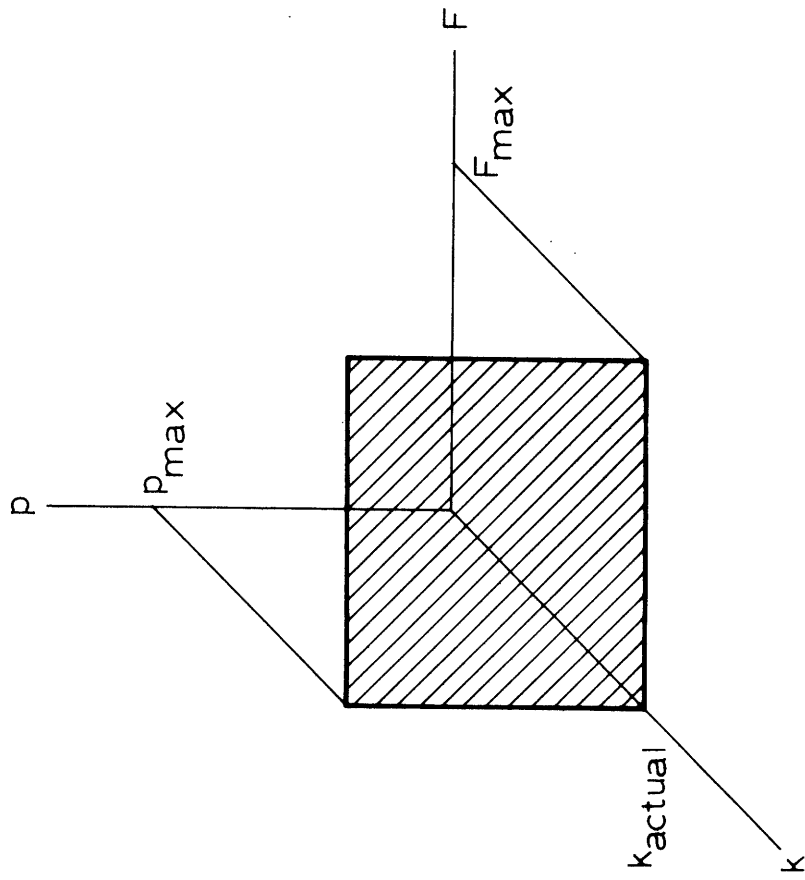
LINE IN STATE-SPACE DETERMINED BY RADIAL EDGE LOAD F .

Figure B5



LINE IN STATE-SPACE DETERMINED BY LIMITING STRESSES
AT $k = 0$ AND $k \rightarrow \infty$ FOR TRANSVERSE PRESSURE p .

Figure B6



REGION IN STATE-SPACE IN WHICH SOLUTIONS NOW EXIST.

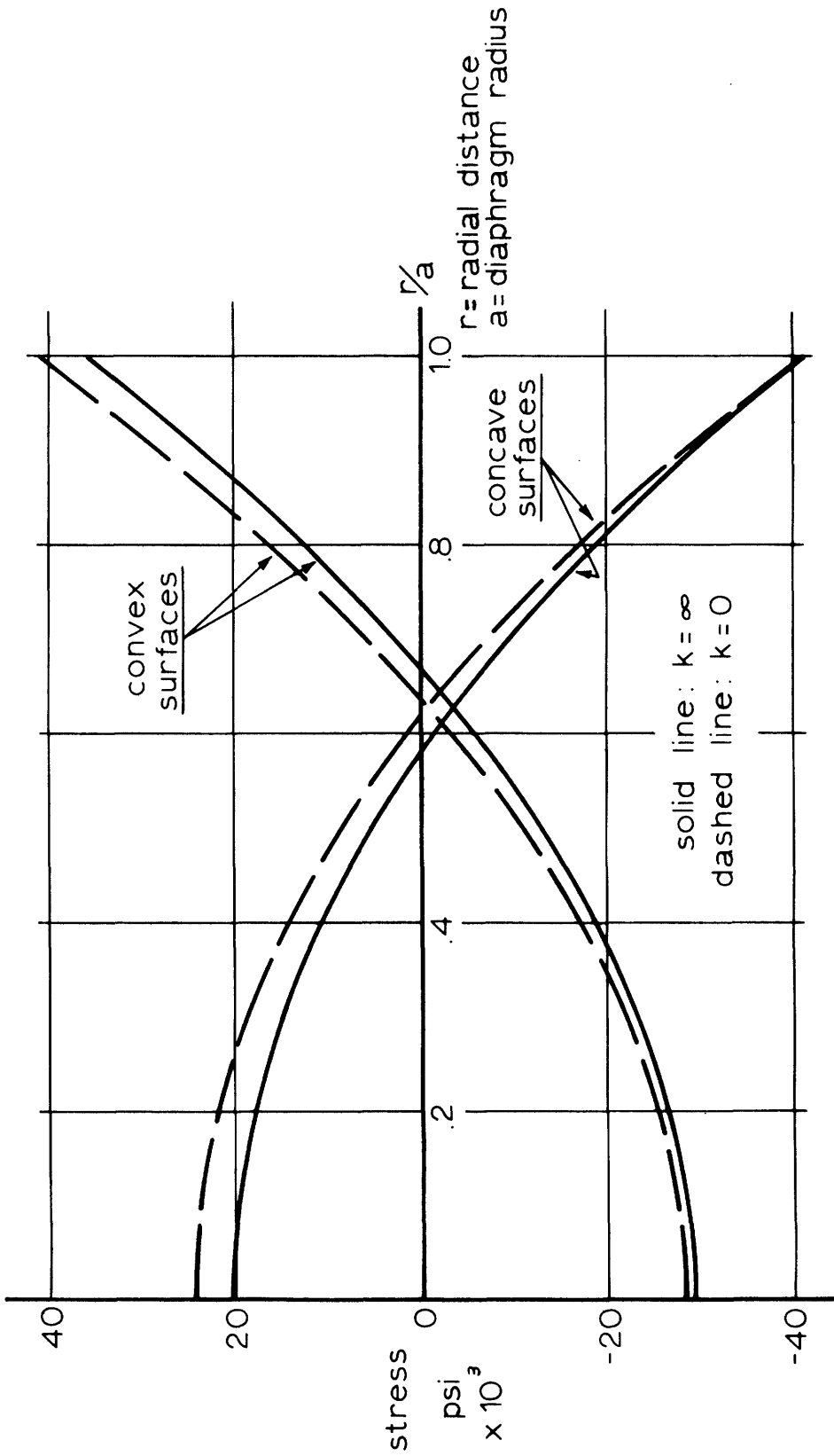
Figure B7

the point $p = 0, F = 0$. The situation when 1000 psi is applied to the diaphragm alone occurs at $p = 1000, F = 0$. The situation of having 1000 psi everywhere on the hemisphere except on the diaphragm occurs at $p = 0, F = F_{\max}$, and the case when the hemisphere is uniformly loaded everywhere to 1000 psi is represented by $p = 1000, F = F_{\max}$.

The resultant stresses in the diaphragm are due to direct and bending stresses. Since bending stresses are present, the highest stresses occur on the surfaces of the diaphragm. This is true for the shear stresses as well as the tensile and compressive stresses. In addition, the magnitudes of the stresses in the radial direction are always equal to or greater than the stresses in the tangential direction, except for small areas of relatively low stress. Figure B8 shows the normal stresses in the radial direction on the concave and convex surfaces along a radius for the two situations $k = 0$ and $k \rightarrow \infty$ when the edge force F is zero. The spring constant k has only a small influence on the stresses. These stresses are principal stresses, since planes perpendicular to the radial and tangential directions are principal planes. The actual stresses on the two surfaces when $F = 0$ lie between the curves for $k = 0$ and $k \rightarrow \infty$.

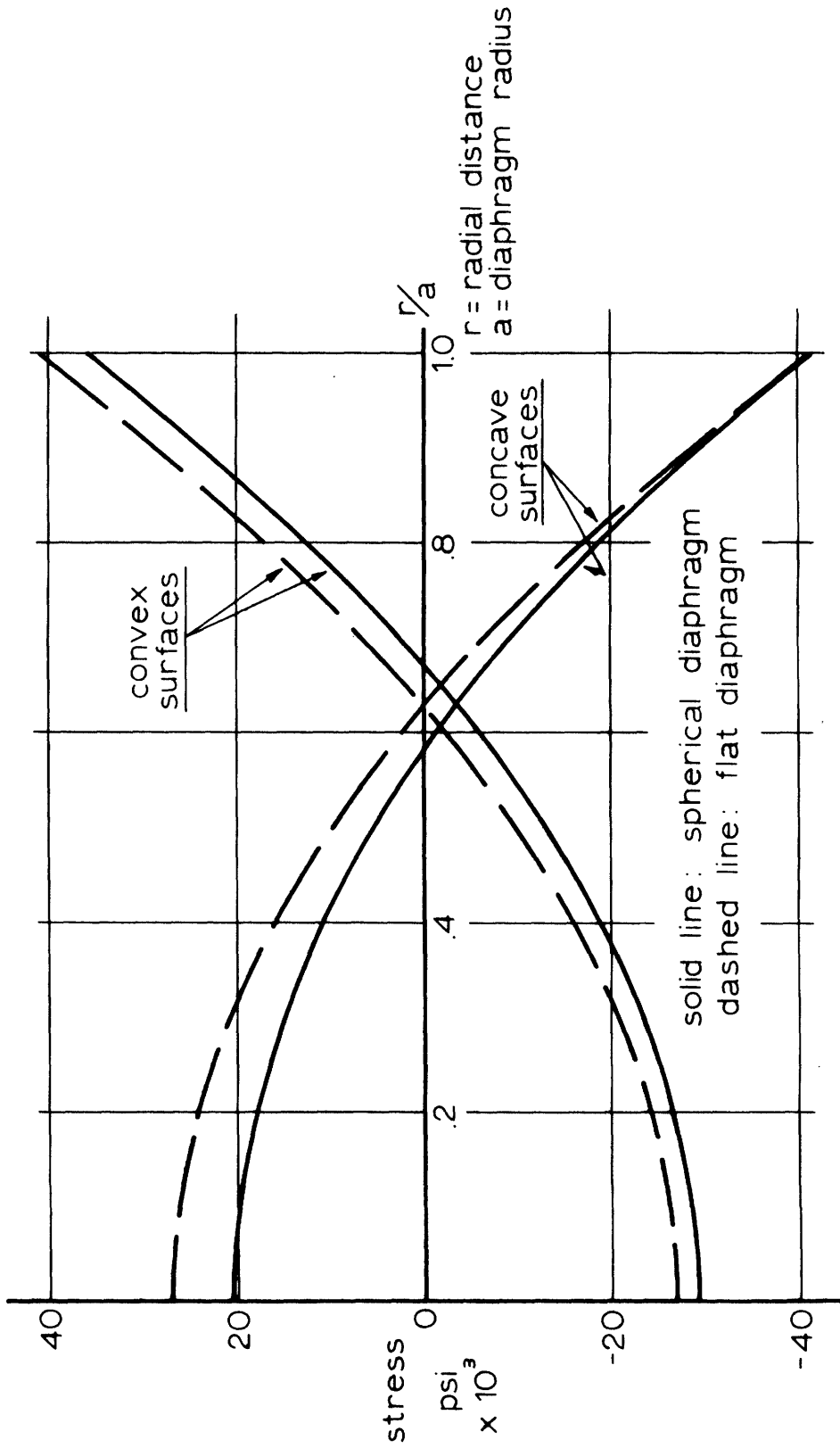
It is interesting to compare the stresses for the $k \rightarrow \infty$ (clamped edge) case to the stresses in a flat diaphragm of the same dimensions. This comparison provides an approximate check of the numerical accuracy of the stress calculations for the spherical diaphragm, since the stresses for the flat diaphragm can be calculated readily from well-known formulas. The results are shown graphically in Figure B9.

Figure B10 shows the radial surface stresses resulting from the maximum edge force F with no transverse pressure p . Note that the



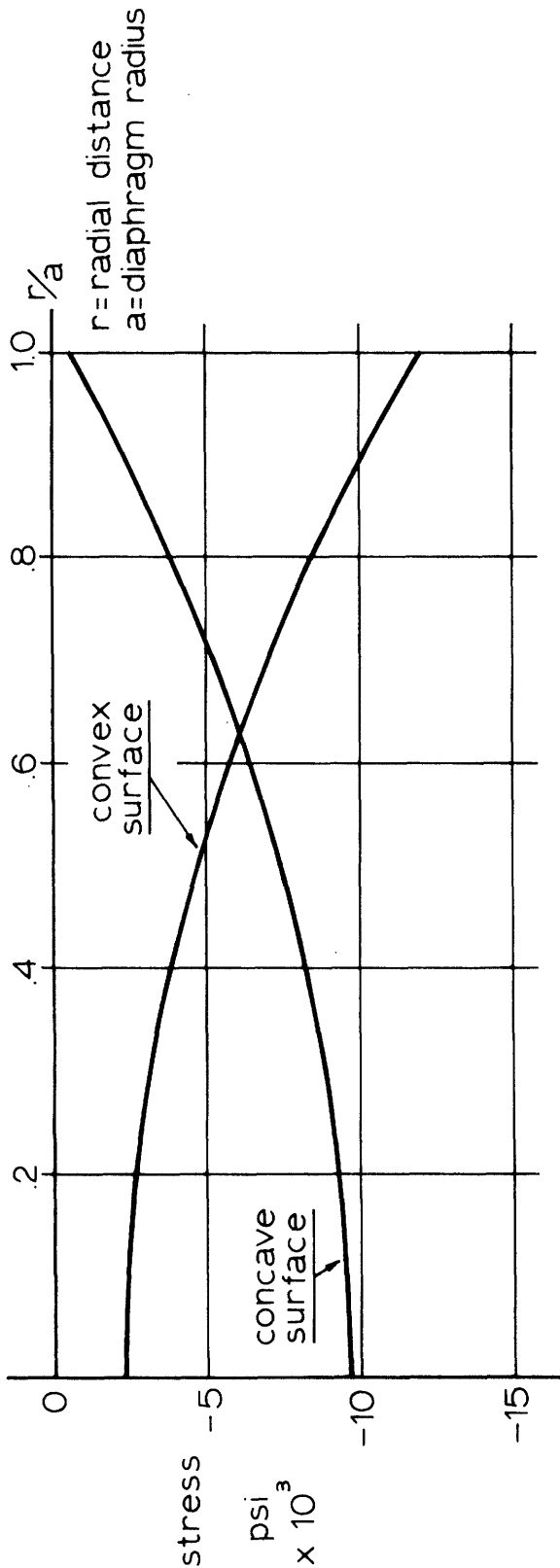
RADIAL STRESSES AT DIAPHRAGM SURFACES DUE TO 1000 PSI APPLIED TO DIAPHRAGM FOR EDGE CONDITIONS $k=0$ AND $k \rightarrow \infty$ WHEN $F=0$.

Figure B8



COMPARISON OF RADIAL SURFACE STRESSES FOR SPHERICAL DIAPHRAGM WITH CLAMPED EDGE ($k \rightarrow \infty$) AND FLAT DIAPHRAGM OF SAME DIMENSIONS. APPLIED PRESSURE IS 1000 PSI.

Figure B9



STRESSES IN RADIAL DIRECTION ON DIAPHRAGM SURFACES
FOR $P=0, F=F_{\text{max}}$

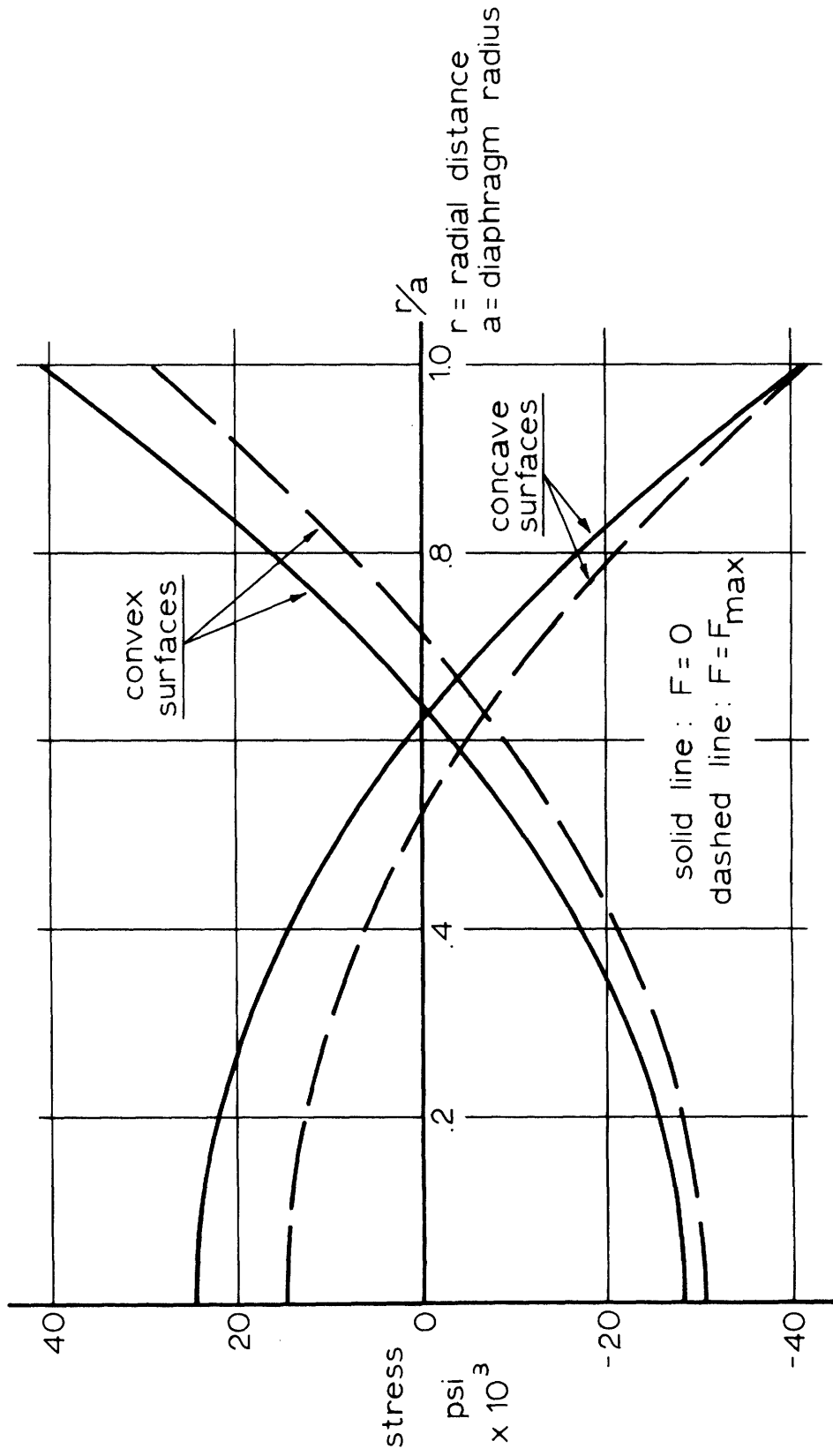
Figure B10

bending stresses very nearly balance the direct stresses at the center on the convex surface and at the circumference on the concave surface.

The stresses due to the edge force F are then added algebraically to the stresses resulting from a transverse pressure $p = 1000$ psi. The combined stresses are shown in Figure B11. Fortunately, the stresses due to F do not significantly increase the stresses in the critical areas. The largest normal stresses occur at the centers and edges of the two surfaces.

Shear stresses in the diaphragm occur on several different planes. The shear stresses whose magnitudes are one-half the difference of the radial and tangential stresses at a point are always less than one-half of the peak radial stress, either because the magnitudes of the two normal stresses are small or the stresses are both tensile or both compressive. The peak shear stresses are caused by radial stresses and are equal to one-half of the normal radial stress at the surface of the diaphragm. Since the endurance limit in shear is generally considered to be one-half the endurance limit in tension (Ref. 18), it is safe to consider only the peak normal stresses in fatigue strength calculations.

There is one additional factor to be considered in determining the stresses in the diaphragm--the stress concentration due to the abrupt change in thickness of the wall of the hemisphere at the circumference of the diaphragm. No tabulated data were found which covered this particular stress concentration geometry, so the stress concentration factor for a similar case (Ref. 18) was used. To be conservative, the stress concentration factor of 1.3 was applied to the appropriate stresses at the circumference of the diaphragm on the convex surface



RADIAL STRESSES AT DIAPHRAGM SURFACES SHOWING EFFECT OF EDGE LOAD F WHEN $k=0$. TRANSVERSE PRESSURE IS 1000 PSI.

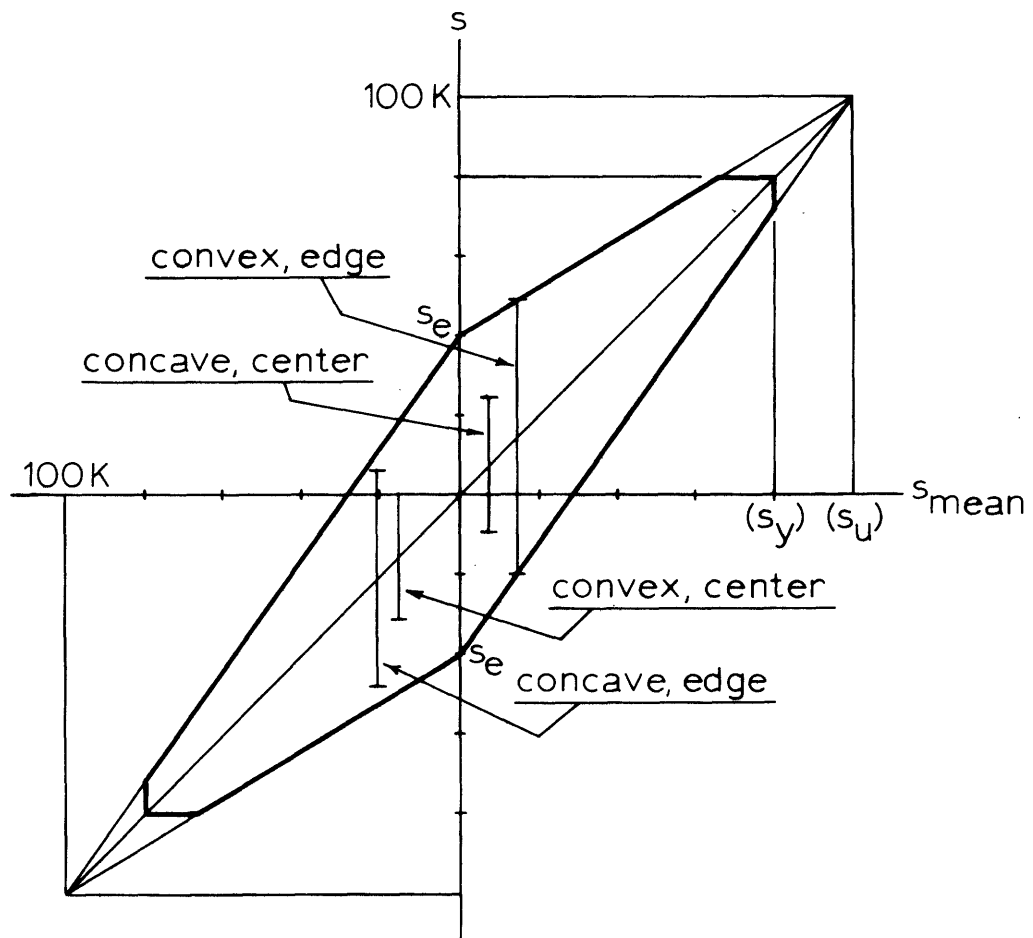
Figure B11

as well as on the concave surface. The accepted procedure for applying the stress concentration factor to cyclic stresses is to apply it to the alternating component of the stress only (Ref. 18).

The endurance limit of Vitallium for reversed bending is 40,000 psi, and the ultimate strength is 100,000 psi (Ref. 12). From these figures one form of the Goodman diagram can be constructed, as shown in Figure B12. The Goodman diagram takes into account the fact that the endurance limit is dependent upon the stress range. As long as the range of stresses at any given point in the diaphragm remains within the limits of the diagram, the endurance limit criterion is satisfied. (The boundaries of the Goodman diagram actually represent the statistical averages of many fatigue tests; they are simply reasonably conservative boundaries between the regions where failing is unlikely and where failure becomes increasingly likely.)

The four vertical lines in Figure B12 indicate the stress ranges under worst-case conditions for the four peak stress areas--the centers and edges of the two surfaces. The critical case occurs at the circumference on the convex surface and occurs when the ball is loaded to 1000 psi everywhere except on the diaphragm followed by removal of all applied pressures except for a 1000 psi load on the diaphragm. In this situation the diaphragm first bows outward, then inward. Figure B12 demonstrates that the diaphragm should be capable of sustaining stresses caused by worst-case conditions indefinitely.

The peak stress in the diaphragm is about 55,000 psi under worst-case loading conditions. Since the yield point of Vitallium is 80,000 psi the diaphragm can withstand occasional pressures as high as 1450 psi without failure.



GOODMAN DIAGRAM SHOWING PEAK STRESS RANGES FOR WORST-CASE CONDITIONS.

Figure B12

Section Two: Equations

The stress analysis of the pressure transducer diaphragm is based on the theory of shells as applied to shallow, spherical shells. The basic differential equations describing the behavior of shallow, spherical shells have been presented by Flügge (Ref. 16) and Timoshenko (Ref. 15) among others, and the solutions to these equations for certain boundary conditions have been derived by Wan (Ref. 17).

The assumptions as stated by Kraus (Ref. 19) under which the differential equations were developed are:

1. The shell is thin.
2. The deflections of the shell are small.
3. The transverse normal stress is negligible.
4. Normals to the reference surface of the shell remain normal to it and undergo no change in length during deformation.

The first assumption, that of a thin shell, is generally understood to mean that the shell thickness is less than one-tenth of the radius of curvature of the shell. The transducer diaphragm is well within these limits, since its thickness is 0.0105 in. and its radius of curvature is nearly 1 in.

The assumption that the shell deflections are small insures that the resulting equations for stress and strain are linear. The deflection of the diaphragm center for an applied pressure of 1000 psi is about 150 μ in., which is less than two percent of the diaphragm thickness.

The third assumption is satisfied by the transducer diaphragm, since the peak transverse normal stress at the outer surface of the diaphragm is 1000 psi, a figure considerably less than the 40,000 psi normal stresses developed in the diaphragm.

The fourth assumption implies that the deflections of all points in the shell are linearly related to the deflection of some reference surface. It is equivalent to the assumption made in developing formulas for stress and strain in beams that plane sections remain plane.

No attempt is made here to present the derivation of the basic differential equation, and readers are referred to texts devoted to the theory of shells. The equations and definitions presented in the next few sections were borrowed freely from Wan (Ref. 17). The material in the diaphragm is assumed to be isotropic, and temperature effects are not considered.

The pertinent differential equations for the transducer diaphragm are:

$$D\nabla^2\nabla^2 w - \frac{1}{R}\nabla^2 F = P_n$$

$$A\nabla^2\nabla^2 F + \frac{1}{R}\nabla^2 w = 0$$

where

- w = transverse component of the middle surface displacement;
- F = stress function representing the direct stress resultants;
- R = radius of the spherical middle surface;
- P_n = pressure applied to the surface in the transverse (normal)

direction;

$$\nabla^2 () = \frac{\partial^2 ()}{\partial r^2} + \frac{1}{R} \frac{\partial ()}{\partial r} + \frac{1}{r^2} \frac{\partial^2 ()}{\partial \theta^2} ;$$

$$A = 1/(Eh);$$

$$E = \text{modulus of elasticity};$$

$$h = \text{shell thickness};$$

$$D = \frac{Eh^3}{12(1 - \nu^2)} ;$$

ν = Poisson's ratio; and

r, θ = polar coordinates in the plane tangent to the apex of
of the shell.

These two differential equations, supplemented by appropriate boundary conditions, constitute the statement of the problem. The solution of these equations consists of the solution to the homogeneous equations and the particular solutions determined by the specified boundary conditions.

The stresses of primary importance in the diaphragm are the principal stresses. Because of symmetry, these principal stresses act in the radial and tangential directions, and they act in directions perpendicular to the normal to the shell surface at the point at which they occur.

The two principal stresses, which will be called the radial stress and the tangential stress, are the sum of two components, the direct stresses and the bending stresses. The direct stresses are of uniform intensity across the diaphragm thickness at a particular point on the diaphragm, while the bending stresses vary linearly from the concave to the convex surface. The stresses due to bending are of equal magnitude but opposite sign on the opposing surfaces at a given point on the diaphragm. Because of these bending stresses the maximum stresses, either tensile or compressive, always occur on the surfaces of the diaphragm.

The differential equations yield solutions in terms of the loads and bending moments per unit length, N_r , N_θ , M_r and M_θ . The quantities N_r and N_θ are the loads per unit length in the radial and tangential directions, and M_r and M_θ are the bending moments per unit

length in the corresponding directions. Figure B13 illustrates the locations of these loads and bending moments. The direct and bending stresses are then calculated from N_r , N_θ , M_r and M_θ by multiplying these quantities by appropriate factors containing the diaphragm thickness "h."

The differential equations describing the behavior of the diaphragm also yield the transverse deflection, w , of the diaphragm.

The desired quantities N_r , N_θ , M_r , M_θ and w are a function of the distance in the radial direction from the center or apex of the diaphragm. To simplify these expressions the radial distance is measured by a dimensionless quantity ρ , which is the ratio of the distance from the diaphragm center to the radius of the diaphragm:

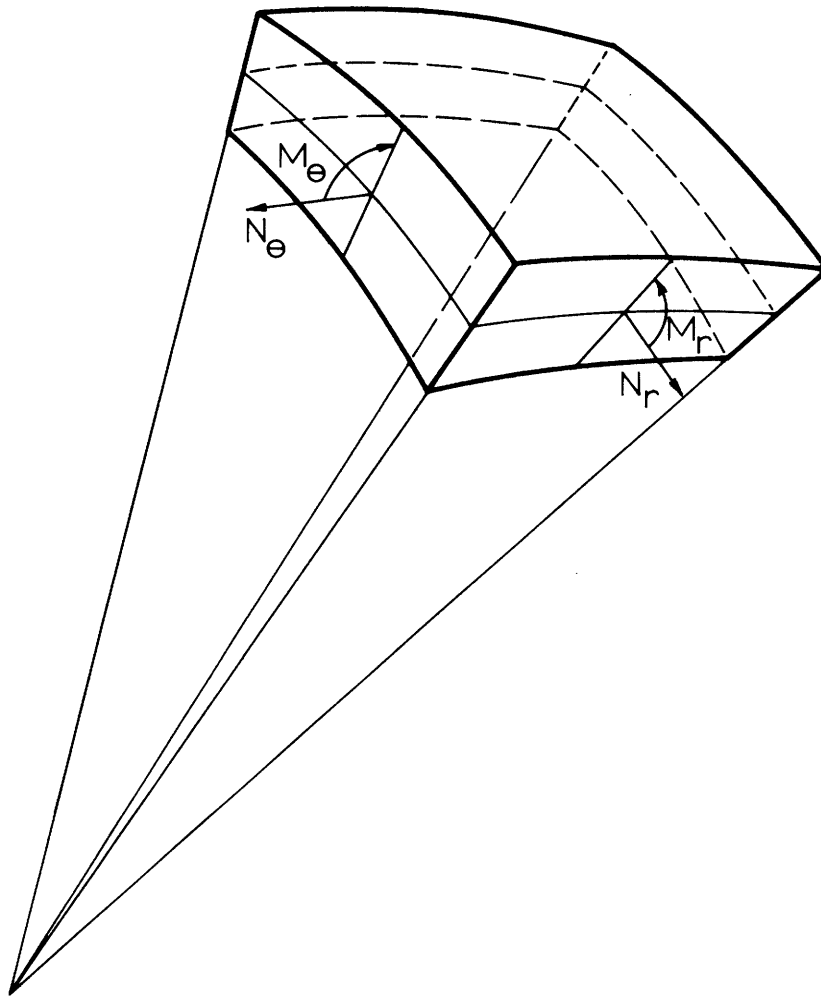
$$\rho = r/a,$$

r = distance from center of diaphragm to a particular point, and
 a = diaphragm radius.

The principal stresses in the diaphragm and the diaphragm deflection were determined for three different boundary conditions, illustrated in Figure B14. These are:

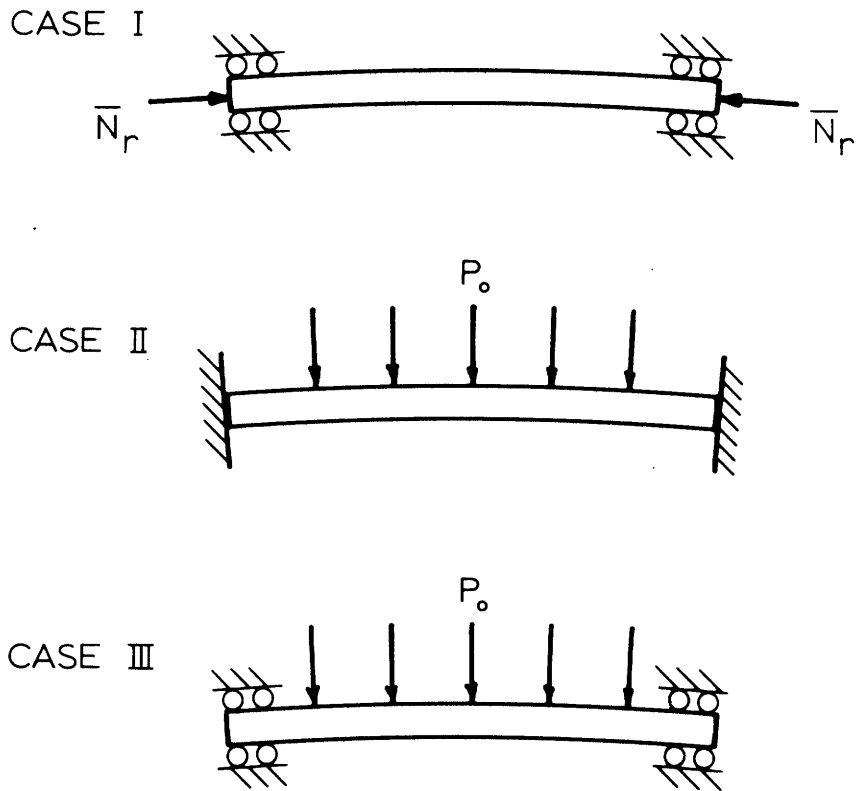
Case I. A radial compressive stress is applied to the circumference of the diaphragm with no pressure applied to the diaphragm surface. This situation arises when a pressure is applied to some or all of the hemisphere except the diaphragm. The worst-case condition is assumed to occur when 1000 psi is applied everywhere except on the diaphragm. The boundary conditions are:

$$w = dw/dr = 0, N_r = \overline{N_r} \text{ at } \rho = 1,$$



LOCATIONS OF NORMAL FORCES AND BENDING MOMENTS ON SECTION OF DIAPHRAGM .

Figure B13



BOUNDARY CONDITIONS FOR CASES I, II, AND III.

Figure B14

where \overline{N}_r is the load per unit length at $\rho = 1$.

Case II. A uniform pressure P_o is applied to the surface of the diaphragm with the circumference rigidly clamped. The maximum stresses occur at the peak applied pressure of 1000 psi. The boundary conditions are:

$$w = dw/dr = u = 0 \text{ at } \rho = 1,$$

$$P_n = P_o,$$

where u is the displacement of the diaphragm in the radial direction.

Case III. A uniform pressure P_o is applied to the diaphragm surface with the circumference free to expand in the radial direction. Again, the maximum stresses occur when $P_o = 1000$ psi. The boundary conditions are:

$$w = dw/dr = N_r = 0 \text{ at } \rho = 1,$$

$$P_n = P_o,$$

The equations for the desired quantities N_r , N_θ , M_r , M_θ and w for the three cases are given in the following section. These equations are obtained by summing the appropriate homogeneous and particular solutions developed by Wan for the three cases and evaluating the constants subject to specified boundary conditions.

Case I:

$$N_r = \frac{\bar{N}_r}{\rho Be_2} \cdot \left(\frac{bei'(\lambda) \cdot bei'(\lambda\rho)}{ber'(\lambda)} + ber'(\lambda\rho) \right)$$

$$N_\theta = -\frac{\lambda \bar{N}_r}{Be_2} \cdot \left[-\frac{bei'(\lambda) \cdot ber(\lambda\rho)}{ber'(\lambda)} + bei(\lambda\rho) \right. \\ \left. - \frac{1}{\lambda\rho} \cdot \left(-\frac{bei'(\lambda) \cdot bei'(\lambda\rho)}{ber'(\lambda)} - ber'(\lambda\rho) \right) \right]$$

$$M_r = \frac{\bar{N}_r a^2}{R\lambda Be_2} \cdot \left[-\frac{bei'(\lambda) \cdot bei(\lambda\rho)}{ber'(\lambda)} - ber(\lambda\rho) \right. \\ \left. + \frac{(1-\nu)}{\lambda\rho} \cdot \left(-\frac{bei'(\lambda) \cdot ber'(\lambda\rho)}{ber'(\lambda)} + bei'(\lambda\rho) \right) \right]$$

$$M_\theta = \frac{\bar{N}_r a^2}{\lambda R Be_2} \cdot \left[\nu \cdot \left(-\frac{bei'(\lambda) \cdot bei(\lambda\rho)}{ber'(\lambda)} - ber(\lambda\rho) \right) \right. \\ \left. - \frac{(1-\nu)}{\lambda\rho} \cdot \left(-\frac{bei'(\lambda) \cdot ber'(\lambda\rho)}{ber'(\lambda)} + bei'(\lambda\rho) \right) \right]$$

$$w = \left(\frac{\bar{N}_r AR\lambda}{Be_2} \right) \cdot \left(Be_1 - \frac{bei'(\lambda) \cdot ber(\lambda\rho)}{ber'(\lambda)} + bei(\lambda\rho) \right)$$

Case II:

$$N_r = -\frac{P_o R}{2} \cdot \left[1 + \frac{(1-\nu)}{\rho[\lambda Be_1 - (1+\nu)Be_2]} \cdot \left(-\frac{bei'(\lambda) \cdot bei'(\lambda\rho)}{ber'(\lambda)} - ber'(\lambda\rho) \right) \right]$$

$$N_\theta = -\frac{P_o R}{2} \cdot \left[1 + \frac{\lambda(1-\nu)}{[\lambda Be_1 - (1+\nu)Be_2]} \cdot \left[-\frac{bei'(\lambda) \cdot ber(\lambda\rho)}{ber'(\lambda)} + bei(\lambda\rho) \right. \right. \\ \left. \left. - \frac{1}{\lambda\rho} \cdot \left(-\frac{bei'(\lambda) \cdot bei'(\lambda\rho)}{ber'(\lambda)} - ber'(\lambda\rho) \right) \right] \right]$$

$$M_r = \frac{P_o a^2(1-\nu)}{2\lambda[\lambda Be_1 - (1+\nu)Be_2]} \cdot \left[-\frac{bei'(\lambda) \cdot bei(\lambda\rho)}{ber'(\lambda)} - ber(\lambda\rho) \right. \\ \left. + \frac{(1-\nu)}{\lambda\rho} \cdot \left(-\frac{bei'(\lambda) \cdot ber'(\lambda\rho)}{ber'(\lambda)} + bei'(\lambda\rho) \right) \right]$$

$$M_\theta = \frac{P_o a^2(1-\nu)}{2\lambda[\lambda Be_1 - (1+\nu)Be_2]} \cdot \left[\nu \cdot \left(-\frac{bei'(\lambda) \cdot bei(\lambda\rho)}{ber'(\lambda)} - ber(\lambda\rho) \right) \right. \\ \left. - \frac{(1-\nu)}{\lambda\rho} \cdot \left(-\frac{bei'(\lambda) \cdot ber'(\lambda\rho)}{ber'(\lambda)} + bei'(\lambda\rho) \right) \right]$$

$$w = \frac{P_o \lambda R^2(1-\nu)}{2[\lambda Be_1 - (1+\nu)Be_2]} \cdot \left(Be_1 - \frac{bei'(\lambda) \cdot ber(\lambda\rho)}{ber'(\lambda)} + bei(\lambda\rho) \right)$$

Case III:

$$N_r = -\frac{P_o R}{2} \cdot \left[1 + \frac{1}{Be_2 \rho} \cdot \left(-\frac{bei'(\lambda) \cdot bei'(\lambda \rho)}{ber'(\lambda)} - ber'(\lambda \rho) \right) \right]$$

$$N_\theta = -\frac{P_o R}{2} \cdot \left[1 + \frac{\lambda}{Be_2} \cdot \left[-\frac{bei'(\lambda) \cdot ber(\lambda \rho)}{ber'(\lambda)} + bei(\lambda \rho) \right. \right. \\ \left. \left. - \frac{1}{\lambda \rho} \cdot \left(-\frac{bei'(\lambda) \cdot bei'(\lambda \rho)}{ber'(\lambda)} - ber'(\lambda \rho) \right) \right] \right]$$

$$M_r = \frac{P_o a^2}{2\lambda Be_2} \cdot \left[-\frac{bei'(\lambda) \cdot bei(\lambda \rho)}{ber'(\lambda)} - ber(\lambda \rho) \right. \\ \left. + \frac{(1-\nu)}{\lambda \rho} \cdot \left(-\frac{bei'(\lambda) \cdot ber'(\lambda \rho)}{ber'(\lambda)} + bei'(\lambda \rho) \right) \right]$$

$$M_\theta = \frac{P_o a^2}{2\lambda Be_2} \cdot \left[\nu \cdot \left(-\frac{bei'(\lambda) \cdot bei(\lambda \rho)}{ber'(\lambda)} - ber(\lambda \rho) \right) \right. \\ \left. - \frac{(1-\nu)}{\lambda \rho} \cdot \left(-\frac{bei'(\lambda) \cdot ber'(\lambda \rho)}{ber'(\lambda)} + bei'(\lambda \rho) \right) \right]$$

$$w = \frac{P_o AR^2 \lambda}{2Be_2} \cdot \left(Be_1 - \frac{bei'(\lambda) \cdot ber(\lambda \rho)}{ber'(\lambda)} + bei(\lambda \rho) \right)$$

where

\overline{N}_r = load per unit length applied in the radial direction
to the circumference of the diaphragm,

P_o = transverse pressure applied to diaphragm,

$\lambda = \frac{a}{\sqrt{Rh}} [12(1-\nu^2)]^{1/4}$ = a constant for a particular diaphragm,

$Be_1 = \frac{ber'(\lambda)ber(\lambda) - ber(\lambda)bei'(\lambda)}{ber''(\lambda)}$, and

$Be_2 = \frac{[ber'(\lambda)]^2 + [bei'(\lambda)]^2}{ber''(\lambda)}$.

The quantities $ber(\lambda)$, $bei(\lambda)$, $ber'(\lambda)$, $bei'(\lambda)$ are the real and imaginary parts (and their derivatives) of the complex function $J_o(i^{3/2}x)$, where J_o is the Bessel function of the first kind, of order zero:

$$J_o(i^{3/2}x) = ber(x) + i bei(x).$$

The equations for N_r , N_θ , M_r , and M_θ yield answers in terms of loads or bending moments per unit length. The corresponding stresses are determined from the following two equations:

$$\sigma_{rD} = \frac{N_r}{h}, \quad \sigma_{\theta D} = \frac{N_\theta}{h}$$

$$\sigma_{rB} = \frac{6M_r}{h^2}, \quad \sigma_{\theta B} = \frac{6M_\theta}{h^2}$$

where σ_{rD} , $\sigma_{\theta D}$ = direct stresses (D) in the radial (r) and tangential (θ) directions respectively,

σ_{rB} , $\sigma_{\theta B}$ = bending stresses (B) on diaphragm surfaces in the radial and tangential directions.

A positive number for σ_{rD} or $\sigma_{\theta D}$ indicates a tensile stress; a positive number for σ_{rB} or $\sigma_{\theta B}$ indicates that the concave surface is in tension

and the convex surface is in compression.

The resulting principal stresses in the radial and tangential directions on the two surfaces are the algebraic sum of the direct and bending stresses.

On the convex surface:

$$\sigma_{r_{\text{convex}}} = \sigma_{rD} - \sigma_{rB}$$

$$\sigma_{\theta_{\text{convex}}} = \sigma_{\theta D} - \sigma_{\theta B}$$

On the concave surface:

$$\sigma_{r_{\text{concave}}} = \sigma_{rD} + \sigma_{rB}$$

$$\sigma_{\theta_{\text{concave}}} = \sigma_{\theta D} + \sigma_{\theta B}$$

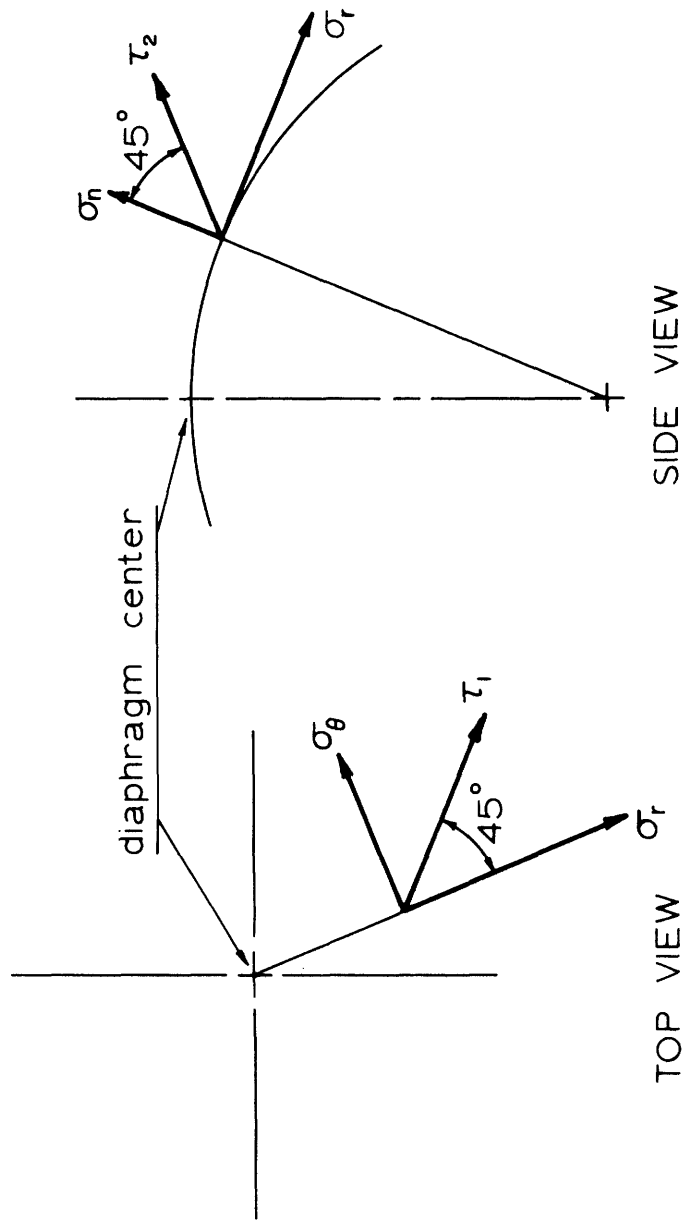
These four equations give the major stresses at any point on the surfaces of the diaphragm for the three loading situations. Knowing these principle stresses the shear stresses which act in directions tangential to the surface can be computed from

$$\tau_1 = \frac{\sigma_r - \sigma_\theta}{2} .$$

In general, however, the principal stresses either have the same sign or are small enough when of opposite sign to insure that this shear stress is always less than one-half of the peak normal stress. The peak shear stresses occur on planes having normals 45 degrees from the normals to the diaphragm surface. In this case the shear stress is

$$\tau_2 = \frac{\sigma_r - \sigma_n}{2} \quad \text{where } \sigma_n \text{ is the transverse pressure.}$$

Since $\sigma_n \ll \sigma_r$ the peak shear stress is about 1/2 the peak radial stress. These shear stresses are shown in Figure B15.



LOCATIONS OF PRINCIPLE SHEAR STRESSES IN DIAPHRAGM.

Figure B15

Given the dimensions of the diaphragm and the mechanical characteristics of Vitallium, it is possible to compute the principal stresses in the surfaces of the diaphragm for the three cases, given the loads applied to the diaphragm. For Cases II and III, the applied pressure is 1000 psi. For Case I, where the diaphragm is subjected to an edge load \overline{N}_r , the numerical value for \overline{N}_r , when 1000 psi is applied everywhere on the hemisphere except on the diaphragm, is not immediately known.

As mentioned previously, the numerical value for \overline{N}_r was found experimentally by a trial-and-error procedure by loading all of the hemisphere except the diaphragm to 1000 psi and measuring the outward deflection of the diaphragm. The edge load \overline{N}_r required to produce this deflection was then calculated from the appropriate equation developed for Case I. The value of \overline{N}_r for use in the Case I equations was found to be 65.6 lb/in.

A tabulation of the pertinent stresses and deflections for the three cases is presented in Table 1. Also included is a tabulation of the combined stresses in the diaphragm when Cases I and III occur simultaneously, i.e., the diaphragm is subjected to edge loads F as well as transverse pressures.

Numerical Values

The numerical values used to compute the stresses as given by the above equations are listed here.

Diaphragm dimensions:

a = diaphragm radius = 0.0781 in.

R = radius of curvature = 0.938 in.

h = diaphragm thickness = 0.0105 in.

Material properties of Vitallium:

$$E = \text{modulus of elasticity} = 3.6 \times 10^7 \text{ lb/in.}^2$$

$$\nu = \text{Poisson's ratio} = 0.3$$

$$\begin{aligned} \sigma_e &= \text{endurance limit, reversed bending at } 10^8 \text{ cycles,} \\ &= 40,000 \text{ psi} \end{aligned}$$

Constants in stress and deflection equations:

$$\lambda = 1.430$$

$$A = 3.18 \times 10^{-6} \text{ in./lb}$$

$$D = 3.18 \text{ in. lb}$$

$$P_o = 1000 \text{ psi}$$

$$\frac{N}{r} = 65.6 \text{ lb/in.}$$

$$\text{ber}(\lambda) = 0.9348$$

$$\text{bei}(\lambda) = 0.5075$$

$$\text{ber}'(\lambda) = -0.1821$$

$$\text{bei}'(\lambda) = 0.6994$$

$$Be_1 = -4.10$$

$$Be_2 = -2.87$$

Flat Diaphragm Equations

For comparison purposes the radial and tangential stresses for a flat diaphragm of the same diameter and thickness as the spherical diaphragm were computed. The following equations from Roark (Ref. 18) were used to compute σ_r , σ_θ , and w for the flat diaphragm. Note that for a flat diaphragm only bending stresses are present, so that the stresses on opposite sides are equal in magnitude.

$$\sigma_r = \frac{3P_o a^2}{8h^2} [(3+\nu)\rho^2 - (1+\nu)]$$

$$\sigma_{\theta} = \frac{3P_o a^2}{8h^2} [(1+3\nu)\rho^2 - (1-\nu)]$$

$$w = \frac{3P_o a^4 (1-\nu^2)}{16Eh^3} (1-\rho^2)^2$$

The constants are the same as in the equations for the spherical diaphragm.

Table 2 lists σ_r , σ_{θ} and w for the flat diaphragm as a function of ρ .

Worst-Case Stress Conditions

The largest stresses occur on the diaphragm surfaces at the center and at the circumference. In addition, the stresses at the diaphragm circumference must be increased by the appropriate stress concentration factor. This stress concentration factor was determined to be 1.30 (Ref. 18).

The range of peak stresses in the diaphragm for Cases I, II and III, and the situation with Cases I and III combined, are tabulated in Table 3. The worst-case (maximum) stress ranges for the four peak stress locations on the diaphragm are also listed. For Cases II and III, the actual stresses in the diaphragm lie between the values given for these two cases. Since the actual values are unknown, either Case II or Case III was used to compute the maximum stress range, depending on which case gave the larger figure. These worst-case stress ranges and their location in the Goodman diagram are shown in Figure B12.

Stresses in Diaphragms of Different Radius of Curvature

Pressure transducer diaphragms will be constructed in prostheses

having sphere diameters of $1 \frac{3}{4}$ and $1 \frac{13}{16}$ in. in addition to the $1 \frac{7}{8}$ in. size for which the values of stress were computed. The influence of the change in R, the radius of curvature, on the diaphragm stresses for these three ball sizes is negligible, so that the numerical values of stress are essentially the same for all three sizes.

TABLE 1 - Stresses in spherical diaphragm.

Case I: $P_n = 0$, $F = F_{\max}$; $w = dw/dr = 0$ at $\rho = 1$.

	ρ	0	.1	.2	.3	.4	.5	.6	.7	.8	.9	1.0
N_r , lb/in, x 10		-6.28	-6.29	-6.30	-6.33	-6.35	-6.38	-6.41	-6.45	-6.50	-6.53	-6.56
N_θ , lb/in, x 10		-6.30	-6.30	-6.34	-6.40	-6.48	-6.56	-6.65	-6.74	-6.81	-6.85	-6.86
M_r , lb, x 10 ⁻²		-6.76	-6.60	-6.09	-5.24	-4.05	-2.51	-0.61	1.63	4.24	7.20	10.6
M_θ , lb, x 10 ⁻²		-6.76	-6.66	-6.38	-5.89	-5.20	-4.33	-3.24	-1.95	-0.45	1.25	3.18
σ_{rD} , psi, x 10 ³		-5.98	-5.99	-6.00	-6.03	-6.05	-6.08	-6.10	-6.14	-6.19	-6.21	-6.25
$\sigma_{\theta D}$, psi, x 10 ³		-6.00	-6.00	-6.04	-6.09	-6.16	-6.25	-6.33	-6.41	-6.49	-6.53	-6.54
σ_{rB} , psi, x 10 ³		-3.68	-3.59	-3.31	-2.85	-2.20	-1.36	-0.33	0.89	2.30	3.91	5.74
$\sigma_{\theta B}$, psi, x 10 ³		-3.68	-3.63	-3.46	-3.20	-2.83	-2.35	-1.76	-1.06	-0.25	0.68	1.73
σ_r convex, psi, x 10 ³		-2.30	-2.40	-2.69	-3.18	-3.85	-4.71	-5.78	-7.03	-8.49	-10.1	-12.0
σ_θ convex, psi, x 10 ³		-2.33	-2.38	-2.58	-2.89	-3.34	-3.90	-4.56	-5.35	-6.24	-7.20	-8.26
σ_r concave, psi, x 10 ³		-9.65	-9.58	-9.31	-8.88	-8.25	-7.44	-6.43	-5.25	-3.89	-2.30	-0.51
σ_θ concave, psi, x 10 ³		-9.68	-9.63	-9.50	-9.29	-8.99	-8.60	-8.09	-7.48	-6.74	-5.85	-4.81
w , inches, x 10 ⁻⁶		-20.9	-20.5	-19.3	-17.3	-14.8	-11.8	-8.62	-5.45	-2.77	-0.73	0

TABLE 1 (continued)

Case II: $P_n = P_o$, $F = 0$; $w = dw/dr = u = 0$ at $\rho = 1$.

	ρ	0	.1	.2	.3	.4	.5	.6	.7	.8	.9	1.0
N_r , lb/in, x 10		-4.67	-4.63	-4.54	-4.39	-4.23	-4.01	-3.75	-3.50	-3.23	-2.98	-2.78
N_θ , lb/in, x 10		-4.80	-4.74	-4.50	-4.10	-3.60	-3.01	-2.42	-1.80	-1.34	-1.06	-1.04
M_r , lb, x 10 ⁻¹		4.55	4.43	4.09	3.52	2.79	1.69	0.42	-1.09	-2.84	-4.84	-7.09
M_θ , lb, x 10 ⁻¹		4.54	4.48	4.28	3.95	3.49	2.90	2.17	1.31	0.30	-0.84	-2.13
σ_{rD} , psi, x 10 ³		-4.44	-4.41	-4.32	-4.18	-4.03	-3.82	-3.57	-3.33	-3.07	-2.84	-2.65
$\sigma_{\theta D}$, psi, x 10 ³		-4.57	-4.51	-4.28	-3.90	-3.43	-2.87	-2.30	-1.71	-1.28	-1.01	-0.99
σ_{rB} , psi, x 10 ³		24.8	24.1	22.2	19.1	15.2	9.20	2.30	-5.90	-15.4	-26.3	-38.6
$\sigma_{\theta B}$, psi, x 10 ³		24.7	24.4	23.3	21.5	19.0	15.8	11.8	7.10	1.60	-4.60	-11.6
σ_r convex, psi, x 10 ³		-29.2	-28.5	-26.5	-23.3	-19.2	-13.0	-5.90	2.60	12.3	23.5	35.9
σ_θ convex, psi, x 10 ³		-29.3	-28.9	-27.6	-25.4	-22.4	-18.7	-14.1	-8.80	-2.90	3.60	10.6
σ_r concave, psi, x 10 ³		20.4	19.7	17.9	14.9	11.2	5.40	-1.30	-9.20	-18.5	-29.1	-41.3
σ_θ concave, psi, x 10 ³		20.1	19.9	19.0	17.6	15.6	12.9	9.50	5.40	0.30	-5.60	-12.6
w , inches, x 10 ⁻⁶		140	138	129	117	99	79	57	37	18	5	0

TABLE 1 (continued)

Case III: $P_n = P_o$, $F = 0$; $w = dw/dr = N_r = 0$ at $\rho = 1$.

ρ	0	.1	.2	.3	.4	.5	.6	.7	.8	.9	1.0
N_r , lb/in, x 10	-1.97	-1.92	-1.82	-1.67	-1.50	-1.27	-0.99	-0.73	-0.43	-0.17	0.00
N_θ , lb/in, x 10	-2.01	-1.94	-1.68	-1.26	-0.73	-0.09	0.53	1.19	1.68	1.98	2.01
M_r , lb, x 10 ⁻¹	4.84	4.72	4.36	3.75	2.90	1.80	0.45	-1.16	-3.03	-5.16	-7.55
M_θ , lb, x 10 ⁻¹	4.83	4.76	4.56	4.21	3.72	3.09	2.31	1.39	0.32	-0.90	-2.26
σ_{rD} , psi, x 10 ³	-1.88	-1.83	-1.74	-1.59	-1.42	-1.21	-0.94	-0.69	-0.41	-0.16	0.00
$\sigma_{\theta D}$, psi, x 10 ³	-1.91	-1.85	-1.60	-1.20	-0.69	-0.08	0.50	1.13	1.60	1.88	1.91
σ_{rB} , psi, x 10 ³	26.3	25.7	23.7	20.4	15.8	9.80	2.40	-6.30	-16.5	-28.1	-41.1
$\sigma_{\theta B}$, psi, x 10 ³	26.3	25.9	24.8	22.9	20.2	16.8	12.6	7.60	1.70	-4.90	-12.3
σ_r convex, psi, x 10 ³	-28.2	-27.5	25.4	-22.0	-17.2	-11.0	-3.30	5.60	16.1	27.9	41.1
σ_θ convex, psi, x 10 ³	-28.2	-27.8	-26.4	-24.1	-20.9	-16.9	-12.1	-6.50	-0.10	6.80	14.2
σ_r concave, psi, x 10 ³	24.4	23.9	22.0	18.8	14.4	8.60	1.50	-7.00	-16.9	-28.3	-41.1
σ_θ concave, psi, x 10 ³	24.4	24.0	23.2	21.7	19.5	16.7	13.1	8.70	3.30	-3.00	-10.4
w , inches, x 10 ⁻⁶	149	147	137	124	106	84	62	39	20	5	0

TABLE 1 (continued)

Algebraic summation of stresses for Cases I and III.

	0	.1	.2	.3	.4	.5	.6	.7	.8	.9	1.0
σ_r convex, psi, x 10^3	-30.5	-29.9	-28.1	-25.2	-21.1	-5.7	-9.10	-1.40	7.60	17.8	29.1
σ_θ convex, psi, x 10^3	-30.5	-30.2	-29.0	-27.0	-24.2	-20.8	-16.7	-11.9	-6.30	-0.40	5.90
σ_r concave, psi, x 10^3	14.7	14.3	12.7	9.90	6.10	1.20	-4.90	-12.3	-20.8	-30.6	-41.6
σ_θ concave, psi, x 10^3	14.7	14.4	13.7	12.4	10.5	8.10	5.00	1.20	-3.40	-8.90	-15.2

TABLE 2

Stresses in flat diaphragm, $P_n = P_o$.

ρ	0	.1	.2	.3	.4	.5	.6	.7	.8	.9	1.0
σ_r , psi, $\times 10^3$	-26.9	-26.2	-24.2	-20.8	-16.0	-9.80	-2.30	6.60	16.8	28.4	41.4
σ_θ , psi, $\times 10^3$	-26.9	-26.6	25.4	-23.3	-20.6	-17.1	-12.8	-7.60	-1.70	5.00	12.6
w , inches, $\times 10^{-6}$	152	149	140	126	108	86	62	40	20	6	0

TABLE 3

Comparison of worst-case radial stress ranges. Units are psi x 10³.

	Convex Surface		Concave Surface	
	$\rho = 0$	$\rho = 1$	$\rho = 0$	$\rho = 1$
Case I	-2.30	-12.0	-9.65	-0.51
Case II	-29.2	35.9	20.4	-41.3
Case III	-28.2	41.1	24.4	-41.1
Case I + Case III	-30.5	29.1	14.7	-41.6
Maximum Stress Range	0 to -30.5	-12.0 to 41.1	-9.65 to 24.4	0 to -41.6
σ_{mean}	-15.25	14.55	7.35	-20.8
$\sigma_{\text{alternating}}$	15.25	26.55	17.05	20.8
$\sigma_{\text{alternating}} \times 1.3^*$		34.52		27.04

*Stress concentration factor, applied to alternating component of stress at $\rho = 1$.

APPENDIX C

DIAPHRAGM FATIGUE TEST

Mechanical failure of the transducer diaphragms can have serious consequences for the person in whom the prosthesis is implanted. A crack in a diaphragm, no matter how it is initiated, will grow with time under repeated cyclic loading if the stress produced by such loading exceeds the endurance limit of the diaphragm material. If a crack occurs on the outer surface of the diaphragm the cartilage in the acetabulum could be scratched or abraded by the edges of the crack. A crack extending all the way through the diaphragm presents the possibility of contaminating the hip socket with biologically incompatible materials present inside the prosthesis. In addition, the presence of a crack or other diaphragm failure probably could not be detected before significant damage had been done to the hip socket. It is, therefore, imperative that all reasonable precautions be taken to preclude the possibility of a diaphragm failure.

The diaphragm has been designed to satisfy a fatigue life criterion. This means that theoretically the diaphragm can withstand repeated cycling between 0 and 1000 psi indefinitely without initiating a crack in the diaphragm. To further reinforce confidence in the theoretical stress analysis an experimental fatigue test was conducted on ten identical diaphragms.

Fatigue Test Specifications

The fatigue test was designed to simulate the diaphragm design criteria. In addition, to more closely approximate the physiological

environment of the hip joint, the diaphragms were continuously exposed to a 0.9 percent saline solution during the test. Vitallium in general appears to be unaffected by saline solutions or other fluids in the body, but there are no data on the effects of saline solutions on the endurance limit of Vitallium. This area of uncertainty was removed by testing the diaphragms in a saline solution.

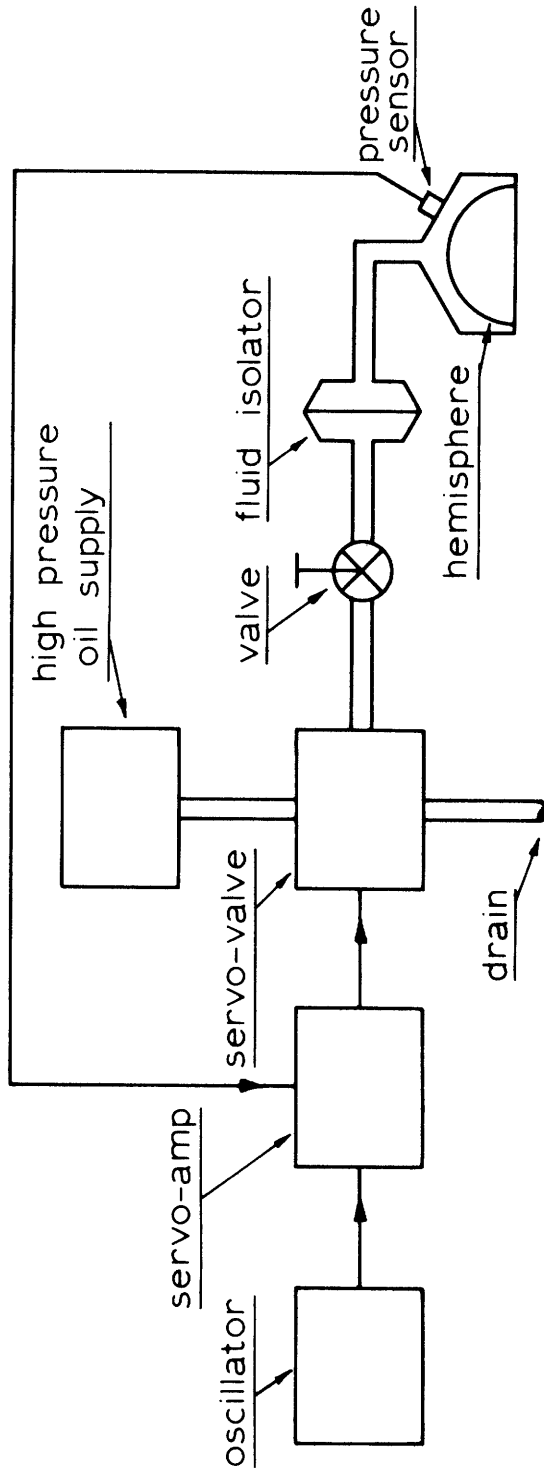
Experimental Apparatus

The ten diaphragms which were tested were uniformly distributed over the surface of a 1 7/8 in. diameter Vitallium hemisphere. All ten diaphragms were machined to the dimensions specified by the stress analysis.

A diagram of the test set up is shown in Figure C1. The hemisphere was mounted in a stainless steel pressure chamber which was filled with the saline solution. The pressure in the chamber was varied by means of a hydraulic servo-system. A flexible rubber diaphragm isolated the saline solution in the test chamber from the oil in the hydraulic system.

The pressure in the test chamber was controlled electrically by means of a servo-valve and servo-amplifier. The servo-valve was switched between a high pressure supply line and an atmospheric pressure drain line. The pressure cycle was controlled by a sinusoidal oscillator, and pressure feedback was employed to produce a nearly sinusoidal pressure variation.

The mass of the fluid in the tubing between the servo-valve and the test chamber and the small but inevitable volume of air trapped in the system were such that the system exhibited significant dynamic behavior at the pressure cycling rate. A manually adjusted needle



FATIGUE TEST APPARATUS .

Figure C1

valve was used to vary the damping in the system to smooth out the pressure variations.

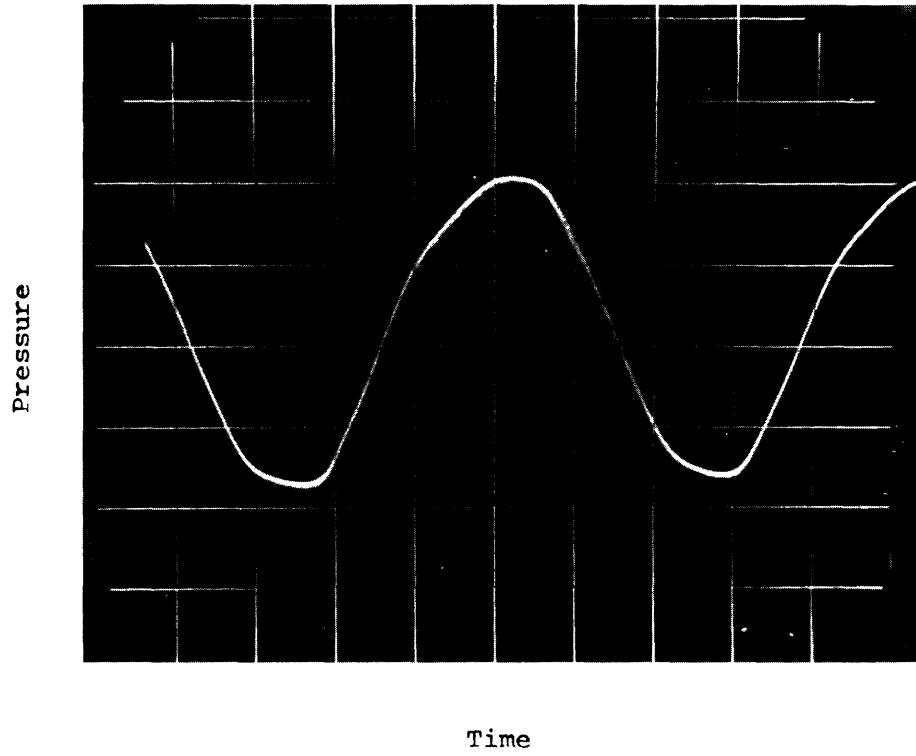
The cycling rate used throughout the fatigue test was 47 cycles per second. At this frequency the system seemed to operate most satisfactorily, and the pressure in the test chamber could be made to vary smoothly.

The pressure in the test chamber was monitored by one of the pressure transducers designed for the hip prosthesis. One of the ten diaphragms in the hemisphere served as the pressure sensitive element in this transducer. The fatigue test thus served to help evaluate the performance of the pressure transducer in addition to checking the reliability of the diaphragms. A typical pressure waveform for one cycle as measured by this transducer is shown in Figure C2. The pressure transducer was calibrated periodically throughout the test to insure the accuracy of the measured pressures.

Test Results

The ten diaphragms were subjected to a total of 43 million cycles. The pressure range during the first 10 million cycles was 0 to 1000 psi; the remaining 33 million cycles were from 0 to 1100 psi. The pressure range was increased at 10 million cycles to more closely approximate the stress range in the diaphragm resulting from worst-case conditions. The fatigue test could not simulate the stress reversal in the diaphragm that occurs when an edge load is applied to the diaphragm in the absence of a direct normal load. The same effective stress range as far as the fatigue test was concerned was produced by increasing the pressure range to 0 to 1100 psi.

The outer surfaces of the diaphragms were visually inspected



Fatigue Test Pressure Waveform

Figure C2

periodically throughout the test for evidence of any form of failure. The diaphragm surfaces were also subjected to a dye penetrant test to determine the presence of surface cracks invisible to the naked eye. This test consists of spraying the surface to be tested with a bright red dye that penetrates any crack in the surface. The excess dye is wiped off, and a fine, white powder is applied to the surface. If a crack is present, the red dye in the crack will be drawn out by the white coating, and the presence of the crack will be indicated by the reddish stain in the coating.

At the end of the 43 million cycles there was no evidence of any failure of any of the diaphragms. The surface of the hemisphere appeared to be unchanged. In addition, the one complete pressure transducer in the hemisphere showed no change in sensitivity throughout the test. Any change in the stiffness of the transducer diaphragm due to internal cracks would have caused a change in sensitivity. Thus, in this one instrumented diaphragm, there was no evidence of internal failure.

Test Conclusions

The results of this fatigue test must be interpreted with some care. The probability of a diaphragm failure cannot be predicted from this one test on ten diaphragms. A series of tests on a large number of diaphragms would be necessary to determine the probability of failure at a given number of cycles. The results of this test tend to confirm the theoretical stress analysis; confidence in the performance of the diaphragms is increased. These results do not indicate that no diaphragm will ever fail when subjected to the same fatigue test as these ten diaphragms, but they do indicate that a failure is very unlikely.

APPENDIX D

PRESSURE TRANSDUCER DESIGN AND ASSEMBLY

Mechanical-to-Electrical Conversion Element

The pressure transducer contains two basic elements--a diaphragm, which produces a mechanical motion proportional to the applied pressure, and a motion sensing element that causes some electrically measurable parameter to change in response to the diaphragm motion. The transducer diaphragm has been discussed in Appendix B. The design details of the mechanical-to-electrical sensing element are presented in the following paragraphs.

Two of the dimensional characteristics of the diaphragm that respond to pressure changes and that are reasonably easy to measure are the surface strain due to bending (measured by strain gages bonded to the inner surface of the diaphragm) and the transverse deflection of the center of the diaphragm (measured by a displacement sensing device). Both of these methods work well in transducers in which the circumference of the diaphragm is rigidly clamped. If the diaphragm circumference is not rigidly clamped, as is the case in the hip prosthesis transducer, measuring the center deflection of the diaphragm gives a more accurate pressure measurement than that obtained by measuring its surface strain.

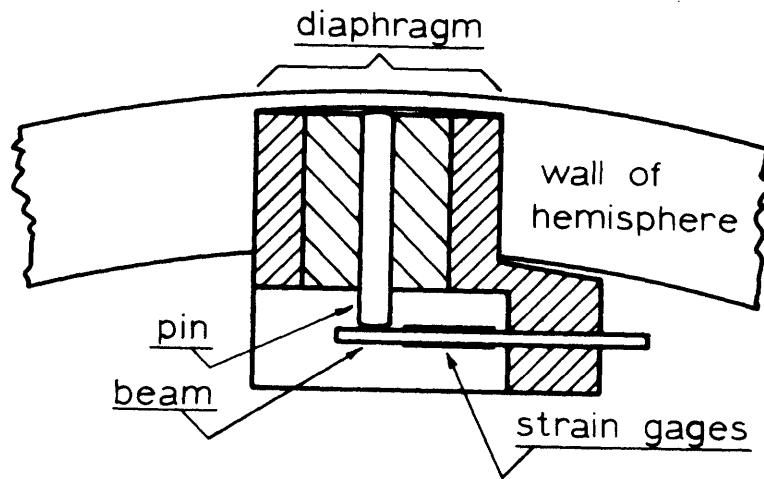
In a semi-rigidly clamped diaphragm, surface strain is caused not only by bending of the diaphragm due to transverse pressure applied to the diaphragm but also by stresses applied to the circumference of the diaphragm caused by loads applied to the diaphragm supports. The sensitivity of the transverse deflection of the center of the diaphragm to edge loads, however, is a function of the radius

of curvature of the diaphragm. In the case of a flat diaphragm, the deflection of its center is essentially zero for radially applied edge loads, up to the stress level where the diaphragm becomes unstable and buckles. The surface strain, though, responds directly to the applied edge loads.

The diaphragms in the hip prosthesis are shallow spheres, so that an edge load does cause some motion of the diaphragm center. However, measuring the center deflection is decidedly more accurate than measuring surface strain. The maximum error caused by worst-case loading conditions (uniform pressure over the entire surface of the hemisphere) is approximately 37 percent for the surface strain method, while the error under similar conditions for the center deflection method is 12 percent. Since worst-case loading conditions are expected to occur rarely, if at all, the error under normal conditions will be significantly less than these figures.

Several practical considerations also make the center deflection method desirable. The small size of the diaphragm, together with its spherical surface, make mounting strain gages directly on its concave surface a difficult procedure. In addition, the strain gage bridge can only be balanced electrically by the addition of an external resistor. The center-deflection method, which also employs a strain gage bridge as the mechanical-to-electrical conversion element, offers the alternative of balancing the bridge mechanically, eliminating the balancing resistor. This feature simplifies somewhat the physical lay-out of the electrical components in the telemetry circuitry.

A cross-sectional view of the complete pressure transducer is shown in Figure D1. The motion of the center of the diaphragm is



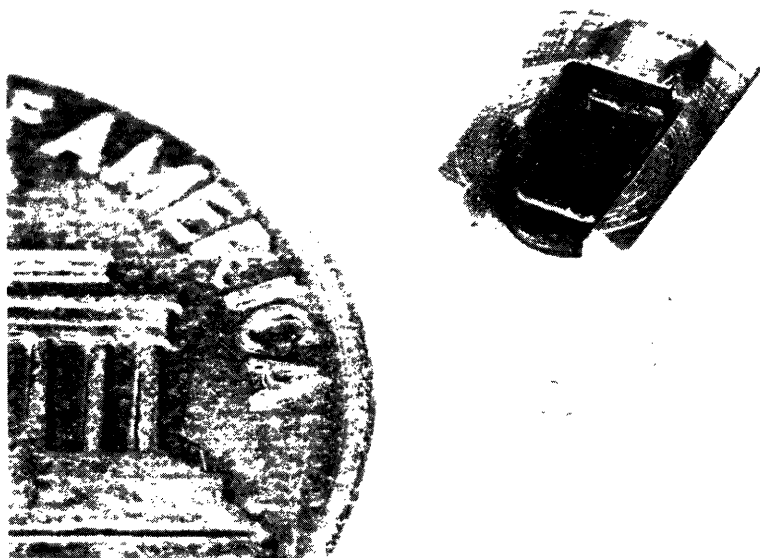
CROSS SECTION OF TRANSDUCER .

Figure D1

coupled to the end of a cantilever beam by a pin that moves freely in a Delrin[®] bushing. The cantilever beam is a single silicon crystal that has four semiconductor strain gages diffused into its surfaces, two gages on the top side and two on the bottom. The gages are wired in a four-active-arm bridge configuration that gives maximum bridge sensitivity and good temperature compensation. The temperature compensation is enhanced by the close proximity of the gages to each other.

The cantilever beam is rigidly mounted in a beam holder which also contains the bushing for the sliding pin. The cantilever beam holder and bushing are assembled as a unit, and this assembly, together with a sliding pin, is then mounted in the wall of the hemisphere under a diaphragm. Figures D2 and D3 show the displacement sensing assembly before and after mounting. During mounting, the cantilever beam is preloaded by a specific amount to insure that the sliding pin will remain in contact with both the diaphragm and the beam. The mass of the pin and beam and the beam preload are such that the pin will remain in contact with the diaphragm for accelerations in excess of 200 g's.

The maximum frequency at which the transducer is useful is limited by the combined mass of the sliding pin and the cantilever beam and the spring constant of the beam. The worst-case condition occurs when the diaphragm and beam have been maximally deflected and the beam must accelerate the pin to follow the diaphragm as it returns to a zero deflection position. The system is a simple spring/mass combination whose resonant frequency is $\omega_n = \sqrt{\frac{k}{m}}$, where k is the spring constant of the beam, and m is the mass of the pin plus a



Displacement Sensing Element Before Mounting
Figure D2



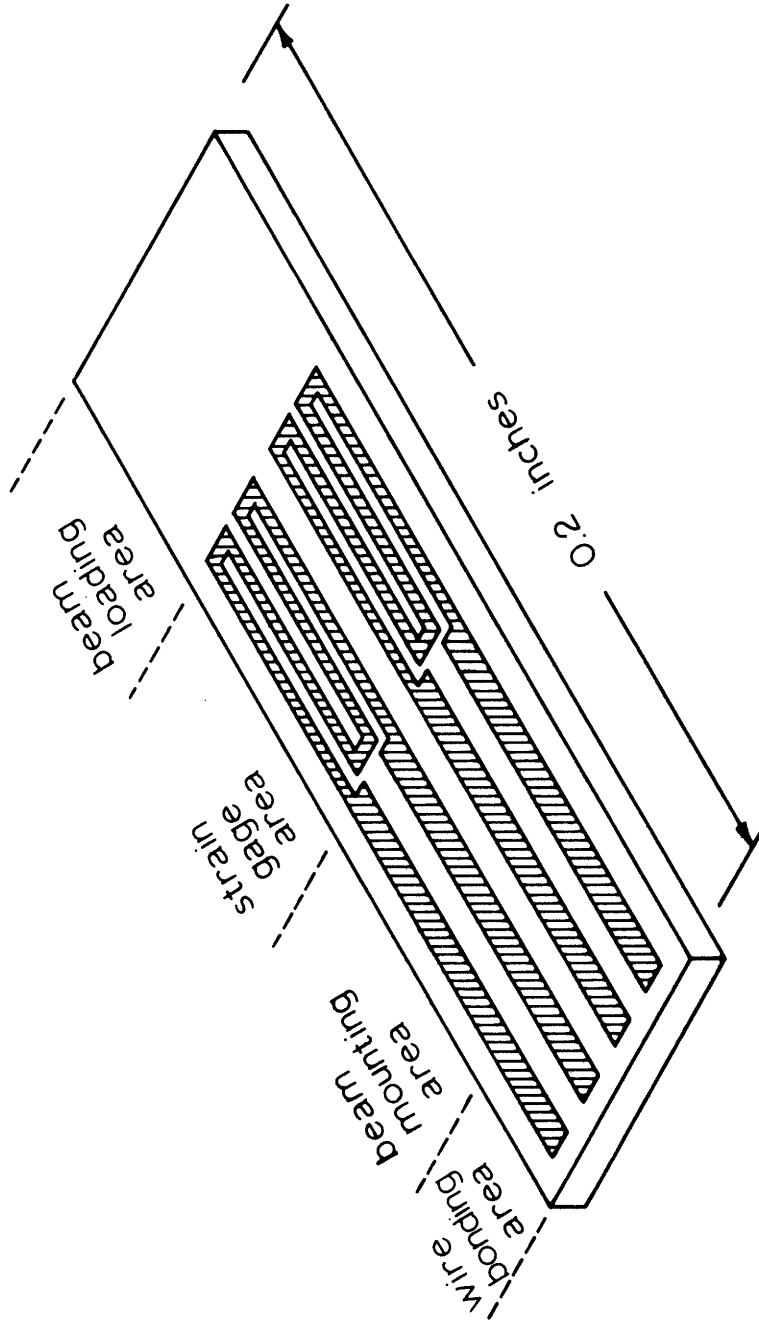
Displacement Sensing Element Mounted in Hemisphere
Figure D3

certain percentage of the mass of the beam. The effective mass that a cantilever beam contributes to a spring/mass system is approximately one fourth of the total mass of the beam for systems in which the beam mass is small in comparison to the mass attached to its end. For the hip prosthesis transducer the resonant frequency is approximately 12 kHz, which is well beyond any expected frequency component in the pressure variations. The deflection of the center of the diaphragm at a peak pressure of 1000 psi is 150 μ in. This deflection should have no effect on the opposing cartilage surface.

The radial clearance between the sliding pin and the plastic bushing is sufficient to allow a free sliding fit. The force applied to the diaphragm by the pin under all conditions is several orders of magnitude smaller than the forces acting on the diaphragm due to external pressure. For all practical purposes, the diaphragm responds only to external pressure. The diaphragm easily overcomes the frictional force developed between the pin and its bushing and the spring force of the beam as it moves inward. As the diaphragm starts to return to the zero-deflection position the force between the pin and diaphragm tends to decrease. This action reduces the tendency of the pin to "cock" or bind in the plastic bushing, a major source of frictional force acting on the pin. As a result, the force exerted on the pin by the deflected beam is sufficient to overcome the smaller frictional forces and maintain the pin in contact with the diaphragm.

Strain Gage Bridge

A drawing of one side of the cantilever beam is shown in Figure D4. The semiconductor strain sensitive elements are connected by metal bands deposited on the beam surface to wire leads attached to the end



PRESSURE TRANSDUCER CANTILEVER BEAM

Figure D4

of the beam that extends beyond the mounting region. The opposite side of the beam is identical. The beam must be insulated from the beam holder to prevent shorting of these metal bands.

As the beam bends, the strain gages on one side are extended while the pair on the opposite side are compressed. The surface strain of the beam varies linearly from the clamped end to the point of loading. The change in resistance of the gages is the same as if the gages were subjected to a uniform strain equal to the average strain over the length of the gage. The four gages are wired in a four-active-arm bridge configuration by short jumper wires at the exposed end of the beam.

The gage factor of the semiconductor strain gages is about 60. For a four-active-arm bridge the output voltage is given by

$$V_o = V_i \cdot GF \cdot \epsilon_{avg}$$

where V_i = bridge excitation voltage,
GF = gage factor, and

ϵ_{avg} = average strain seen by the individual gages.

The surface strain of the beam is given by

$$\epsilon = \frac{3y_e xc}{l^3}$$

where ϵ = surface strain at a distance x from free end of beam,
 y_e = deflection of end of beam,
 x = distance from free end of beam,
 c = one-half the thickness of the beam (0.0035 in.), and
 l = length of beam from clamped end to point where
deflection is y_e (0.085 in.).

The effective strain seen by the strain gage is one-half of the surface strain developed at the clamped end of the beam (the strain

gage is equidistant from the clamped end and the free end). For a deflection y_e of 150 μ in. due to 1000 psi on the diaphragm, the strain at the clamped end of the beam is 218 microstrain. The average strain is 109 microstrain. The theoretical output voltage for 1000 psi on the diaphragm with 6 V input to the bridge is 39.6 mV. This figure agrees well with the results obtained experimentally.

The transducer sensitivity is given by the output voltage for 1 V excitation and 1 psi applied pressure and is 6.6 μ V/V/psi. Because of the small deflection of the diaphragm and cantilever beam this sensitivity is constant over the design operating range of the transducer (0 to 1000 psi).

Pressure Transducer Assembly Procedure

The pressure transducer is assembled in two steps--the cantilever beam is first glued in place in the beam holder, and the beam holder assembly is then mounted in the hemisphere over a diaphragm. This procedure is complicated somewhat by the fact that the inherent non-zero outputs of the pressure transducers and the telemetry system for zero input pressure must be balanced out by varying the preloads on the cantilever beams. The non-zero output for zero input is due to imperfect matching of the resistances of the strain gages in the pressure transducers and to mismatched components in the telemetry system.

The allowable range of beam preloads is relatively large. The maximum preload is limited by the maximum allowable stress in the cantilever beam, and the minimum preload is that load necessary to insure that the sliding pin remains in contact with both the diaphragm

and the beam under worst-case conditions. The range of preloads required to balance out the zero-offset of the strain gages and telemetry components is well within the maximum preload limit of the beams.

Basically, the preloading procedure is as follows. From measurements made on each channel of the telemetry unit, the input voltage required on each channel to produce a zero output voltage is known. The cantilever beam preload is then adjusted to give this voltage on the output of the strain gage bridge. However, the required bridge output voltage may be obtainable only for a negative preload (placing the sliding pin in tension)--an impossible condition. This situation is avoided by mounting the cantilever beam in the beam holder in one of the two possible configurations; the beam can be mounted in the beam holder with one side or the other in contact with the sliding pin. The correct mounting configuration is that in which the beam is bent by preloading in the direction that causes the output voltage to pass through zero.

An example may help to explain this requirement. Assume from previous measurements that the transducer bridge output voltage required to produce a zero voltage signal at the output of a particular telemetry channel is +4 mV. Suppose that the zero preload bridge output voltage of a particular transducer is +5 mV and that the output voltage increases with increasing preload. It is impossible to produce the desired bridge output voltage with this particular transducer assembly. Switching either the bridge input polarity or the output polarity will change the sign of the output voltage to -5 mV, but increasing preloads will merely cause the output to become more negative.

If the cantilever beam in this pressure transducer had been

mounted with the other side of the beam in contact with the sliding pin the desired output voltage could have been obtained. In this case (the correct beam mounting configuration) the bridge output voltage would still be +5 mV for zero preload, but now increasing preloads would cause the bridge output to decrease, pass through zero, and become negative. The desired output voltage of +4 mV is readily obtained. In fact, +4 mV can be obtained for two different preloads if the bridge polarity is adjustable.

The correct preload and bridge polarity is determined by an additional requirement: the bridge output voltages must all become more positive (or more negative) with increasing pressure. The choice of positive going or negative going outputs is determined by the polarity of the synchronizing pulse in the telemetry circuitry.

Suppose that the bridge output must be positive going with increasing pressure. In the above example this requirement is met by simply reversing either the bridge input or output polarity (assuming correct beam mounting configuration). The bridge output voltage would then be -5 mV for zero preload and would become more positive with increasing preload (and increasing pressure). The correct output voltage is achieved by preloading the beam to the point that the output is +4 mV.

The correct beam mounting configuration is determined prior to mounting the beam by measuring the polarity of the bridge output for a specified bridge wiring convention.

Not all telemetry channel zero offsets can be balanced out by a particular pressure transducer. In the above example the range of voltages that the bridge could match is -5 mV to some positive voltage

limited by the maximum allowable preload. Any voltage more negative than -5 mV is not obtainable with this particular transducer bridge. Cantilever beam assemblies must be matched to specific channels to insure that the ranges of bridge output voltages cover the required voltages.

The process of setting the correct preload on the cantilever beam and gluing the cantilever beam assembly in place in the hemisphere is fairly straightforward. The mounting surfaces of the beam holder are coated with a thin layer of epoxy and the assembly is then slipped into the hole over a diaphragm. The desired beam preload is obtained by adjusting the position of the beam holder relative to the diaphragm. This is accomplished in a special assembly fixture that has a micrometer translator capable of accurately positioning the beam holder to within a few millionths of an inch. The point at which the correct preload is achieved is determined by monitoring the bridge output voltage.

This preloading procedure is performed in an oven at 100° F so that the beam will be correctly preloaded when it is operating at or near body temperature.

APPENDIX E

TELEMETRY SYSTEM OPERATION, FABRICATION AND CALIBRATION

Circuit Operation

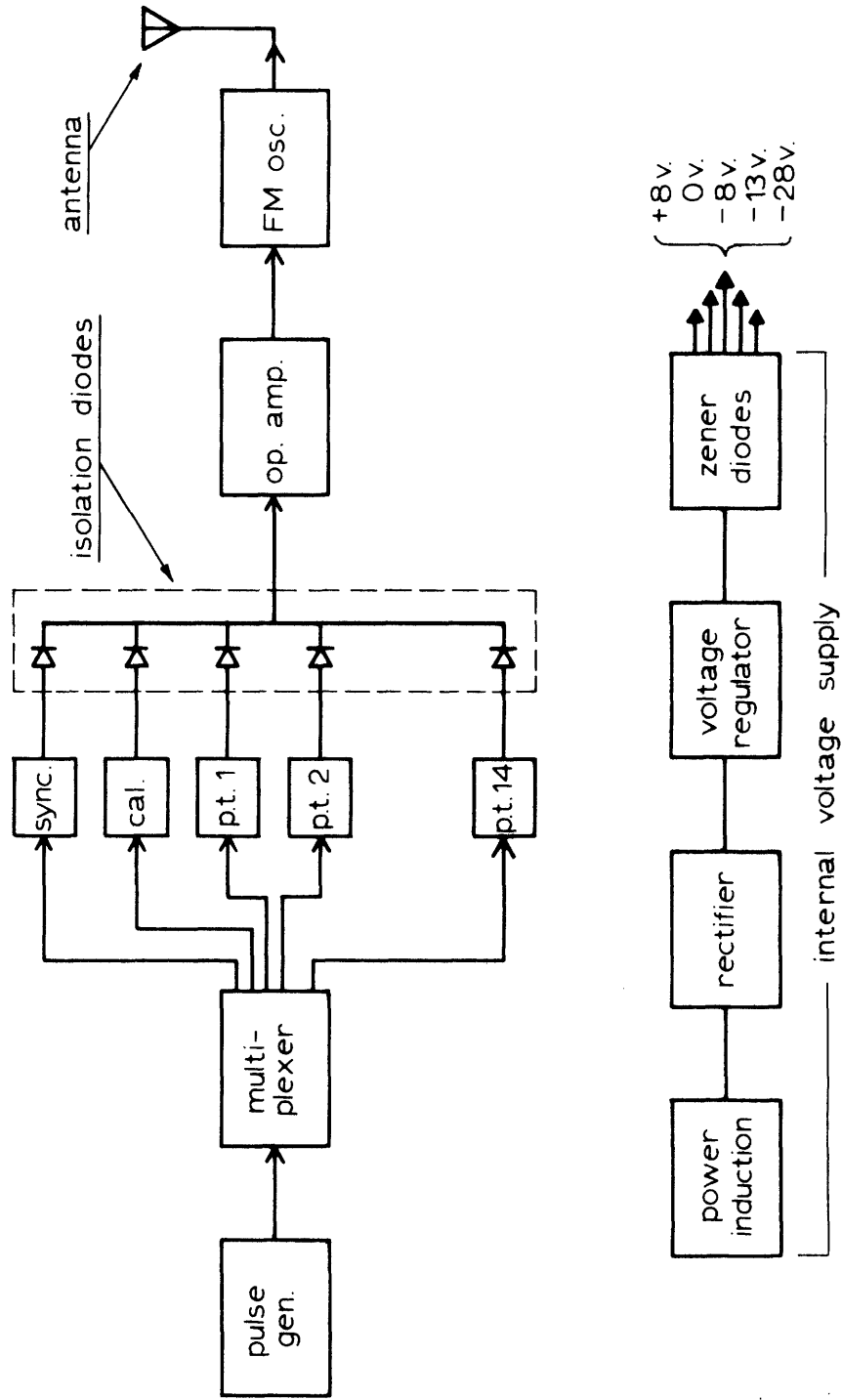
A block diagram of the telemetry device is shown in Figure E1. The circuitry in each of these blocks or stages and a description of the circuit operation is presented in the following sections.

Pulse Generator Stage. The circuit diagram of the pulse generator, together with a table describing the circuit operation, is shown in Figure E2. The generator consists of a MOSFET (metal-oxide-semiconductor field-effect transistor) quad 2-input NOR gate and a pair of RC timing circuits. R_1 and C_1 control the pulse repetition rate, while R_2 and C_2 determine the pulse width. The output of the generator is also shown in Figure E2.

The basic operation of this circuit is described most simply by the table in Figure E2 which gives the logic states at specific points in the circuit during one cycle. The letters A through F in the left-hand column refer to the points shown in the circuit of Figure E2. The NOR gates can be characterized as having a low output impedance and a high input impedance. A zero (0) logic state corresponds to zero volts, and one (1) state corresponds to -10 V. The arrows in the table indicate logic state changes that are controlled by the potential across a capacitor in an RC circuit.

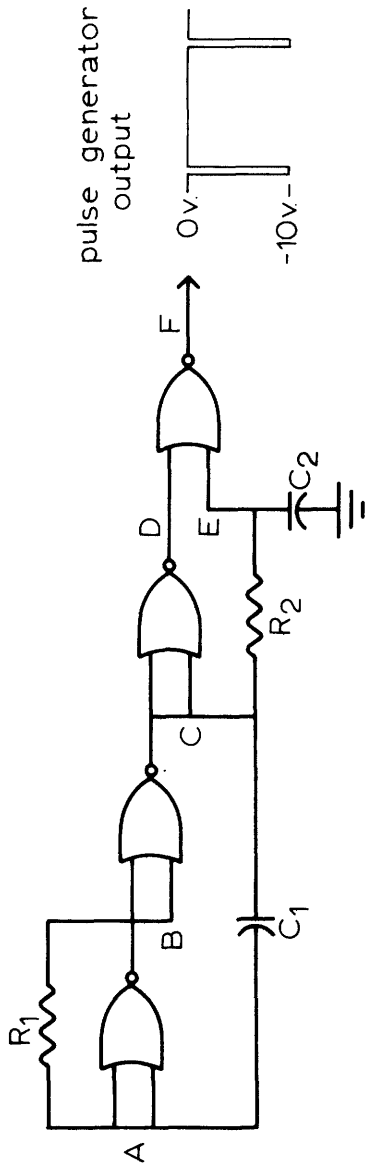
The minimum pulse width at the -10 V level required by the multiplexer for satisfactory switching is 2 μ sec. R_2 and C_2 are chosen to give a pulse width of approximately 4 μ sec.

The pulse repetition rate is the product of the sampling rate per channel and the total number of channels. Each channel is



BLOCK DIAGRAM OF TELEMETRY DEVICE.

Figure E1



time →

A	0	→ 1	1	→ 0	0	0
B	1	0	0	1	0	1
C	0	1	1	0	0	0
D	1	0	0	1	1	1
E	0	0	→ 1	1	→ 0	0
F	0	1	0	0	0	0

PULSE GENERATOR STAGE.

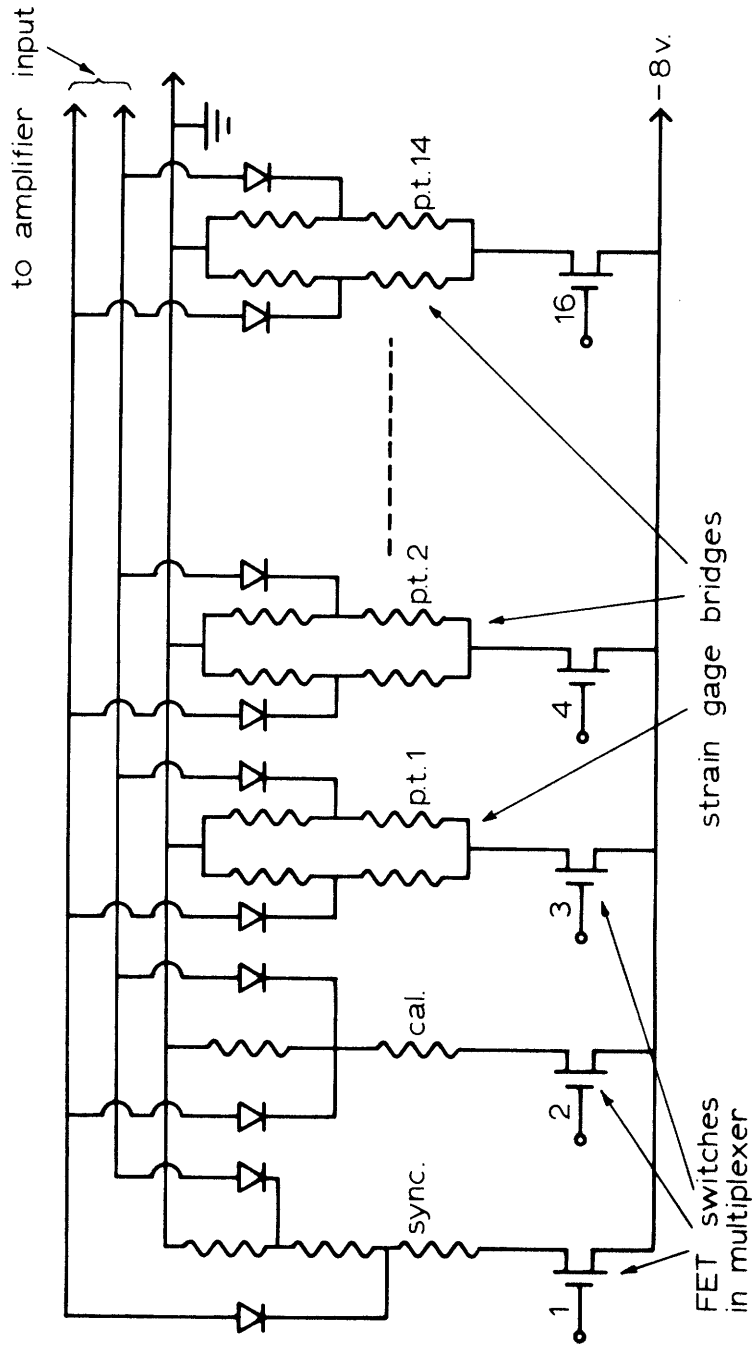
Figure E2

sampled 250 times per second. For sixteen channels the required pulse rate, controlled by R_1 and C_1 , is 4kHz.

Multiplexer and Pressure Transducer Stages. The multiplexer stage consists of one component--a sixteen-channel integrated circuit MOSFET multiplexer. The device contains a sixteen channel counter, composed of four flip-flop stages, a decoding matrix and sixteen FET switches. A pulse from the pulse generator advances the counter one step and the decoder matrix turns on the switch that corresponds to the counter output. Each channel is "on" for the full time period between pulses. The multiplexer switches the inputs of the transducer strain gage bridges, rather than switching the bridge outputs; only one bridge is energized at a particular instant. This is done primarily to minimize power consumption.

Figure E3 is a simplified schematic of the bridge switching circuitry. The resistors in channels 1 and 2 generate the synchronization and calibration pulses, and those in the remaining fourteen channels represent the strain gage bridges in the transducers. The FET switches are the sixteen switches in the multiplexer. The one switch that is "on" simply connects one of the input terminals of the bridge to a negative potential, energizing the bridge. The switches are operated sequentially, thereby scanning through the pressure transducers.

The FET switches typically have an "on" resistance of $1\text{ k}\Omega$. To maximize the input voltage to the bridges it is necessary to make the bridge resistance large relative to the switch resistance. In this case the bridge resistance is nominally $12\text{ k}\Omega$. The FET switch "off" resistance is on the order of $10\text{ M}\Omega$, which effectively



TRANSDUCER BRIDGE SWITCHING CIRCUITRY .

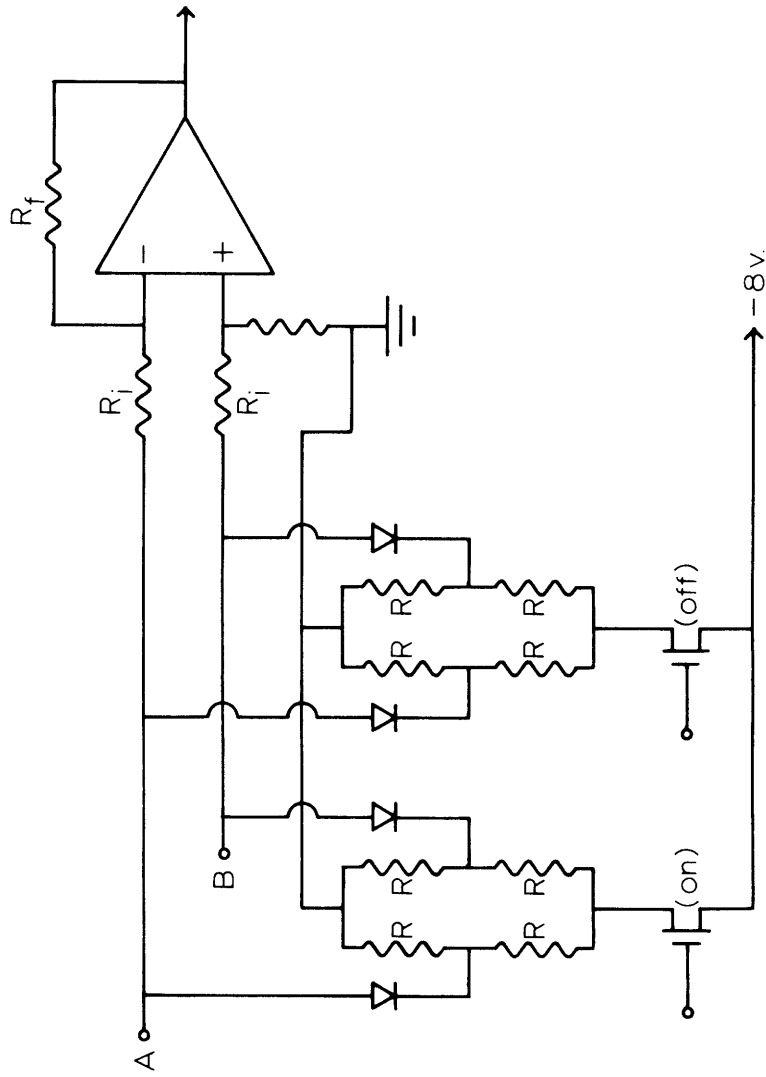
Figure E3

turns the bridges "off."

The circuitry for generating the synchronization and calibration pulses is shown in Figure E3. The synchronization pulse is generated by amplifying the voltage drop across a fixed resistor, while the calibration pulse is generated by connecting the input leads to the same potential. These two channels are switched by the multiplexer in the same fashion as the pressure transducer channels. The 5.6 k Ω resistors are chosen so that the resistance of these two circuits as seen by the multiplexer will nearly match the resistance of the pressure transducer bridges.

Diode Isolation Stage. The outputs of all of the pressure transducer bridges are connected to the differential input terminals of an operational amplifier in the amplifier stage. To prevent loading of the output of the one energized bridge by the other bridges that are "off", a diode isolation stage is employed. The circuit for two representative bridges is shown in Figure E4. The bridge isolation is achieved by inserting a pair of diodes for each bridge in the leads between the bridge output and the inputs to the amplifier.

The circuit works as follows: the output terminals of the one bridge that is "on" assume negative potentials that are roughly midway between ground and the negative input voltage. This bridge output potential forward biases the two diodes associated with the "on" bridge, causing leads A and B in Figure E4 to assume a negative potential. The output terminals of the bridges that are "off" are at ground potential, and thus the diodes on all of these bridges are reverse biased. These diodes present a high impedance and isolate the "off"



DIODE ISOLATION OF TRANSDUCER BRIDGES.

Figure E4

bridges from the inputs to the amplifier stage.

The isolation diodes are contained in four IC flatpacks containing eight diodes each. The diodes in each flatpack are connected in a common-anode configuration. The two diodes on each bridge do not have a common anode, so the diodes in each pair must be in different flatpacks. The diodes in each pair are matched to minimize offset in the bridge output voltage.

Amplifier Stage. A simple integrated circuit differential input operational amplifier boosts the transducer outputs to a level sufficient to modulate the transmitter stage. The basic circuitry for the amplifier and one transducer bridge is shown in Figure E5.

The gain of this amplifier is not determined wholly by the ratio of R_f to R_i ; the isolation diodes and the bridge itself have an influence on the gain. Specifically, the dynamic resistance R_D of the diodes must be included, and a factor of $R/2$ also must be added to R_i to calculate the correct gain. The equation for the gain of the amplifier is:

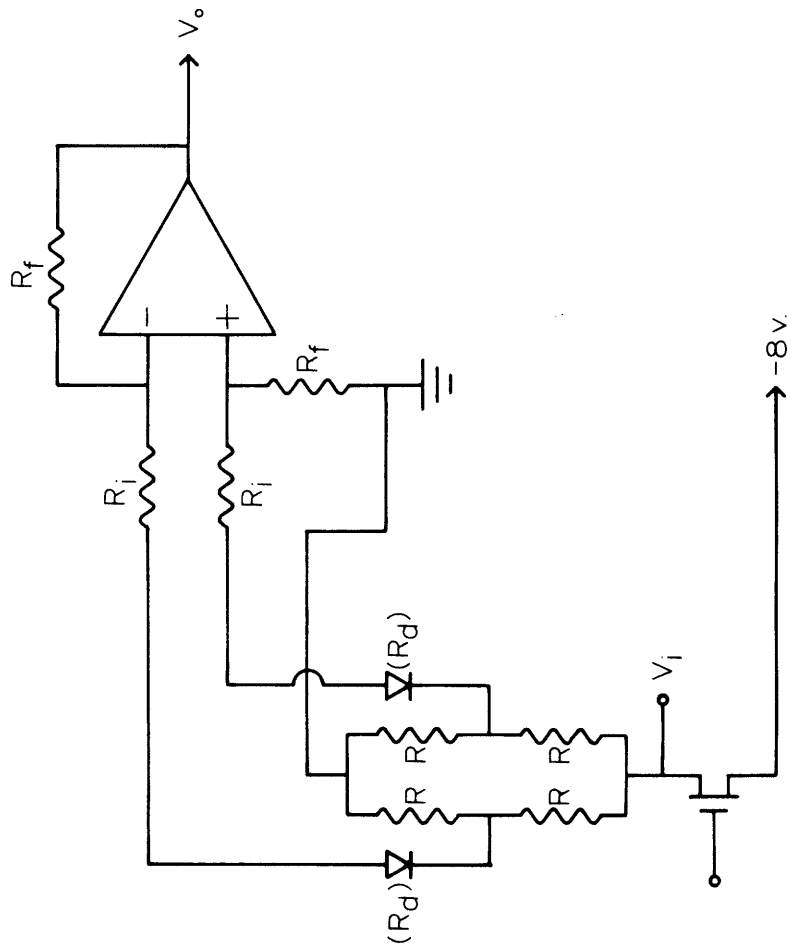
$$G = \frac{R_f}{R_i + R_D + \frac{R}{2}} .$$

The complete expression relating output voltage V_o to the change in resistance ΔR of each of the resistances R (which represent strain gages) is

$$V_o = V_i \cdot \frac{\Delta R}{R} \cdot \frac{R_f}{(R_i + R_D + \frac{R}{2})} ,$$

where V_i is the bridge input voltage (V_i is less than 8 V because of the voltage drop across the FET switch).

Several factors govern the selection of specific values for R_f



AMPLIFIER STAGE.

Figure E5

and R_i . The desired gain of the amplifier is one factor. The current flowing through the R_f , R_i and R_D should be much larger than the input bias current required by the amplifier. The current, however, should be small compared to the current in the bridge (V_i/R), so that the bridge output voltage is not significantly affected by this injected current. The dynamic resistance R_D of the diodes is a function of the current through them so that the choice of R_f and R_i determines R_D . Lastly, very large values of R_f affect the frequency response of the system; the input capacitance of the amplifier together with other circuit capacitance form an RC circuit whose time constant can be significant.

The values of R_f and R_i chosen for the circuit are 220 k Ω and 1.8 k Ω respectively. For these values the current through R_f , R_i and R_D is approximately 10 μ A. This current is well above the input bias current of the op amp (100 nA) and is small compared to the bridge current (600 μ A). The dynamic resistance R_D of the diodes at this current level is 3 k Ω . For a bridge resistance R of 12 k Ω , the amplifier gain is twenty.

The isolation diodes introduce a small nonlinearity into the gain, since the dynamic resistance R_D is a function of diode current. The diode in the lead connected to the noninverting (+) input of the amplifier has essentially a fixed value of current through it for all bridge output voltages. The diode connected to the inverting (-) input, however, has a significant change in current, since the feedback resistor R_f connected to the inverting input is connected to the amplifier output rather than a fixed ground potential. In the previous equation for op amp gain, R_D is added to R_i and $R/2$. In-circuit tests

show that the change in R_D due to changes in diode current is small in comparison to the total of these three resistances. The deviation from nonlinearity of the output voltage V_o as a function of ΔR is less than 2 or 3 percent over the full range of ΔR .

The expression relating output voltage V_o to the circuit values for the synchronization channel is not identical to the equation for the pressure transducer channels. The output voltage of this circuit, shown in Figure E6, is given by:

$$V_o = \frac{V_i R' R_f}{(R_i + R_D)(R' + 2R'') + R'R''} ,$$

For the resistances used in this circuit the output voltage is given with good accuracy by:

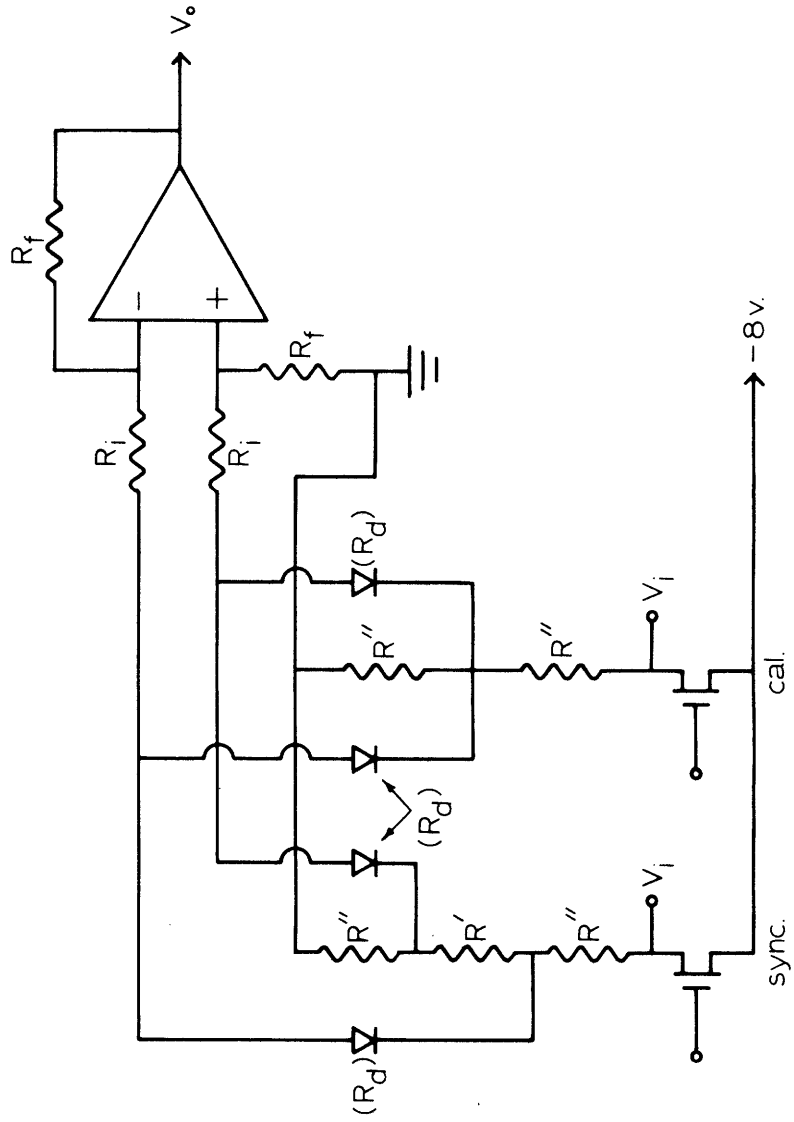
$$V_o = \frac{V_i R' R_f}{2R''(R_i + R_D)} .$$

A value for R' of 33Ω gives an output voltage of approximately 1 V. The other resistances are the same as in the previous case, with $R'' = 5.6 \text{ k}\Omega$.

The calibration channel is identical to the synchronization channel, except that R' is zero, and thus the output voltage V_o is zero.

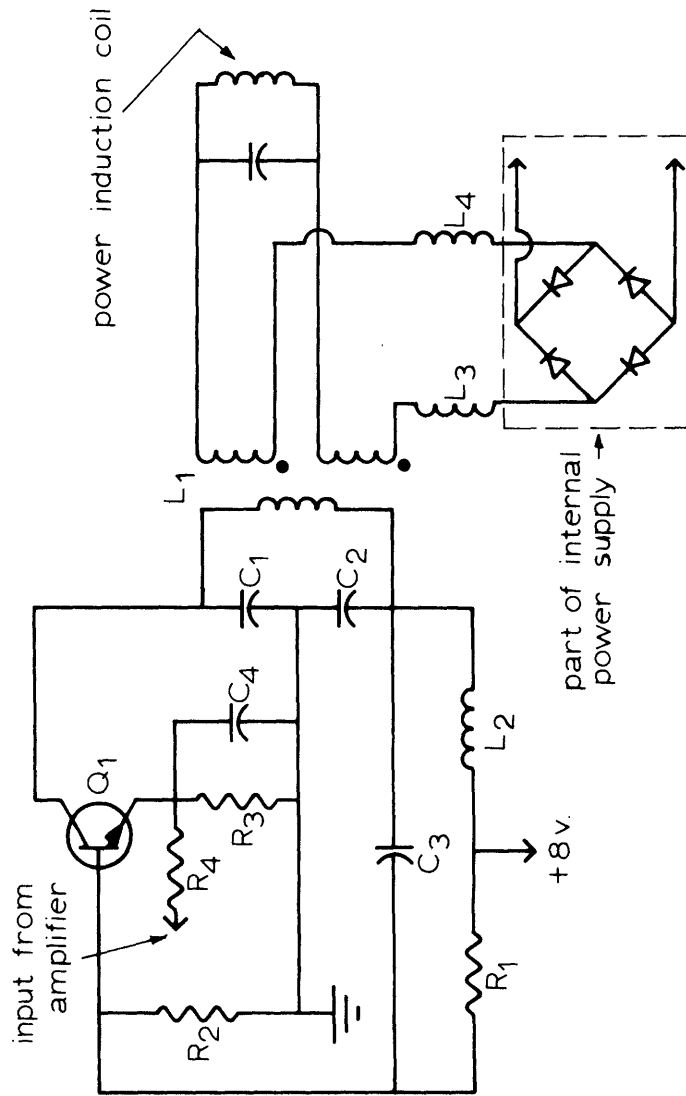
Oscillator Stage. A simple Colpitts oscillator, Figure E7, tuned to operate between 90 and 100 MHz transmits the information from the pressure transducers to an external receiver. L_1 , C_1 and C_2 set the nominal oscillator frequency, R_1 , R_2 and R_3 control the operating point, and C_3 , C_4 and L_2 serve as signal bypass and isolation elements.

The oscillator is frequency modulated by varying the base-to-emitter voltage. This change in bias causes the capacitance of the



SYNCHRONIZATION AND CALIBRATION CIRCUITRY .

Figure E6



OSCILLATOR STAGE AND ANTENNA COUPLING.

Figure E7

reverse-biased collector-to-base junction to change, which changes the capacitance of the LC tank circuit, causing a change in frequency. The base-to-emitter voltage is controlled by changing the emitter potential. The output of the amplifier is coupled to the transistor emitter by resistor R_4 . The amplifier injects a varying amount of current into R_3 , changing the voltage drop across R_3 and thus the base-to-emitter bias.

The magnitude of the oscillator frequency deviation for a given modulation voltage is adjusted by varying R_4 . It is desirable to have as large a frequency deviation as possible to maximize the received signal-to-noise ratio. R_4 is adjusted so that the largest pulse in the PAM input signal (in this case the synchronization pulse) causes a frequency deviation that substantially occupies the bandwidth of the receiver. A standard FM tuner has a bandwidth of 200 kHz. The maximum frequency deviation of the oscillator is adjusted to about 150 kHz, thus allowing the oscillator to drift slightly without requiring retuning of the receiver.

The oscillator frequency deviation is a nearly linear function of the input voltage over a frequency range of at least 200 kHz. The deviation from nonlinearity is within 2 to 3 percent.

The radio frequency signal generated by the oscillator is radiated by a coil mounted on the tip of the stem of the prosthesis. This coil, shown in Figure E7, serves two functions. In addition to serving as the transmitting antenna the coil is also the secondary winding of a simple transformer that couples power into the prosthesis from an external source. This power induction scheme is described in Appendix F.

The radio frequency energy in the tank circuit is coupled to the

external coil on the prosthesis through L_1 , the inductance in the oscillator tank circuit (see Figure E7). The two wires from the external coil are connected to a pair of two-turn windings on L_1 . The polarity of these windings is such that the magnetic fields generated by the equal but opposite currents in the windings tend to cancel, minimizing the voltage induced in L_1 by the power induction circuitry. L_3 and L_4 are chosen to be a high impedance at the signal frequency, 100 MHz, and a low impedance at the power induction frequency of 100 kHz. The presence of these two inductances minimizes loading of the oscillator tank circuit by the internal power supply circuitry.

The coupling between the oscillator tank circuit and the external coil through the two-turn windings on L_1 is quite small. This loose coupling minimizes the effects on the oscillator frequency of the presence of conductive objects near the external coil but requires a relatively high power oscillator if a sufficiently strong signal is to be radiated. The oscillator consumes approximately 50 mW of power. At this power level the signal-to-noise ratio at the output of the FM receiver located thirty feet from the prosthesis is quite satisfactory. The presence of bone and tissue surrounding the prosthesis appears to have very little effect on the transmitted signal. This is demonstrated by observing the received signal while cupping the radiating coil in one's hands.

The power pickup coil on the prosthesis stem is not intentionally designed to enhance the radiation of the 100 MHz signal. As far as the oscillator is concerned, the coil is merely a conductor that extends beyond the metallic shielding of the prosthesis and that is

capable of radiating some energy, albeit in a rather inefficient manner.

An ideal oscillator would have as one of its characteristics excellent frequency stability, i.e., it would change frequency only when the signal at its input terminal changed. In this respect the oscillator described in this section leaves something to be desired. The 100 kHz telemetry power frequency modulates the oscillator to a small extent; the peak-to-peak amplitude of the 100 kHz signal is about 20 percent of the synchronization pulse amplitude. Fortunately, the 100 kHz modulation is well above the 4 kHz PAM signal frequency, and a simple first-order filter will eliminate the 100 kHz signal while passing the amplitude information in the PAM signal.

Another potential source of frequency modulation is temperature changes. This type of very low frequency modulation is more commonly called "drift." The oscillator is reasonably insensitive to temperature changes--a change in ambient temperature from 80° F to 140° F causes a change in oscillator frequency of less than 200 kHz. Since the oscillator operates in an environment in which the temperature is rather well controlled, the oscillator frequency can be expected to be quite stable. Under continuous operation the temperature rise inside the ball of the prosthesis could be as much as 10° F to 15° F, but under the anticipated intermittent mode of operation the temperature rise should be much less. The rate of change of temperature in the prosthesis ball is quite slow, and any consequent changes in frequency could easily be followed by manually retuning the receiver.

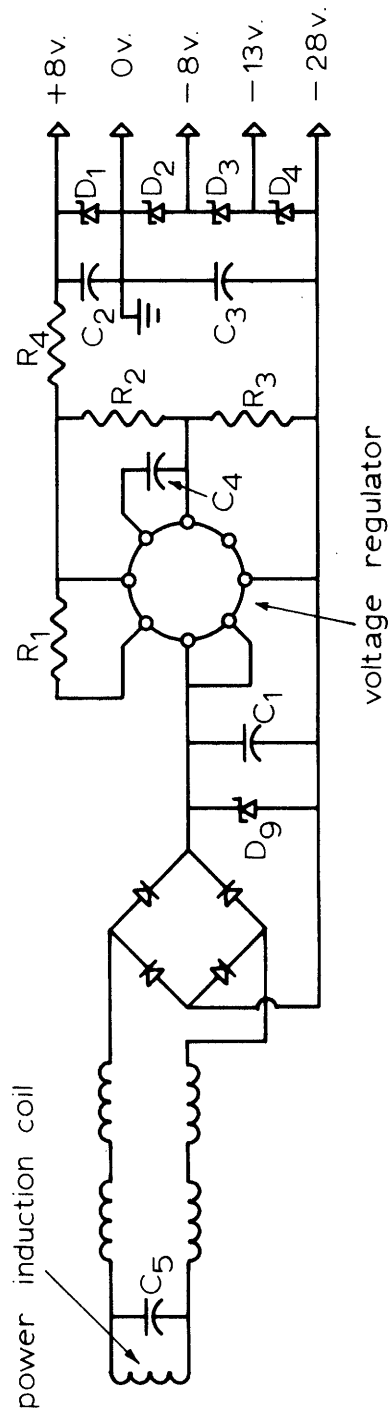
A third source of extraneous frequency modulation is caused by relative motion of the wires and components in the oscillator. The telemetry device will conceivably be subjected to significant impact

and shaking forces during normal use. This source of modulation is minimized by using components of small mass firmly mounted on a stiff supporting structure.

A fourth source of undesired frequency modulation, and one to which the oscillator is quite susceptible, is changes in the DC supply voltage. The oscillator is designed to be frequency modulated by varying the bias on the transistor, and a changing DC supply voltage very effectively changes the transistor bias. In the telemetry circuit this problem is eliminated by carefully controlling all of the circuit supply voltages.

Frequency modulation of the oscillator by extraneous sources is not necessarily a problem, as long as the undesired frequencies are much higher or much lower in frequency than the frame rate. The amplitudes of all of the pulses in the PAM signal are measured with respect to a zero reference level. This zero reference is the calibration pulse which is transmitted once during each frame. Variations in oscillator frequency due to very low frequency events, such as "drift" caused by temperature fluctuations, cause no difficulty, since the oscillator "zero" level is transmitted 250 times per second. Likewise, modulation frequencies that have several cycles during the 250 μ sec that each pulse is present can easily be filtered out (for example, the 100 kHz power frequency which superimposes 25 cycles on each pulse). Only those frequency variations that occur at or near the frame rate are potential sources of difficulty.

Power Supply Stage. The DC supply voltages required by the various sections of the telemetry device are supplied by the power supply stage whose circuit diagram is shown in Figure E8. The telemetry system is



POWER SUPPLY STAGE .

Figure E8

powered through the coil mounted on the stem of the prosthesis. This inductance is connected in a resonant circuit tuned to 100 kHz by C_5 . The voltage developed across this parallel LC circuit is rectified by a full-wave bridge, and the output of this bridge is partially smoothed by C_1 . The filtered DC then goes to an integrated circuit voltage regulator in which the output voltage is regulated by a series-pass element (a transistor).

Several supply voltages are required by the various stages of the telemetry system. The pulse generator requires -13 V and -28 V; the multiplexer, -28 V; the strain gage bridges, -8 V; the operational amplifier, ± 8 V; and the oscillator, +8 V. These potentials are all referenced to a ground potential. The required voltages are developed across a series string of four Zener diodes, D_1 through D_4 in Figure E8. The regulated output of the voltage regulator is connected to the Zener diodes through a series resistor, R_4 .

The Zener diode, D_9 in Figure E8, limits the input to the voltage regulator to less than 50 V, the maximum allowable input voltage. If the peak voltage from the rectifier exceeds approximately 47 V, D_9 conducts, effectively placing a low impedance load across the output of the 100 kHz tank circuit and thereby limiting the voltage generated in the tank circuit.

R_1 is an output current limiting resistor which limits the maximum current the regulator can supply, thereby protecting the regulator from abnormal load conditions. R_1 limits the charging current to C_2 and C_3 under certain circuit start-up conditions.

C_4 provides frequency compensation for the regulator. R_2 and R_3 set the output voltage. The output voltage is adjusted to produce

a current of 10 mA through R_4 . This current level is sufficient to insure that all of the Zener diodes, D_1 through D_4 , stay in the Zener breakdown region. C_2 and C_3 help minimize voltage fluctuations across the Zener diodes caused by transient changes in the circuit loads.

The decision to use active voltage regulation in addition to the passive regulation provided by the Zener diodes was based on several considerations. First, the voltage developed across the power induction coil can easily vary by as much as 20 to 30 percent, due to relative motion between the primary external coil around the test subject's leg and the secondary power pickup coil on the prosthesis. Second, the voltage regulation provided by a Zener diode alone is not sufficient to prevent serious extraneous modulation of the oscillator caused by large fluctuations in input voltage. In addition, the strain gage bridges in the pressure transducers are excited by a DC voltage, and small variations in the bridge input voltage cause corresponding changes in the bridge output that are difficult to distinguish from pressure fluctuations. Active voltage regulation in the power supply stage minimizes the above-mentioned problems and contributes to a transmitted signal that is "cleaner" and easier to handle with respect to data processing.

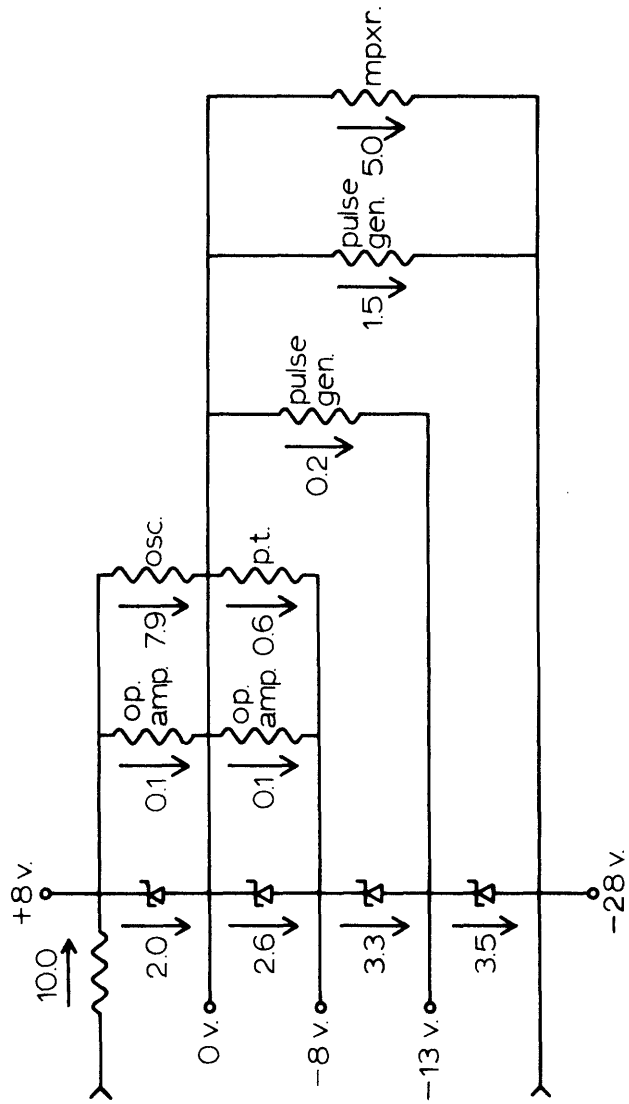
The active voltage regulator provides an output voltage of approximately 37.5 V that is essentially independent of voltage fluctuations on the input side. The 200 kHz ripple on the regulated output has a peak-to-peak amplitude of roughly 5 mV, while the ripple on the input side of the regulator is about 2 V.

The 37.5 V regulated output is equally insensitive to changes

in load. However, the presence of the series resistor R_4 degrades the voltage regulation across the Zener diodes--variation in circuit loads cause corresponding voltage drops across R_4 . Fortunately, all of the loads due to the various stages of the telemetry circuitry are quite stable, at least during the 250 μ sec periods when the transducers are "on". Some load variations occur during the switching period, but these transients last for only a few microseconds.

The current flow through the Zener diode string and the various telemetry stages is shown in Figure E9. The current delivered by the voltage regulator is such that all of the diodes have a minimum of 2 mA flowing through them, insuring that the diodes stay well in the Zener breakdown region for the range of expected operating conditions. Using a series of Zener diodes to set the operating voltages is rather inefficient; with the Zener currents shown in Figure E9 more than 20 percent of the total power utilized by the telemetry system is dissipated in the Zener diodes. If power were at a premium, this method of obtaining several DC supply voltages would be very unsatisfactory. However, since a relatively large amount of power for the device is available through the power induction system, the Zener diodes provide a simple means of obtaining the operating voltages.

In general, the IC devices selected for use in the various stages were chosen to minimize power consumption. The oscillator, however, is designed to use as much power as possible (up to approximately 60 mW) while still maintaining the minimum Zener current levels. If the oscillator did not fully utilize the power available to it, this power would be dissipated in a Zener diode.



CURRENT FLOW IN MILLIAMPERES
THROUGH TELEMETRY DEVICE STAGES.

Figure E9

Heating of Prosthesis Due to Power Dissipation in Telemetry System

The telemetry device inside the prosthesis dissipates approximately 500 mW of power. A conservative estimate of the steady-state temperature rise of the surface of the ball was calculated by assuming that the ball is in a material of uniform thermal conductivity of infinite extent. The value of the thermal conductivity used in this calculation was 0.001 cal/cm sec °C (Ref. 20). The temperature rise of the surface of the ball is about 7° F for 500 mW dissipation inside the ball. The time required to reach this equilibrium temperature is on the order of 30 minutes.

A temperature rise of this magnitude is undesirable from a medical point of view, and it could significantly disturb the normal behavior of cartilage and synovial fluid, possibly affecting the pressure distribution.

To minimize heating in the prosthesis the telemetry system will be energized during the test sessions only when measurements are being made. The measurement times in the individual tests should be no more than three to five minutes. The temperature rise of the prosthesis can be held to a negligible amount by allowing appropriate "cooling-off" periods between test runs.

Legal Requirements for Operation of Telemetry System

Operation of the 100 MHz signal oscillator used in the telemetry system is governed by Part 15, Radio Frequency Devices, of the Federal Communications Commission Rules and Regulations. The technical requirements are set forth in Subpart E--Low Power Communication Devices, Section 15.212, Telemetering devices and wireless microphones in the band 88-108 MHz.

Briefly, the requirements are:

1. Operation must be within the frequency limits of 88-108 MHz.
2. Users must take adequate precautions to insure that the telemetry device does not cause any interference with other licensed stations.
3. The radiated signal must lie within a band 200 kHz wide which lies wholly within the 88-108 MHz band.
4. The field strength of the signal radiated inside the 200 kHz band must not exceed 50 $\mu\text{V}/\text{m}$ at a distance of 50 ft or more.
5. The field strength of the signal radiated outside the 200 kHz band must not exceed 40 $\mu\text{V}/\text{m}$ at a distance of 10 ft or more.

The first and third requirements are definitely met by the telemetry system. The second requirement is met by choosing a frequency in a relatively "quiet" area in the 88-108 MHz band; this minimizes interference from, as well as interference to, local FM broadcast stations. Whether or not the fourth and fifth requirements are met is unknown. No attempt has been made to measure the field strength of the radiated signal. The received signal has a satisfactory signal-to-noise ratio at a range of thirty feet.

Telemetry Device Packaging

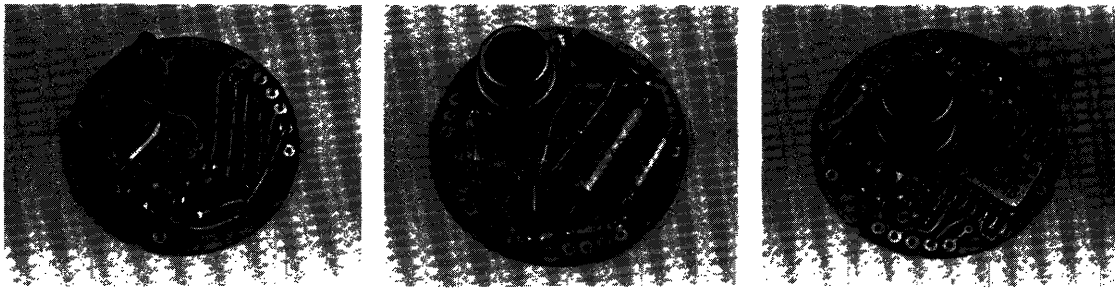
The various stages of the telemetry device are constructed on five circular, double-sided printed circuit boards which are then connected together in a layer-cake assembly. The boards are supported by stiff wires passing through holes in the peripheries of the boards. These wires also serve as the electrical interconnections. The

individual boards are shown in Figure E10, and the assembled unit is shown in Figure E11. Chip resistors and capacitors are used throughout, except for some large value electrolytic capacitors on the power supply board.

The diode board has two rings of holes around its circumference-- the inner ring makes connections with the other boards, and the outer ring of holes makes connections with the pressure transducer bridges through an annular terminal ring.

The method of mounting the telemetry device in the hemisphere is illustrated in Figure E12. After the pressure transducers have been mounted, a metal ring with a small internal flange is attached to the hemisphere. The terminal ring is mounted on this flange and the wires to the transducers are attached to the ends of the pins in this ring which extend into the hemisphere. The telemetry unit is slipped over the opposite ends of the pins in the ring with the pins passing through the appropriate holes in the outer ring of holes in the diode board. The various electrical connections are soldered and the complete telemetry device assembly is fastened in place by a bead of silicone rubber cement around the circumference of the diode board and terminal ring.

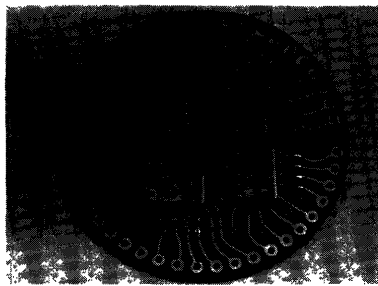
One side of the oscillator board is exposed after the telemetry unit has been mounted in the hemisphere. The resistor which controls the magnitude of the frequency deviation of the oscillator for a given input signal is accessible on this board, as are the two capacitors in the oscillator tank circuit which control its nominal frequency. This arrangement allows the ratio of frequency deviation to signal amplitude and the oscillator frequency to be trimmed after



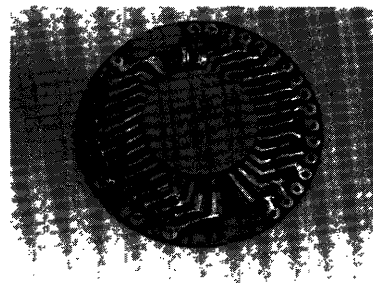
Oscillator Board

Power Supply Board

Pulse Generator
& Op Amp Board

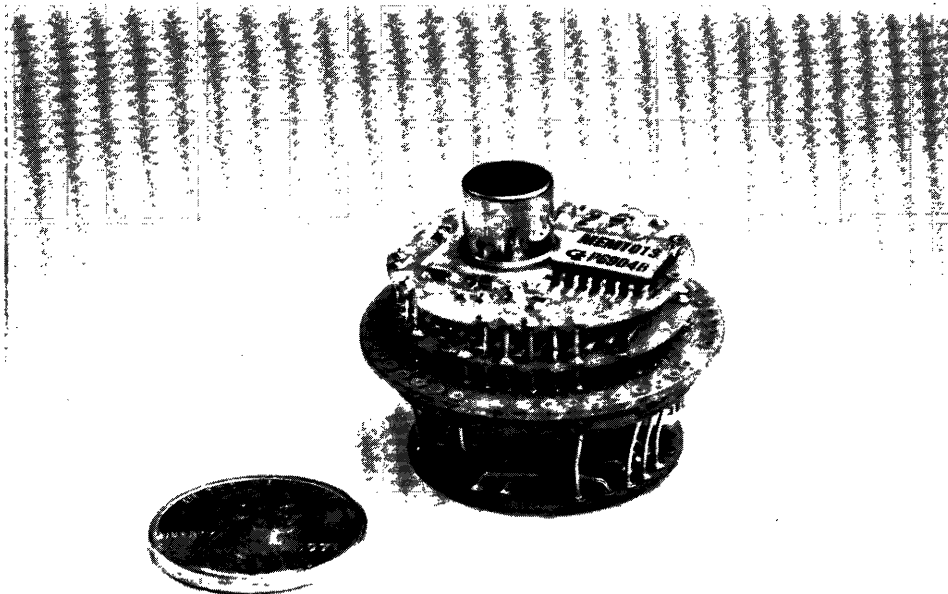


Diode Board



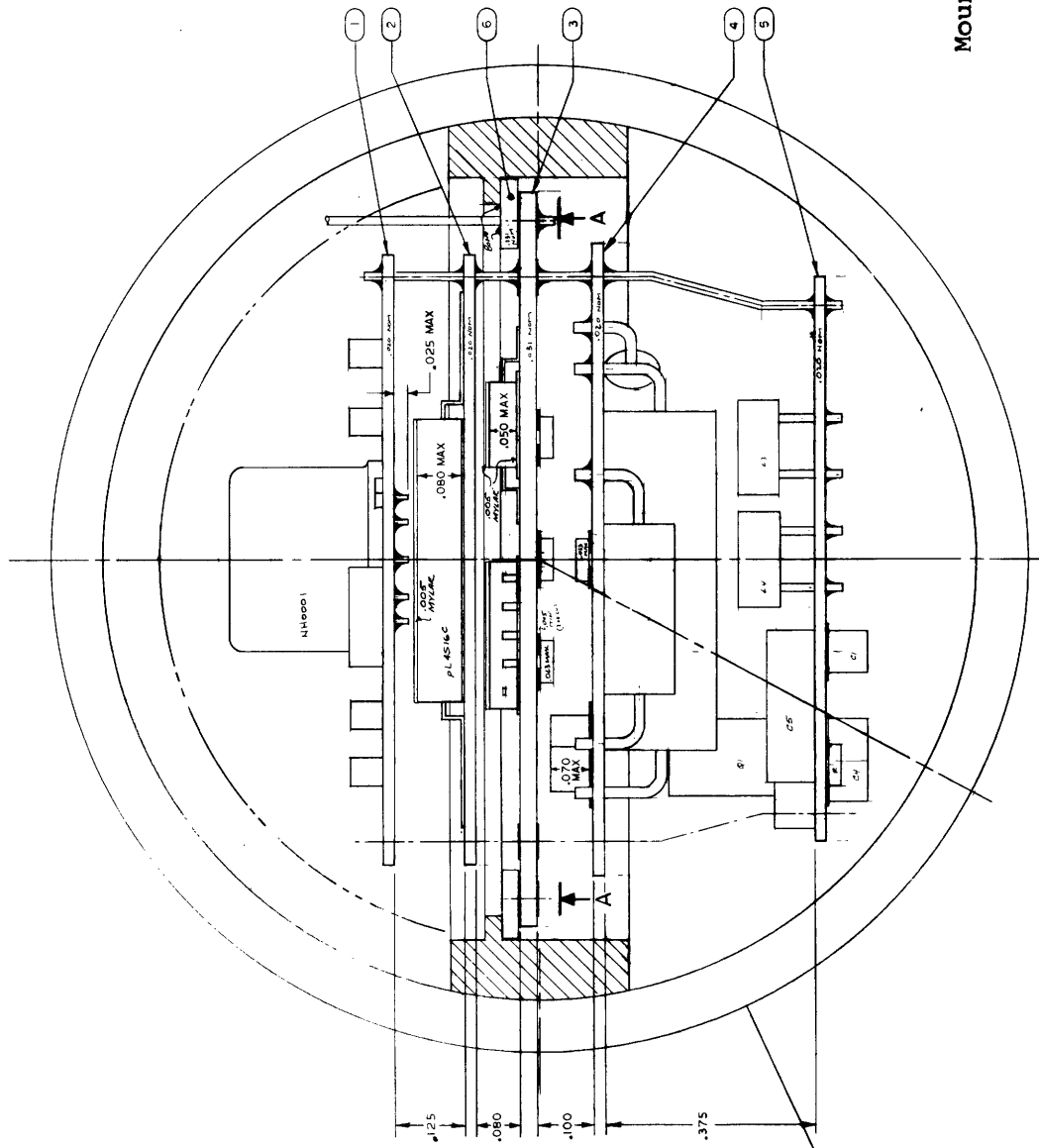
Multiplexer Board

Individual Printed Circuit Boards in Telemetry Device
Figure E10



Assembled Telemetry Device
Figure E11

1. Pulse Generator and Op Amp Board
2. Multiplexer Board
3. Diode Board
4. Power Supply Board
5. Oscillator Board
6. Annular Terminal Ring



Mounting Arrangement of Telemetry Device in Hemisphere

Figure E12

the telemetry unit has been mounted in the hemisphere. This is particularly important with respect to oscillator frequency, which is shifted significantly by the proximity of the metal halves of the ball of the prosthesis.

When these final adjustments have been completed the two wires from the coil in the stem part of the prosthesis are soldered to a pair of terminals on the oscillator board and the ball of the prosthesis is closed.

Pressure Transducer/Telemetry System Calibration

After the instrumented prosthesis has been completely assembled the telemetry system and the fourteen pressure transducers are calibrated by applying a series of known pressures to each of the transducers and recording the amplitudes of the pulses for the corresponding telemetry channel. This calibration procedure is necessary for two reasons. First, there is some small variation in sensitivity among the pressure transducers, and second, each channel has a small, fixed amount of zero offset. The variations in transducer sensitivity are caused by small differences in the physical construction of the transducers and slightly different gage factors for the strain gages in the cantilever beams. The zero offset is due to imperfect balancing of the strain gage bridges when the cantilever beam holder assembly is mounted in the hemisphere.

All pressures are measured by comparing the amplitudes of the pressure transducer signals to the fixed difference in amplitude between the synchronization and calibration channels. This fixed reference amplitude is transmitted in each frame and provides a known pressure reference for each channel. Thus, the pressure information is sent in terms of relative rather than absolute

amplitudes and is not affected by changes in amplification in any stage of the telemetry system.

The calibration procedure is as follows. First, the telemetered signal is recorded with zero pressure applied to the transducers. The zero signal amplitudes, measured from the calibration channel level, are recorded as a percentage of the reference amplitude. This establishes the zero pressure level baseline relative to the reference level. Then a series of known pressures are applied to the pressure transducers individually and the corresponding telemetered amplitudes are measured from the calibration channel level and recorded. Each recorded value is then corrected by the previously measured zero offset and the corrected value is compared to the reference amplitude. The resulting ratio is then recorded for that pressure.

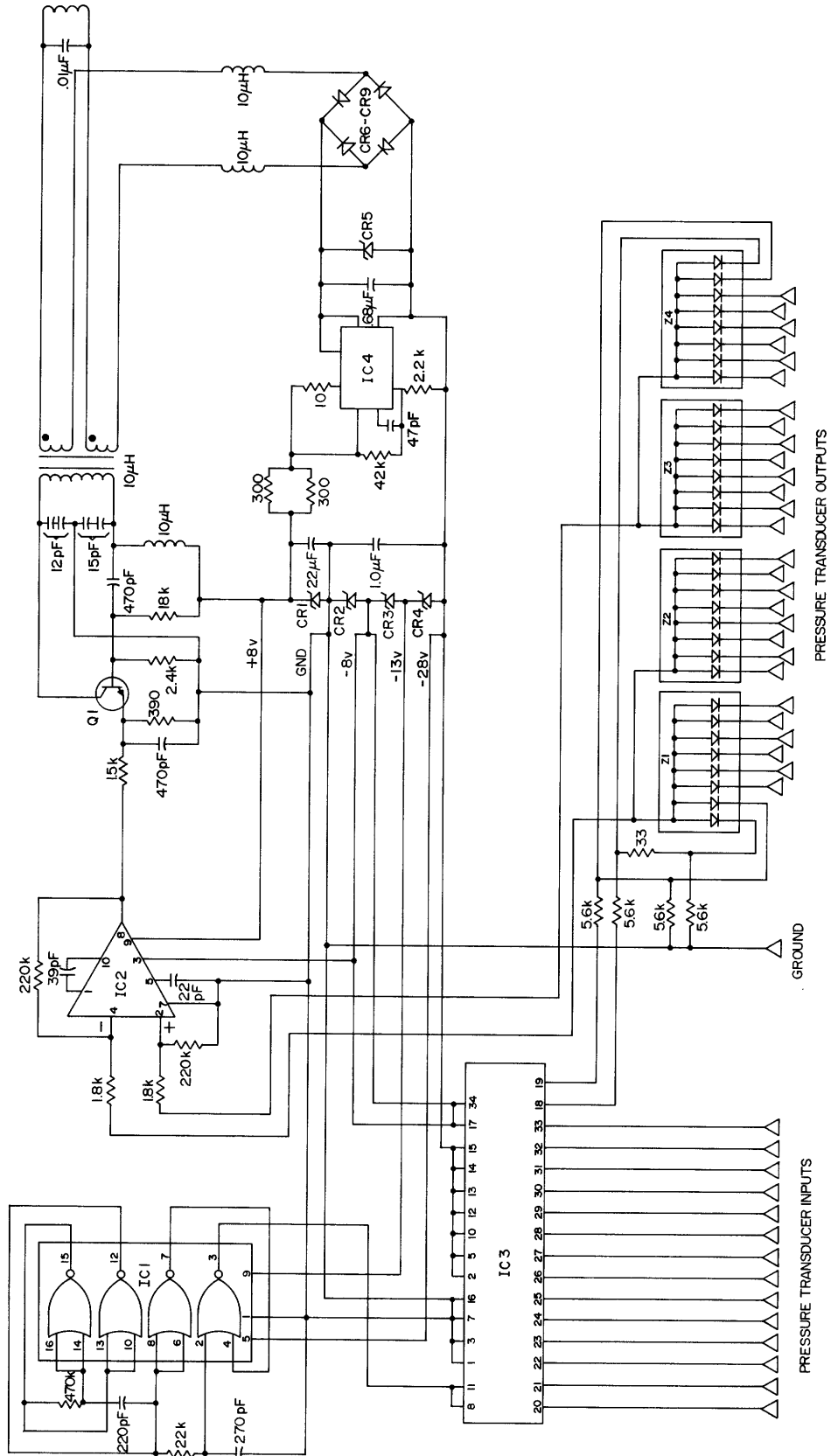
Theoretically the pressure transducer/telemetry system is very nearly linear, but if for some reason there is a significant nonlinearity this calibration procedure will allow the received pressure information to be corrected for this nonlinearity.

The sensitivities of the pressure transducers are quite stable. The zero offsets, however, may not be so stable over a long period of time. It may become necessary to re-establish the zero pressure baseline after the prosthesis has been implanted, and this can be done by literally pulling the test subject's leg. The instrumented hip would be placed in traction and the telemetered signal would be recorded for various leg angles. The lowest recorded pressures for each channel would then represent the new zero-pressure levels.

Telemetry Device Schematic

The schematic diagram of the sixteen channel transmitter is shown in Figure E13. The pressure transducers are not shown. Those parts whose values or designations are not indicated in the schematic are listed below.

IC1	MEM1013	General Instrument Corp. (not currently available)
IC2	NH0001C	National Semiconductor Corp.
IC3	pL4S16C	Philco Ford Microelectronics Div. (not currently available)
IC4	LM205	National Semiconductor Corp.
Z1-Z4	TID23A	Texas Instruments, Inc.
CR1, CR2	1N4101	8.2 V Zener
CR3	MZ4624	4.7 V Zener
CR4	1N4109	15 V Zener
CR5	1N5261B	47 V Zener
CR6-CR9	1N4934	
Q1	2N3663	



Sixteen-Channel Transmitter

Figure E13

APPENDIX F

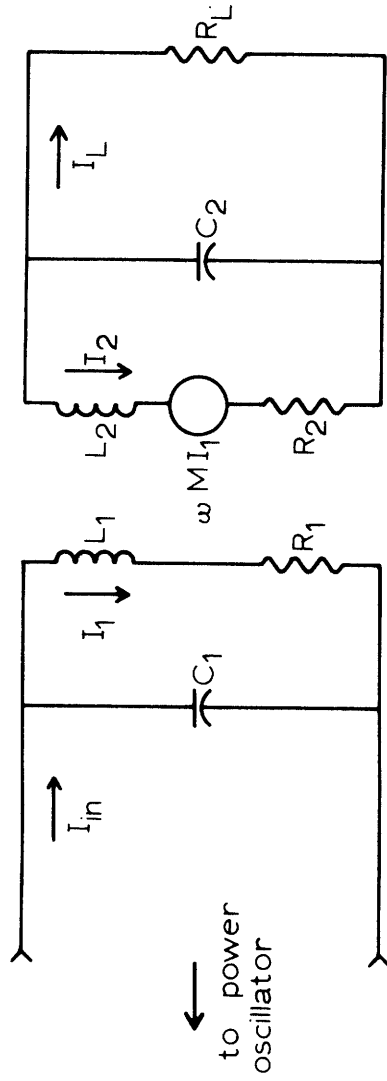
POWER INDUCTION SYSTEM

The implanted telemetry system is powered externally through a simple transformer arrangement. A primary coil placed around the test subject's thigh couples power to a secondary coil mounted on the tip of the prosthesis stem.

Although relatively large amounts of power are available to operate the telemetry device, it is desirable to maximize the efficiency of the power induction system in order to minimize the power losses and consequent heating in the external and internal coils. Optimum efficiency is particularly important if the external power source is to be carried by the test subject. Minimum power levels also contribute to the test subject's safety.

A model of the power induction system is shown in Figure F1. Both the primary and secondary coils are operated in parallel resonant circuits. The use of resonant circuits is necessary for reasonable circuit efficiency. L_1 and L_2 are the primary and secondary coils, respectively, and C_1 and C_2 are their associated resonating capacitors. R_1 and R_2 are the resistances of the coils, and R_L represents the load placed on the secondary resonant circuit by the telemetry circuitry.

The analysis of the circuit in Figure F1 is simplified considerably by assuming that the coefficient of coupling between L_1 and L_2 is small, so that the secondary circuit has a negligible influence on the currents and voltages in the primary circuit. In view of the physical sizes and the separation of the coils this assumption is quite reasonable. The power induction circuit can then be separated into three independent sections for analysis: the primary circuit,



POWER INDUCTION CIRCUITRY .

Figure F1

the coupling between L_1 and L_2 and the secondary circuit.

The primary resonant circuit $L_1 C_1$ has basically two functions-- to generate a magnetic field of maximum intensity and to present a suitable resistive load to the power oscillator. The magnetic field intensity is maximized by maximizing the current I_1 through the turns of L_1 (Figure F1) for a given power input P_{in} from the power oscillator.

P_{in} is given by $|I_{in}|^2 \cdot Z_{in}$, where

$$Z_{in} = \frac{(Z_{L_1} + R_1)Z_{C_1}}{Z_{L_1} + R_1 + Z_{C_1}}$$

in which

$$Z_{L_1} = j\omega L_1 \text{ and } Z_{C_1} = \frac{1}{j\omega C_1} .$$

At resonance $Z_{L_1} = -Z_{C_1}$. The ratio of the magnitude of Z_{L_1} to R_1 is typically greater than 10, so that Z_{in} is given with negligible error

by

$$Z_{in} = \frac{\omega^2 L_1^2}{R_1} .$$

At resonance the relationship between I_1 and I_{in} is

$$|I_1| = \frac{\omega L_1}{R_1} \cdot |I_{in}| .$$

Expressing I_1 as a function of P_{in} results in the following equation:

$$|I_1| = \frac{\omega L_1}{R_1} \cdot \left[\frac{P_{in}}{Z_{in}} \right]^{1/2} = \frac{\omega L_1}{R_1} \cdot \left[\frac{P_{in} R_1}{\omega^2 L_1^2} \right]^{1/2}$$

or

$$|I_1| = \left[\frac{P_{in}}{R_1} \right]^{1/2} .$$

The magnetic field intensity at any given point in the vicinity of the primary coil is proportional to $N \cdot |I_1|$, the product of the coil current and the number of turns in the coil. The expression for $N \cdot |I_1|$ is

$$N \cdot |I_1| = N \cdot \left[\frac{P_{in}}{R_1} \right]^{1/2} .$$

This equation indicates that the magnetic field intensity is maximized for a given power input by choosing an inductor L_1 which has a large number of turns and a low resistance.

The need for an external coil of minimum size and weight effectively limits the magnetic field intensity that can be achieved for a given P_{in} , since a coil with a large number of turns of low resistance (large diameter) wire is physically large.

In order to minimize the required power capability of the external source (and thus its size and weight), Z_{in} should match the output impedance of the power source. The expression for Z_{in} , as shown previously, is

$$Z_{in} = \frac{\omega^2 L_1^2}{R_1} .$$

Maximizing the magnetic field intensity causes Z_{in} to increase for fixed ω , since L_1 is proportional to N^2 for this particular coil. Z_{in} can be matched to the power source output impedance by a transformer, but the transformer may significantly add to the size and weight of the external power induction equipment. If a transformer adds too much bulk to the external equipment, the magnitude of the maximum magnetic field intensity possible for a given P_{in} may be limited by power oscillator output impedance.

The frequency at which the circuit is driven is 100 kHz. The

reasons for choosing this frequency are discussed subsequently.

The second part of the power induction system analysis concerns maximizing the flux density through the windings of L_2 , the coil mounted on the tip of the prosthesis stem. The maximum diameter of L_2 is limited by the space available in the marrow cavity and the mechanical shielding around the coil necessary to isolate it from body tissues and fluids. These considerations limit the diameter of L_2 to less than 0.2 in. The coupling between an air-core coil of this diameter located concentrically in another air-core coil large enough in diameter to slip over a person's thigh is very small. The addition of a high permeability ferrite core inside L_2 greatly increases the coupling between L_1 and L_2 and makes the power induction scheme practical. The ferrite core provides a low reluctance path for the magnetic field and greatly increases the flux density through L_1 . The particular ferrite chosen for this application has a permeability of 3000, compared to a figure of 1 for air.

It is desirable from a coupling efficiency viewpoint to maximize the cross-sectional area of this core. The diameter of the core used inside L_2 is 0.150 in.

The third part of the power induction system consists of the secondary winding L_2 , its resonating capacitor C_2 and the load R_L which represents the telemetry system. The pertinent circuit is shown in Figure F1. R_2 is the resistance of L_2 , and ωMI_1 is the voltage induced in L_2 by the magnetic field set up by the current in L_1 .

Again, to maximize coupling efficiency, it is desirable to minimize the losses in the coil resistance R_2 . The ratio of I_2 (the current through R_2) to I_L (the load current) at resonance ($Z_{L_2} = -Z_{C_2}$)

is

$$\frac{I_2}{I_L} = \frac{R_L - Z_{L_2}}{Z_{L_2}} .$$

The ratio of the power delivered to the load R_L to the power lost in R_2 is given by

$$\frac{P_L}{P_{R_2}} = \frac{|I_L|^2 R_L}{|I_2|^2 R_2} .$$

Substituting from the previous equation yields

$$\frac{P_L}{P_{R_2}} = \frac{R_L \omega^2 L_2^2}{(R_L^2 + \omega^2 L_2^2) R_2} .$$

From this equation it can be seen that the ratio of P_L to P_{R_2} is maximized by making R_2 small and ωL_2 large.

A practical constraint on the maximum value of the inductance L_2 is the space available for it. The coil used for L_2 has 120 turns of #30 silver wire wound in two layers on the ferrite core. The inductance of this coil (L_2) is about 250 μH , and its resistance is slightly less than one ohm.

The power lost in the coil resistance R_2 can now be calculated from the above formula. For a load resistance R_L of 5000 Ω and a frequency of 100 kHz, the ratio of P_L to P_{R_2} is very nearly five, so that 100 mW are dissipated in the coil when 500 mW are delivered to the load. The numerical values in the denominator of the above equation indicate that R_L^2 is much larger than $\omega^2 L_2^2$; hence, the ratio P_L/P_{R_2} could be readily increased by increasing the frequency at which the circuit operates.

A frequency of 100 kHz was chosen primarily because it was the upper frequency limit of the available power oscillator. The overall efficiency of the power induction system, i.e., the ratio of the power delivered to the load to the total power in, is about 10 percent, a figure that is acceptable in view of the power levels involved. The telemetry system requires 500 mW. The lost power, about 4.5 W, is dissipated primarily in L_1 , the external coil which circles the thigh of the test subject. The size of this coil is such that its temperature rise is only a few degrees Fahrenheit. The power dissipated in body tissues is virtually zero at this power level and frequency (Ref. 14).

For maximum efficiency the resonant frequencies of the primary and secondary tuned circuits must be equal, and the power oscillator must be adjusted to this frequency. Since the secondary circuit is not adjustable once the instrumented prosthesis has been assembled, the primary circuit and oscillator must be adjusted to match the resonant frequency of the secondary circuit. This alignment of frequencies is performed by monitoring the frequency of the 100 MHz oscillator in the telemetry system.

The 100 MHz oscillator frequency is quite sensitive to variations in its DC supply voltage. This voltage can be controlled by reducing the input power to the point where the input voltage to the voltage regulator in the internal power supply is insufficient to maintain a regulated output voltage. The 100 MHz oscillator frequency then becomes a sensitive indicator of the power delivered to the telemetry system. C_1 , the resonating capacitor in the primary circuit, and the power oscillator are then adjusted to maximize the coupling efficiency. Once

the primary circuit and power oscillator have been adjusted, the input power is increased to the point where unfavorable relative positions of the primary and secondary coils do not decrease the power input below the level required for satisfactory operation of the telemetry system.

When the telemetry system is energized the test subject will experience no sensation. The peak voltage at the input to L_1 , the external coil, is less than 50 V, and the coil and associated wiring are well insulated.

APPENDIX G

DATA ACQUISITION, STORAGE AND COMPUTATION

Telemetry System Receiver

The frequency modulated signal transmitted by the 100 MHz oscillator is received and demodulated by a standard FM broadcast receiver. The particular receiver used has a ratio detector type of demodulator, and the output of the detector is the desired PAM signal. A simple amplifier circuit is connected to the ratio detector output to boost the signal level and isolate the ratio detector from data recording and display equipment. This amplifier is followed by a low pass filter to eliminate the extraneous 100 kHz power frequency signal from the basic PAM signal. No other equipment is required to recover the PAM signal.

From the viewpoint of the complete telemetry system, the most difficult PAM signal to handle is one in which the pulse amplitudes alternate between zero and the maximum value, essentially producing a 2 kHz square wave. The frequency response of a good quality stereo receiver extends from approximately 20 Hz to 75 kHz, so the receiver is capable of reproducing a very clean 2 kHz square wave, or any other PAM signal whose fundamental pulse width is 250 μ sec.

Telemetry Data Recorder

The simplest and most practical method of recording the telemetered data is to record the PAM signal directly onto a single track on a magnetic tape. This procedure records the data in its purest form and requires no additional signal processing equipment, but it does require a tape recorder with suitable frequency response.

To adequately record and reproduce the PAM signal, the recorder does not have to be capable of reproducing exactly the received PAM signal waveform. Since the amplitudes of the pulses contain the pressure information, the frequency response of the magnetic tape recorder needs only to be such that the reproduced signal reaches a steady-state value within the 250 μ sec pulse width period. For practical reasons it is desirable that the reproduced pulse reach a steady-state within approximately 150 μ sec to simplify the pulse amplitude measurement made by subsequent data processing equipment.

Again the most difficult PAM signal to record and reproduce is one which resembles a 2 kHz square wave. Experimental tests have indicated that a magnetic tape record/reproduce unit having a frequency response extending to 10 times the fundamental square wave frequency satisfactorily reproduces the amplitudes of a 2 kHz square wave signal.

Typical instrumentation quality recorders operating in the FM mode at a tape speed of 60 in. per second are capable of a frequency response of DC to 20 kHz with good stability and signal-to-noise ratio. Such a recorder is entirely adequate for recording the telemetered PAM signal.

Data Processing

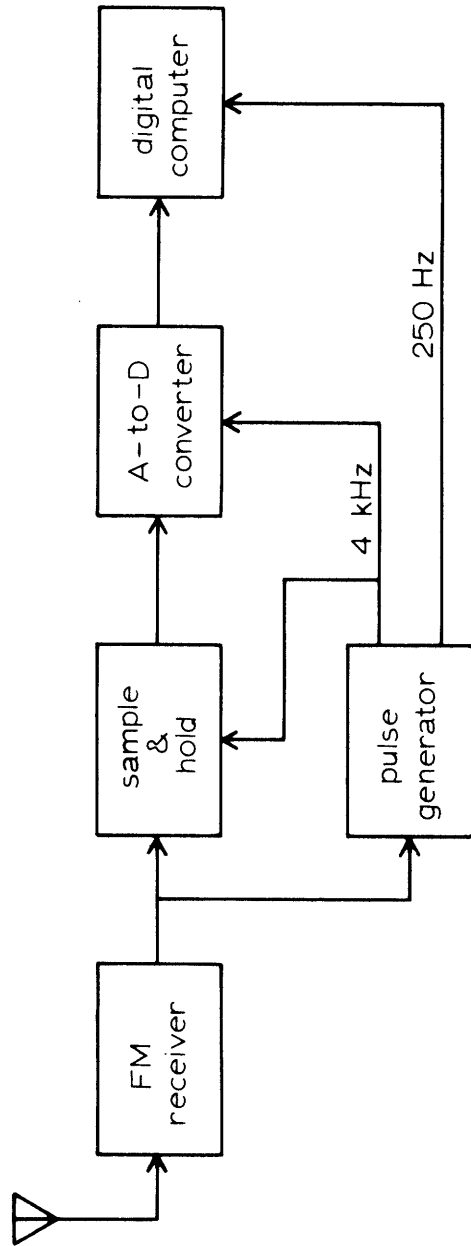
In view of the rate at which data are produced by the telemetry system (~4000 samples per second), manual manipulation of the data is impractical except for very simple measurements. Relatively complex operations, such as interpolating to find the pressure magnitude at locations on the prosthesis hemisphere between pressure transducers

or integrating the pressure distribution to find the magnitude and direction of the resultant load, are practical only if a digital computer is used.

The serial presentation of data in the time multiplexed PAM signal is a format that can readily be converted to a form compatible with a digital computer input. The necessary signal processing equipment consists of a pulse generator that is keyed to the nominal 4 kHz sampling rate, a sample-and-hold unit, and an analog-to-digital convertor. The block diagram of these units is shown in Figure G1.

The pulse generator basically consists of a voltage-controlled oscillator (VCO) whose frequency is maintained at the sampling rate by a phase-locked loop. A level sensor detects the synchronization pulse at the beginning of each frame, producing a signal whose frequency is identical to the frame rate (250 Hz). The output of a divide-by-sixteen stage connected to the output of the voltage-controlled oscillator is then compared for phase and frequency errors with the 250 Hz signal from the level sensor, and an error signal is produced if a difference exists between the two signals. The error signal automatically adjusts the frequency of the VCO to minimize the error and maintain the 4 kHz output at the same frequency as the sampling rate.

The output of the 4 kHz VCO generates a series of pulses which triggers a sample-and-hold unit. The output of the sample-and-hold device is converted to a digital signal by the A-to-D converter, and the digitized signal is then fed into the digital computer. The timing of the trigger signal from the pulse generator is controllable so that the PAM signal is sampled at a suitable time during the "flat" portion



SIGNAL PROCESSING STAGES .

Figure G1

of the pulse.

Data Computation

A digital computer is a necessity for all but the simplest computations or data displays. In order to determine the correct pressure on each transducer, the measured value must be corrected for zero-offset and then compared to the reference pressure level set by the synchronization and calibration pulse amplitudes, taking into account the sensitivity of that particular transducer. A digital computer can perform this calculation very rapidly.

Some of the proposed data displays require information on the pressure at a large number of points on the surface of the hemisphere. Computer programs are available which can interpolate between the fourteen measured points to generate values for the pressure at any number of intermediate points. These interpolated values can then be used by the computer to generate displays, such as contour maps showing lines of constant pressure or pressure profiles on arbitrary planes through the hemisphere. Integration of the pressure distribution on the surface of the hemisphere to obtain the magnitude and direction of the resultant is also readily performed by the computer.

To fully use the information obtainable with the instrumented prosthesis, it is highly desirable to have the display and computation capability available at the time and location at which the tests are performed. This capability is possible through the use of a relatively portable mini-computer.

APPENDIX H

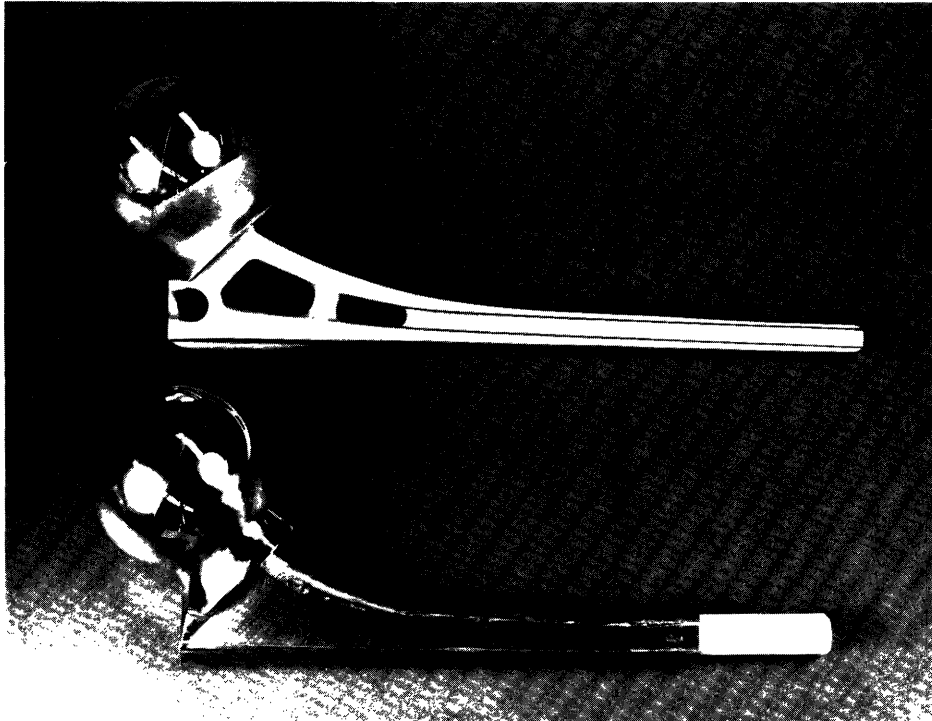
PROSTHESIS MODIFICATIONS, ASSEMBLY AND STERILIZATION

Mechanical Details of Instrumented Hip Prosthesis

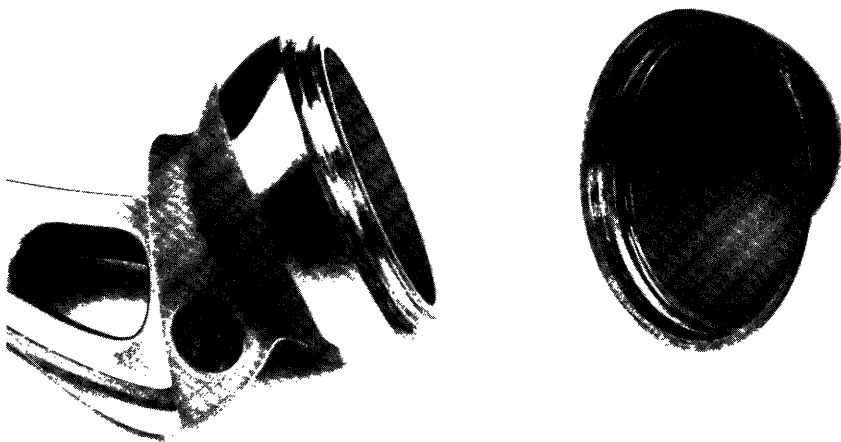
The instrumented hip prosthesis contains several specific modifications of the standard Moore prosthesis, some of which can be seen by comparing the two prostheses shown in Figure H1. The most important modification in terms of device safety is the construction of the pressure transducer diaphragms in the hemisphere of the prosthesis. The mechanical design and analysis of these diaphragms has been presented in detail in Appendix B. Other modifications are an annular ring in the ball of the prosthesis that aligns the hemisphere with the stem, the redesign of the stem to accommodate the coil on the stem tip and the coil and its protective sleeve.

Alignment Ring. The standard Moore prosthesis is normally cast in two parts, a hemisphere and a stem, as shown in Figure H2. A raised threaded section on the stem mates with female threads on the inside of the hemisphere. The hemisphere and stem must be held together temporarily while the exterior surface of the ball is ground and polished, after which the ball is opened, the pressure transducer diaphragms are machined, and the pressure transducers and telemetry unit are mounted. To simplify the procedure of aligning and welding the two parts together after the instrumentation has been mounted in the hemisphere, it is highly desirable to have a more accurate means of locating the hemisphere on the stem than is provided by the original threaded design.

The modified joint is shown in Figure H3. The joint consists



Standard and Instrumented Prostheses
Figure H1



Hemisphere and Stem of Standard Prosthesis
Figure H2



Hemisphere, Stem and Alignment Ring in Modified Prosthesis

Figure H3

of a circular ring that fits snugly in recesses ground in the walls of the hemisphere and stem. This arrangement eliminates any lateral motion between the hemisphere and stem and also allows the mating faces of the hemisphere and stem to be ground flat to produce a close fitting joint between the two pieces.

The circular alignment ring is machined from stainless steel, rather than Vitallium, since it is not exposed to body tissues. The recesses ground into the walls of the hemisphere are of minimum diameter and depth to insure that adequate wall thickness is maintained in the ball of the prosthesis.

A circular flange is machined in the inside diameter of this ring and serves as the support for the telemetry unit.

Stem Redesign. The most obvious modification of the prosthesis is the stem. The standard Moore prosthesis in Figure H1 is designed to be driven into the marrow cavity in the femur and has two transverse holes in its stem through which bone can grow to help secure the prosthesis. The instrumented prosthesis will be inserted by hand into a cavity in the bone marrow which has been reamed out to a size somewhat larger than the prosthesis stem and partially filled with freshly mixed polymethyl methacrylate. This procedure minimizes the impact loads applied to the prosthesis during implantation and rigidly fixes the prosthesis in the femur in a matter of a few minutes. The polymethyl methacrylate does not bond to the prosthesis stem but merely provides a close-fitting socket for the stem.

The stem is tapered to allow the prosthesis to be pulled out of the polymethyl methacrylate socket without damaging the socket or surrounding bone in the event that the prosthesis must be removed.

To insure that the power induction coil and its protective sleeve can be withdrawn with the prosthesis the cross-sectional dimensions of the stem must be at least as large as those of the sleeve. This is the reason for the rather massive appearance of the stem.

The tapered stem of the prosthesis helps lock the prosthesis in the polymethyl methacrylate socket, since the loads on the prosthesis act to force it into the socket. In addition, the essentially rectangular cross section of the upper portion of the stem prevents rotation of the stem in the socket.

Power Induction Coil Design and Assembly. The power induction coil and ferrite core mounted on the tip of the prosthesis stem must be protected from body tissues and fluids for it to perform satisfactorily, and any possibly injurious substances in the coil assembly must be isolated from the body. This design problem was approached from two aspects: to choose an encapsulation material with optimum properties, and to use materials for the coil and core assembly that were known or could reasonably be expected to be relatively bio-compatible.

Ideally, the material chosen to encapsulate the coil should be bio-compatible for long-term implantation, a good electrical insulator, mechanically tough, and non-porous. The material chosen for the encapsulation is premium grade virgin Teflon[®]. Teflon is an excellent insulator and has acceptable mechanical properties. It is generally accepted as an implantable material in situations in which it is not subjected to wear or exposed to the blood stream (Ref. 21). On the other hand, Teflon is somewhat permeable to water and other fluids. No ordinary adhesives will bond to it, and it tends to

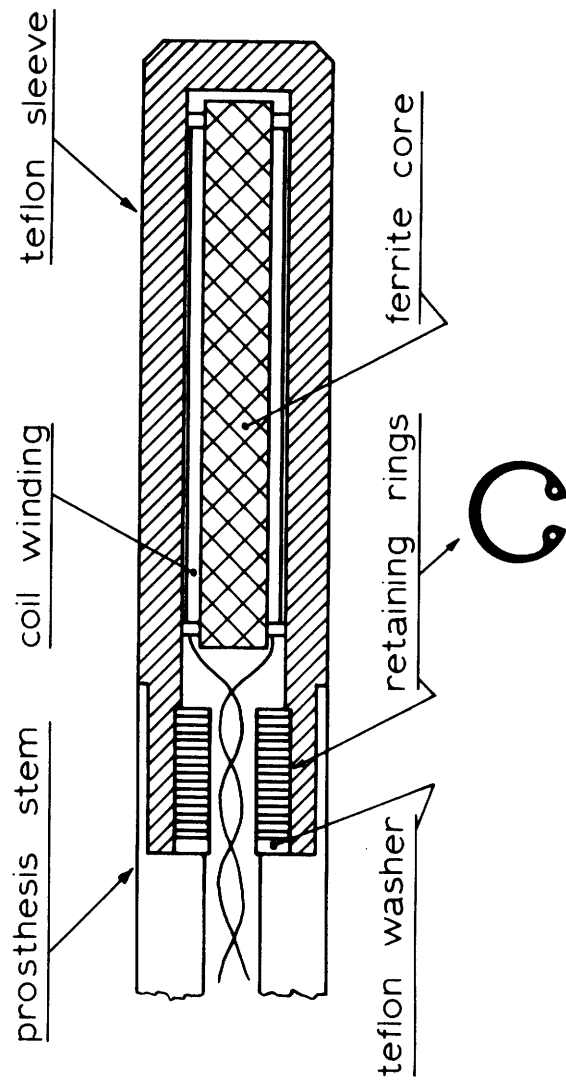
creep or cold flow under stress.

The coil encapsulation and the method of attaching the assembly to the prosthesis are shown in Figure H4. The coil and ferrite core are mounted in a sleeve machined from a single piece of Teflon. The sleeve fits into a recess machined in the stem of the prosthesis and is locked in place by some fifteen circular retaining rings. These stainless steel retaining rings, one of which is shown in the insert in Figure H4, are used as springs which push out in a radial direction on the Teflon sleeve, pressing it against the inside diameter of the recess in the stem. This arrangement securely fastens the Teflon sleeve to the stem and also provides a good moisture barrier at this point.

Teflon tends to cold flow when loaded, but only if it is unconfined. By eliminating where possible the spaces into which the compressed section of the Teflon sleeve can flow, loss of contact pressure between the sleeve and the stem recess can be minimized. The retaining ring "springs" also help to maintain contact pressure.

The encapsulation provided by the Teflon sleeve is relatively good, but it is not impermeable. Moisture can penetrate this barrier, possibly degrading the electrical performance of the coil, but more importantly dissolved material from the coil or the ferrite core could diffuse out through the Teflon sleeve. The rates at which substances pass through the Teflon sleeve can be reduced by using high quality Teflon of low micro-porosity and by maximizing the thickness of the walls of the sleeve, but the sleeve will still have some finite permeability.

It is, therefore, necessary to examine the bio-compatibility of



POWER INDUCTION COIL ENCAPSULATION.

Figure H4

the materials in the ferrite core, the power induction coil and its insulation, the stainless steel retaining rings, and the potting compound used to fill voids around the core/coil assembly.

The ferrite core is essential for the performance of the power induction system. Ferrites are composed of oxides of iron, manganese, magnesium, nickel and zinc, which are fused together under elevated temperature and pressure. Ferrites are relatively inert and are much like ceramics. Very little is known about them in terms of bio-compatibility, but in view of their ceramic-like properties the rate at which the constituents of the ferrite would be leached out by moisture penetrating the Teflon sleeve seems very small.

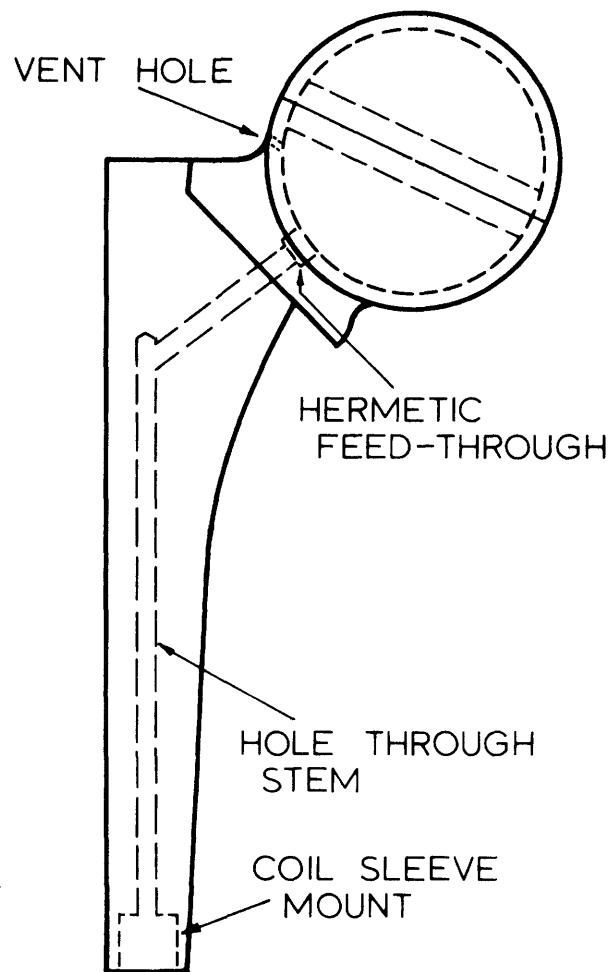
The wire chosen for the coil is Teflon insulated silver. The electrical requirements on coil resistance limit the choice of conductor materials to copper or silver, and silver is more corrosion resistant than copper. Silver has been used as an implant material, but it is not as corrosion resistant as Vitallium. Teflon insulation was chosen because of its excellent electrical properties and its chemical inertness.

The retaining rings are made of PH 15-7 Mo stainless steel which has good corrosion resistance properties. The use of dissimilar metals--stainless steel, Vitallium, and silver--in a potentially conductive medium must be done with care if electrical cells and the resultant corrosion are to be avoided. Specifically, there must be no direct contact between the different metals. The stainless steel retaining rings are isolated from the Vitallium stem by the Teflon sleeve and a Teflon washer (See Figure H4). The silver wire is isolated by its own insulation and the potting material.

The hole in the stem of the prosthesis through which the two wires from the coil pass to the interior of the ball and the space around the coil and ferrite core in the Teflon sleeve are filled with medical grade silicone rubber. The silicone rubber serves several purposes. It immobilizes the coil/ferrite core assembly and the wire pair in the stem hole, and it acts as a filler to minimize the volume available for moisture accumulation. The silicone rubber is permeable to moisture, however, so it does not act as a significant moisture barrier in thin sections. It does act as a significant barrier in the stem hole, shown in Figure H5. This hole is 0.125 in. in diameter and some 5 in. long, and the rate of diffusion of moisture through this hole, when filled with silicone rubber, is quite low, provided the rubber is well bonded to the walls of the hole. This long plug of rubber is protecting a hermetic seal (Figure H5) at the entrance to the interior of the ball. The wires from the coil are soldered to two terminals in this seal, and moisture at this point could conceivably cause some corrosion of the terminals.

Two types of medical grade silicone rubber are used. One type vulcanizes on contact with water vapor in the air, and the other uses a catalyst to initiate vulcanization. The first type is an adhesive that will bond to Vitallium, whereas the second type is not an adhesive and will not bond to Vitallium although it will bond to other silicone rubber surfaces.

The procedure for assembling the coil, core and Teflon sleeve to the prosthesis stem is as follows. A silicone rubber tube is passed through the stem hole and adhesive silicone rubber is forced



SIDE VIEW OF MODIFIED PROSTHESIS
(POWER INDUCTION COIL NOT SHOWN).

Figure H5

into the hole around the outside of the tube. Air is then pumped through the tube to insure that the tube is open and to accelerate vulcanization. The silicone tube is sufficiently permeable to moisture to allow adequate vulcanization. The adhesive rubber bonds both to the Vitallium surface and to the silicone rubber tube. The net result is that the hole has been lined with silicone rubber.

The power induction coil and ferrite core are then potted in the Teflon sleeve using the catalyst vulcanized rubber. The retaining rings are placed in the Teflon sleeve, followed by the insulating washer. The two wires from the coil are then passed through the silicone rubber tube in the stem hole and an appropriate amount of catalyst-vulcanizing rubber is forced into the rubber tube. The Teflon sleeve is then pressed into place in the recess on the tip of the stem while pulling on the wires projecting into the interior of the ball. Following vulcanization, the hermetic seal, which has tubular terminals, is slipped over the projecting wires and attached to the stem.

The Teflon sleeve mounted in this fashion is capable of a very small amount of bending relative to the stem. This semi-rigid mounting decreases the loads carried by the sleeve and causes the Vitallium stem to assume some of the stresses that would otherwise be imposed on the Teflon sleeve.

Prothesis Assembly

The assembly of the two basic subunits of the prosthesis--the stem with the power induction coil and the hemisphere with the pressure transducers and telemetry unit--has been described previously. The joining of these two subunits is presented here.

The telemetry unit in the hemisphere is connected to the two terminal pins of the hermetic feed-through seal in the stem by a pair of short wires. The hemisphere is then placed on the stem, taking care to align the hemisphere so that the transducers are in the specified locations. The seam between the two parts is then electron beam welded.

Electron beam welding is essentially what the name implies-- the source of energy for the welding process is a precisely controlled beam of electrons. The electron beam can be focussed very sharply and the intensity of the beam can be adjusted, so that very clean welds can be achieved with a minimum amount of energy input. The welding process is done in a vacuum so that there is no possibility of introducing contaminating elements into the weld.

A small tapered vent hole is machined in the stem side of the ball, as shown in Figure H5. This hole is necessary for two reasons: to insure that there are no traces of gas leaking out through the seam in the ball while it is being welded in the vacuum chamber, a situation that could cause a defective weld, and to allow the pressure inside the ball to be adjusted to atmospheric pressure after welding. This vent hole also allows the interior of the ball to be sterilized, as described in the following section. The hole is sealed after sterilization by a tapered pin which is welded in place.

The prosthesis is welded by rotating the prosthesis under the stationary electron beam. The energy input to the prosthesis ball is such that the temperature on the outer surface of the ball reaches a maximum of 350° F approximately 1/4 in. from the welded seam. This temperature rise does not exceed the limits of the epoxies

used in the pressure transducer assemblies, nor are the heat sensitive components in the telemetry unit excessively heated.

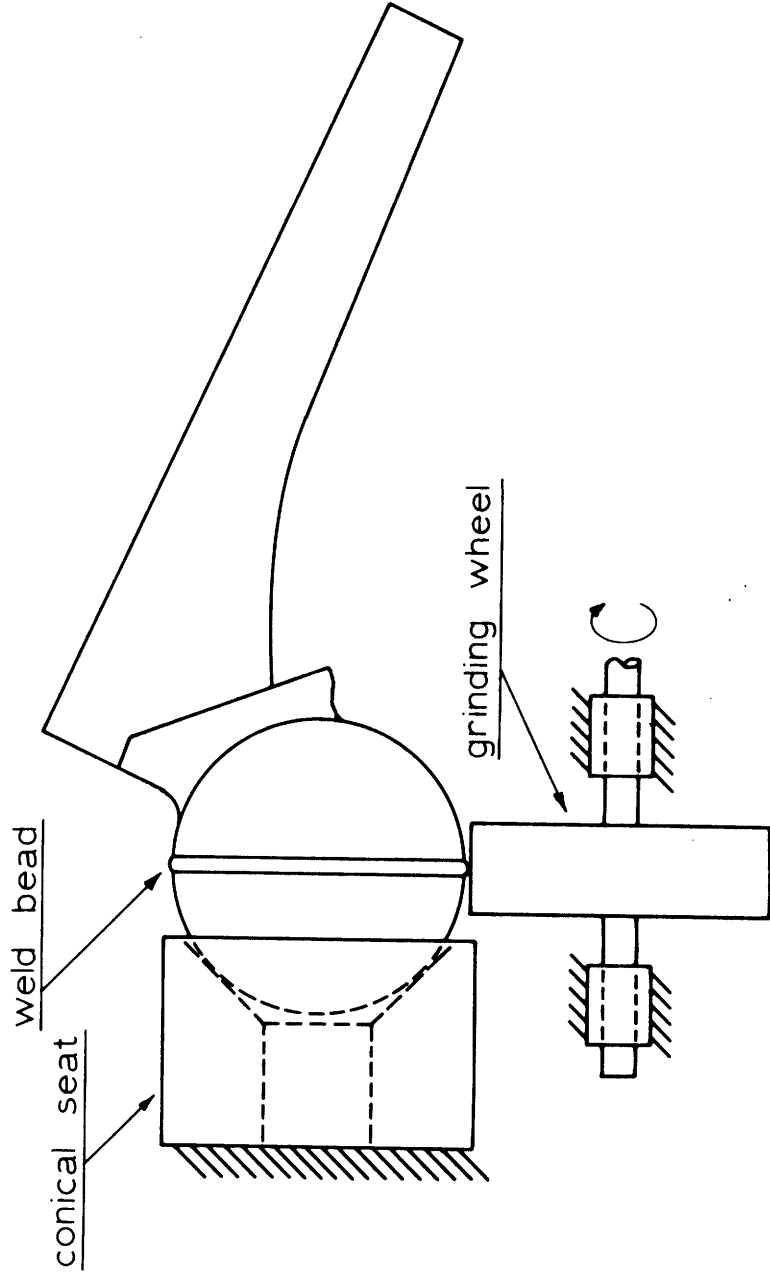
After the hemisphere and stem have been welded, a 0.010 in. diameter cast Vitallium wire is tack welded over the weld bead to add material to the weld to insure a built-up bead on the ball. This wire is then smoothed out over the previous weld, again by the electron beam welding process.

This weld bead is carefully ground down to match the radius of the prosthesis sphere in the device shown in Figure H6. By rotating the ball in the conical seat while oscillating the weld bead back and forth over the grinding wheel, the weld bead can be ground down to the desired radius. The correct radius is achieved when the weld bead has been ground to the point where the grinding wheel just begins to touch metal adjacent to the weld. The correct radius at the finished diameter is assured since the ball automatically rotates about its center. The ground area is then carefully polished to match the rest of the ball.

Prosthesis Sterilization Procedure

To insure that the instrumented hip prosthesis presents a minimum hazard to the test subject, the interior of the prosthesis as well as the exterior is sterilized. The probability of a catastrophic failure of the prosthesis that would expose body fluids and tissues to various components and materials inside the prosthesis is extremely small, but the sterilization is relatively straightforward and provides an additional degree of protection.

After the power induction coil and Teflon sleeve have been



WELD BEAD GRINDING SETUP

Figure H6

attached to the stem the completed stem is sterilized by heating it to a temperature of approximately 250° F. This step sterilizes the interior spaces in the stem, i.e., the stem hole, the ferrite core and coil, and the silicone rubber. All of the materials in the stem can easily withstand the 250° F temperature.

Some of the materials in the pressure transducer and telemetry unit, however, are not capable of withstanding this temperature. After the prosthesis hemisphere with its pressure transducers and telemetry unit has been welded to the stem, the interior of the sphere is sterilized by flushing the inside of the ball with ethylene oxide introduced through the vent hole. This gas is commonly used to sterilize certain devices that are temperature sensitive. Following this sterilization the interior of the ball is filled with nitrogen at atmospheric pressure which has been passed through a millipore filter, and a tapered pin is pressed into the access hole and welded in place, permanently sealing the ball. Nitrogen, rather than air, is used to fill the ball because of its inertness.

Prior to implantation the external surfaces of the prosthesis are gas sterilized with ethylene oxide. Some of the gas may be absorbed by the Teflon sleeve, and precautions must be taken to insure that the Teflon is adequately degassed before implanting the prosthesis.

REFERENCES

1. Hammond, B. T. and J. Charnley, "The Sphericity of the Femoral Head," Medical and Biological Engineering, Vol. 5, pp. 445-453, (1967).
2. Inman, V. T., "Functional Aspects of the Abductor Muscles of the Hip," The Journal of Bone and Joint Surgery, Vol. 29, No. 3, pp. 607-619, July (1947).
3. Paul, J. P., "Forces Transmitted by Joints in the Human Body," Symposium on Lubrication and Wear in Living and Artificial Human Joints, published by the Institution of Mechanical Engineers, London (1967).
4. Paul, J. P., "The Patterns of Hip Joint Force during Walking," Digest of the 7th International Conference on Medical and Biological Engineering, Stockholm (1967).
5. Rydell, N. W., Forces Acting on the Femoral Head-Prosthesis, Göteborg, Sweden, Tryckeri AB Litotyp (1966).
6. Charnley, J., "The Lubrication of Animal Joints in Relation to Surgical Reconstruction by Arthroplasty," Annals of the Rheumatic Diseases, Vol. 19, pp. 10-19 (1960).
7. MacConaill, M. A., "The Function of Intra-Articular Fibro-Cartilages, with Special Reference to the Knee and Inferior Radio-Ulnar Joints," Journal of Anatomy, Vol. 66, pp. 210-227 (1932).
8. Tanner, R. I., "An Alternative Mechanism for the Lubrication of Synovial Joints," Physics in Medicine and Biology, Vol. 11, No. 1, pp. 119-127 (1966).
9. McCutchen, C. W., "Mechanism of Animal Joints: Sponge-hydrostatic and Weeping Bearings," Nature, Vol. 184, pp. 1284-1285, October 24 (1959).
10. Longfield, M. D., D. Dowson, P. S. Walker, and V. Wright, " "Boosted Lubrication" of Human Joints by Fluid Enrichment and Entrapment," Bio-medical Engineering, pp. 517-522, November (1969).
11. Greenwald, A. S. and J. J. O'Connor, "The Transmission of Load Through the Human Hip Joint," Journal of Biomechanics, Vol. 4, pp. 507-528 (1971).
12. Aerospace Structural Metals Handbook, Vol. 2, Non-Ferrous Alloys. Syracuse University Press, New York (1963).
13. Lathi, B. P., Signals, Systems and Communication, John Wiley & Sons, Inc., New York, p. 437 (1965)

14. Schuder, J. C., J. H. Owens, H. E. Stephenson, Jr., and J. W. Mackenzie, "Response of Dogs and Mice to Long-term Exposure to the Electromagnetic Field Required to Power an Artificial Heart," Transactions, American Society for Artificial Internal Organs, Vol. 14, (1968).
15. Timoshenko, S., Theory of Plates and Shells, McGraw-Hill (1959).
16. Flügge, W., Stresses in Shells, Springer - Verlag (1966).
17. Wan, F. Y. M., "Membrane and Bending Stresses in Shallow, Spherical Shells," Technical Report 317, M.I.T. Lincoln Laboratory (1964).
18. Roark, R. J., Formulas for Stress and Strain, McGraw- Hill (1965).
19. Kraus, H., Thin Elastic Shells, John Wiley and Sons (1967).
20. Wissler, E. H., "An Analysis of Factors Affecting Temperature Levels in the Nude Human," Temperature, Its Management and Control in Science and Industry, C. M. Herzfeld, editor-in-chief, Biology and Medicine, Vol. 3, Part 3, J. D. Hardy, editor, p. 607.
21. Boretos, J. W., "Biomedical Materials Compatibility and the Design Challenge," 71-DE-8, The American Society of Mechanical Engineers, New York (1971).

BIOGRAPHICAL NOTE

Mr. Carlson was born on September 4, 1943, in Chicago, Illinois. In 1951 the Carlson family settled in Genoa, Illinois, where Mr. Carlson attended the Genoa-Kingston High School. He entered the University of Illinois in June of 1961 and received the degrees of B.S. in Mechanical Engineering and B.S. in Electrical Engineering, both with Highest Honors, in February, 1966. Mr. Carlson was Salutatorian of his graduating class. While at the University of Illinois he became a member of Pi Tau Sigma, ASME and SAE.

His graduate work at MIT began in September, 1966. In June, 1967, he received an S.M. in Mechanical Engineering. A National Science Foundation Fellowship, Teaching and Research Assistantship positions and a National Institute for General Medical Sciences Traineeship provided financial support for his graduate studies. While at MIT he became a member of Sigma Xi.

Mr. Carlson's industrial experience includes summer positions with John Deere & Company, Battelle Memorial Institute, Bell Telephone Laboratories, Douglas Aircraft Corporation, and the Lawrence Radiation Laboratory.

The author presented a paper titled "A Pressure Transducer/Telemetry System for Implantation in the Human Hip Joint" at the March, 1970, meeting of the Association for the Advancement of Medical Instrumentation in Boston, Mass. A second paper titled "A Proposed Method for Measuring Pressures on the Human Hip Joint" was presented at the May, 1970, meeting of the Society for Experimental Stress Analysis in Huntsville, Alabama, and was published in Experimental Mechanics, the Journal of the Society for Experimental Stress Analysis.

Upon completion of his graduate work, Mr. Carlson will be appointed Research Associate in the Mechanical Engineering Department at MIT.